

**DESIGN AND FABRICATION OF A
PHOTOTHERMAL SPECTROMETER
AND INVESTIGATIONS OF MULTILAYER
THIN FILMS**



Thesis submitted to Cochin University of Science and Technology

For the award of the degree of

DOCTOR OF PHILOSOPHY

By

Ramkumar S

Applied Optics Division
Department of Physics
Cochin University of Science and Technology
Kochi- 22, India

January 2006

Dr.K.P.Vijayakumar
Professor

Department of Physics
**Cochin University of Science
and Technology**
COCHIN-682 022
INDIA

Ph:(off):0484-2577404

(res):0484-2577103

Fax:0484-2577595

Email : kpvcus@cusat.ac.in

CERTIFICATE

Certified that the work presented in this thesis entitled "*Design and fabrication of a photothermal spectrometer and investigations of multilayer thin films*" is based on the bonafide research work done by Mr. Ramkumar S under my guidance in the Department of Physics, Cochin University of Science and Technology, Kochi - 682022, and has not been included in any other thesis submitted previously for the award of any degree.

Kochi-22
05-01-2006



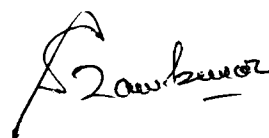
Prof. K. P. Vijayakumar
(Supervising Guide)

DECLARATION

Certified that the work presented in this thesis entitled “*Design and fabrication of a photothermal spectrometer and investigations of multilayer thin films*” is based on the original research work done by me under the guidance of **Prof. K. P. Vijayakumar**, Department of Physics, Cochin University of Science and Technology, Kochi - 682022, and has never been included in any other thesis submitted previously for the award of any degree.

Kochi-22

05-01-2006

A handwritten signature in black ink, appearing to read 'Ramkumar S', with a stylized flourish at the end.

Ramkumar S

The journey was very long and the distance traveled so less! Ten years through the desert in search of that vital elixir of life, the key to all pervasive truth that kept on eluding me: yes it was a true "mirage".

From my Masters' days till today with unseen hands two persons kept on supporting me. Yes their presence was almost silent and in the shadows, leading me when there was no light, holding me when I staggered and fell. I owe everything in this pursuit to my guiding light Prof. K P Vijayakumar and Dr. C Sudha Katha.

As an engineer by training I strayed into the corridors of Dept. of Physics, I was given a warm welcome. Within a short period I was also one among the physics family at CUSAT. I remember with my heart full the support extended to me by all the faculty members.

Dr. T M Abdul Rasheed holds a special place in my heart for he was the one who initially drove me hard, shared new ideas and propelled me. His meticulousness had always left me wondering.

The support that I have received from the Dept. of Physics office all these years has been tremendous.

Dr. Madhusoodanan, Department of Instrumentation, CUSAT, is acknowledged for the lead he provided by showing me the "deflection".

Mr. Pradeep G is a very special person to me. His research methods were so near perfect. My initial days in research would not have been possible but for his resourcefulness.

Mrs. Elizabeth Fenn, Ms. Sheena Mary John, Dr. Minu Joy, Dr. Jyothsna and Ms. Chitra Nayak were my co-travelers in my pursuit at different instances of time. All of them have contributed immensely to enrich this work.

Dr. Sunny, Dr. Vidyadharan Pillai, Dr. Varkey, Dr. Zeenath, and Dr. Syamala were inspiring seniors. On my bad days, Sunny's tireless and long innings in developing VASE here helped me to pull on. Dr. Varkey was a part-timer par excellence. I have never seen any other plan his time here at CUSAT as methodically as he used to.

Dr. Bindu, Dr. Bini, Dr. Lakshmi and Ms. Shiji were my contemporaries. My odyssey into thin films might not have happened without them. The moments we have shared are still cherished.

Renu and Harish are fondly remembered for the support they lend me in building the spectrometer.

Dr. Rupa and Dr. Teny were my juniors in the thin film laboratory. After my contemporaries left it was they who made my life at CUSAT easy, especially Teny. It was with investigations done on Teny's samples that the system reached its maturity.

Ratheesh, Wilson, Kishore, Beena, Deepa, Jayakrishnan, Sreekumar, 'Solar' Sreekumar, Tina, Merrill: had their whole hearted support not been there, it would not have been possible for me to touch this finishing line.

Ms. Anitha Warriar, like any one who starts their research, takes everything with a pinch of salt. Her criticism has helped me to review our results with enthusiasm.

Sreelatha, Malini, Viji, Shaji, Joesph Mathai, Saji Augustin, Santhosh and Saravanan are great friends to have.

I express my deep gratitude to the Management of Rajagiri School of Engineering and Technology my current employer for their constant support.

Rev. Fr. Jose Alex and Rev. Fr. Mathew Vattethara and Prof. Joseph Injodey were sources of strength.

Prof. Babu Joseph saw me mature from a student to a researcher and later to a teacher. His support and guidance to me from my Masters days is acknowledged.

Prof. Mathew Panjikkaran's parental concern for me has been so touching. He and Prof A C Mathai, Principal, RASET, finally could arrange to "send me off" to complete this work.

The encouragement I have received from NPOL residents, scientist friends and their families all these years have been overwhelming.

Paul (Dr. Paulraj) is more than a brother to me. Over the last six years we were together through thick and thin professionally and personally. Photothermal spectrometer at the Applied Optics Division is a standing testimony to our togetherness.

I have been blessed with tremendous support from all my dear and near.

I still believe the journey is a long one since the "mirage" continues to tempt me and keep me going.

Ramkumar S

Preface	i-iv
Publications	P1-P2
Chapter 1	
Introduction	1.1
1.1 Laser Excitation and Induced Processes	1.8
1.1.1 Laser Excitation	1.8
1.1.2 Laser-Induced Processes	1.9
1.2 Detection Schemes	1.12
1.2.1 Temporal Variation of Radiation Intensity	1.12
1.2.2 Detection Methods	1.13
1.3 Interface Systems	1.15
1.3.1 Homogeneous Phases with Ideal Boundaries	1.15
1.3.2 Random Media	1.17
1.3.3 Films and Layered Structures	1.17
1.4 Applications	1.18
1.4.1 Spectroscopy	1.18
1.4.2 Distribution of Energy	1.19
1.4.3 Transport Processes	1.20
1.4.4 Nondestructive Evaluation	1.20
1.5 Discussion of the Literature	1.21
REFERENCES	1.22
Chapter 2	
Photothermal and Photoacoustic Effects and Applications	2.1
2.1.1 Signal Generation Process	2.4
2.1.2 Detection Methods	2.13
2.1.3 Instrumentation	2.24
2.2 Spectroscopy of Thin Films	2.29
2.2.1 Semiconducting Films	2.30
2.2.2 Dielectric and Metallic Films	2.33
2.2.3 Spectroscopy of Layered Films	2.34
2.2.4 Nonradiative Quantum Yield	2.35
2.3 Thermal Analysis of Thin Films	2.37
2.3.1 Thermal Diffusivity	2.37
2.3.2 Film Thickness	2.39
2.3.3 Phase Transitions	2.40
2.4 Ultrasonic Analysis of Thin Films	2.41
2.5 Nondestructive Evaluation of Thin Films	2.43

2.5.1	Depth Profiling	2.44
2.5.2	Imaging	2.46
2.6	Miscellaneous Thin Film Applications	2.48
2.6.1	Plasmon Detection	2.48
2.6.2	Ferromagnetic Resonance	2.49
2.7	Conclusion	2.50
	REFERENCES	2.51

Chapter 3

	Photothermal Spectrometer: design and use	3.1
3.1.1	The Pump Source	3.3
3.1.2	The Mechanical Chopper	3.3
3.1.3	The Probe Beam Source	3.3
3.1.4	The Sample Cell	3.4
3.1.5	The Detector Assembly and Signal Measurement	3.5
3.1.6	Vibration Isolation Table	3.6
3.2	Results And Discussions	3.20
3.2.1	CuInSe ₂	3.21
3.2.2	In ₂ S ₃ thin films	3.22
3.2.3	CuInS ₂ thin films	3.32
3.2.4	Rubbers	3.41
3.2.5	Poly Urethane with fillers	3.49
3.2.6	He ⁺ implanted CdS	3.52
	REFERENCE:	3.56

Chapter 4

	Lock in Detection	4.1
4.1	Why lock in detection?	4.1
4.2	The basic lock in strategy	4.2
4.2.1	Asynchronous detection	4.3
4.2.2	Synchronous ("lock-in") detection:	4.3
4.2.3	The theory of lock in detection	4.4
4.4	Harmonics:	4.8
4.5	The Typical Lock-In Amplifier	4.9
4.5.1	Signal Channel	4.9
4.5.2	Reference Channel	4.10
4.5.3	Phase-sensitive Detector	4.10
4.5.3.1	Analog Multiplier	4.10

4.5.3.2 Digital Switching Multiplier	4.11
4.5.3.3 Digital Multiplier	4.12
4.5.4 Low-pass Filter and Output Amplifier	4.13
4.5.5 Output	4.14
4.5.6 Single Phase and Dual Phase	4.14
4.5.7 Internal Oscillator	4.15
4.6 The PLL	4.15
4.6.1 Operating Principles of the PLL	4.15
4.6.2 Classification of PLL types	4.19
4.6.3 The SPLL	4.20
4.6.3.1 The Hardware-Software Trade-off	4.20
4.6.3.2 Feasibility of an SPLL Design	4.22
4.7 SPLL. Examples	4.24
4.8 Implementation	4.43
REFERENCES	4.49
Summary, Conclusion and Scope for future work	5.1
Scope for Future Work	5.2
REFERENCE	5.5
APPENDIX A	
Temperature Distribution in a photothermal experiment	A1-A9
APPENDIX B	
ADSP 2105 and sample PLL code	B1-B12

PREFACE

Surface characterization is an essential branch of materials science. Many different and complementary techniques currently used in the field of surface and thin film analysis.

Most of these methods involve bombarding the sample with an incoming (incident) particle and monitoring an ejected particle. Each of the methods wherein the incident particle is either an electron or an ion measures must be taken to insure that the sample surface is electrically conductive. Thus, for insulating materials and films such as oxides, glasses, and polymers, the experiments are not straight forward. Many of them have limitations on the sample form and sizes. On the instrumentation side, most of these techniques employ ultra high vacuums, require sophisticated components and hence are very costly. Time taken for measurement and analysis are prohibitively high.

Photothermal spectroscopy is a group of high sensitivity methods used to measure optical absorption and thermal characteristics of a sample. The basis of photothermal spectroscopy is a *photo*-induced change in the *thermal* state of the sample. Light energy absorbed and not lost by subsequent emission results in sample heating. This heating results in a temperature change as well as changes in thermodynamic parameters of the sample which are related to temperature. Measurements of the temperature, pressure, or density changes that occur due to optical absorption are ultimately the basis for the photothermal spectroscopic methods.

Preface

Sample heating is a direct consequence of optical absorption and so photothermal spectroscopy signals are directly dependent on light absorption. Scattering and reflection losses do not produce photothermal signals. Subsequently, photothermal spectroscopy more accurately measures optical absorption in scattering solutions, in solids, and at interfaces. This aspect makes it particularly attractive for application to surface and solid absorption studies, and studies in scattering media

Photothermal spectroscopy can be used to measure acoustic velocities, thermal diffusion coefficients, sample temperatures, bulk sample flow rates, specific heats, volume expansion coefficients, and heterogeneous thermal conductivities in solids. In particular, a technique called thermal wave imaging allows nondestructive material inspection by measuring the rate of heat transfer in heterogeneous materials.

In this work we present the results of our attempt to build a compact photothermal spectrometer capable of both manual and automated mode of operation. The design has been extended to incorporate other complementary optical spectroscopic schemes like ellipsometry, PL and LBIC. Data acquisition and analysis has been automated through indigenization and implementation of 'Lock-in-Amplifier' using PC. The spectrometer has then been put to use to analyse single and multilayer semiconductor thin films, transparent oxides, polymer samples.

CHAPTER ONE is a very brief introduction to surface analysis techniques and comparison of strengths and weaknesses. The need for a low cost,

Preface

complementary and versatile technique for surface analysis is identified. We justify the selection of thermal wave techniques for surface analysis and introduce the fundamentals of signal generation, detection. An overview is presented of the recent advances and developments. This includes the development of theoretical models in the time and frequency domains, and the fundamental mechanisms involved in photoacoustic, photothermal and photochemical processes. The analysis of these phenomena by different experimental techniques and their application in spectroscopy, the field of transport processes, and nondestructive evaluation, etc., is discussed.

CHAPTER TWO presents photothermal and photoacoustic effect in thin films. Signal generation process is outlined. Photothermal and photoacoustic spectroscopy requires an understanding of the signal generation process so that detection methods can be carefully chosen. The various detection schemes are outlined. This naturally leads into the discussion on the choice of instrumentation. A very generic photothermal spectrometer is discussed. Spectroscopy of thin films, semiconducting films, dielectric and metallic films, spectroscopy of layered films and nonradiative quantum yield which are the broad spectrum application areas are briefly highlighted. The chapter further goes on to highlight thermal analysis of thin films resulting in computation of thermal diffusivity and film thickness and identification of phase transitions.

The chapter wind up with the application of the technique in nondestructive evaluation of thin films particularly depth profiling, imaging and other miscellaneous thin film applications.

Preface

CHAPTER THREE describes the design and fabrication of our compact photothermal spectrometer and the results of analysis of single and multilayer thin films and polymer samples. The fabrication of the vibration isolation table and its characterization is discussed. Detection electronics is also outlined. Studies on In₂S₃, CuInSe₂, CuInS₂ and ion implanted CdS samples and results on their thermal diffusivity, thickness and mobility are reported. Additive of fillers on polymers to modify their properties is well studied. We report the synergy of filler addition on the thermal properties of Poly Urethane and Rubber.

Signal recovery from noise had always been a challenge in spectroscopy. In **CHAPTER FOUR** is about the indigenization of the 'Lock-in-Amplifier'(LIA), a powerful tool in signal recovery in frequency modulated experiments. Fundamental building blocks of LIA are illustrated and their software counter parts discussed. Finally our implementation of a software LIA is discussed.

The summary of the work done and the scope for including other complementary techniques in the photothermal spectrometer is the content of the concluding chapter. The integration VASE (Variable Angle Spectroscopic Ellipsometer), Photoluminescence (PL) and photoconductivity into the same instrumentation with theoretical integration of information content derived from these techniques would form the core of future work.

List of papers publications in journals and international / national conferences

1. Characterisation of undoped and Cu doped CdS thin films using photothermal and other techniques. M. Paulraj, **S. Ramkumar**, K. P. Varkey, K. P. Vijayakumar, C. Sudha Kartha, K. G. M. Nair, *Phys. Stat. Sol. (a)*, **1– 10** (2004) / DOI 10.1002/pssa.200406918.
2. Studies on Ar⁺ implanted CdS films using photothermal deflection technique. M. Paulraj, **S. Ramkumar**, K. P. Vijayakumar, C. Sudha Kartha, P. Magudapathy, K. G. M. Nair and B. Viswanathan, *Nucl. Instr. And Meth. In Phys. Res. B*, **122(1-2)** (2004) 123-129.
3. Photothermal imaging of He⁺ ion implanted CdS, M. Paulraj, **S. Ramkumar**, C. Sudha Kartha, K. P. Vijayakumar, and K. G. M. Nair, *Journal de Physique IV*, 125(2005)97
4. Characterisation of In₂S₃ and ZnO thin films for photovoltaic application using photothermal deflection technique, M. Paulraj, **S. Ramkumar**, Teny Theresa John, P. M. Ratheeshkumar, C. Sudha Kartha, K. P. Vijayakumar, and K. G. M. Nair, *Journal de Physique IV* 125(2005)469.
5. Determination of thickness and mobility of In₂S₃ and ZnO thin films using photothermal deflection technique. M. Paulraj, **S. Ramkumar**, Teny Theresa John, P. M. Ratheeshkumar, C. Sudha Kartha, K. P.

- Vijayakumar, and K. G. M. Nair, Proceeding in Regional Conference on Photoacoustics in Condensed matter physics and NDT, held at Madurai Kamaraj University (School of Physics) (March 2004).
6. Determination of thermal diffusivity of polymethane doped with various fillers by photothermal deflection method. M. Paulraj, **S. Ramkumar**, V. G. Jayakumari, S. Kusuma Kumari, C. Sudha Kartha, K. P. Vijayakumar, Proceeding of International Seminar on Advances in Polymer technology - CUSAT, held at Cochin, India (Dec 2002).
 7. Photothermal deflection spectroscopy for ion implanted thin films, M Paulraj, **S. Ramkumar**, A. Jayaprasad, K. P. Vijayakumar, C. Sudha Kartha, K. G. M. Nair, T. S. Radhakrishnan - Proceedings of DAE Solid state physics Symposium, held at Mumbai - India, (Dec 2001).

Chapter 1

Introduction

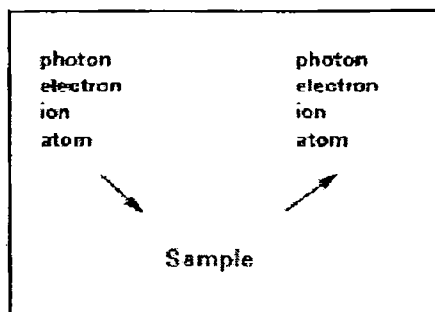
Surface is a special state of condensed matter, and it is the boundary of materials with vacuum. In the semiconductor device industry, for example, techniques are needed to control surface structures in order to control some specific transport properties. Epitaxial growth of thin films is becoming an indispensable technique for synthesizing new materials, such as superconductor thin films, semiconductor superlattices, metallic superlattices (or multilayers) and diamond films, which have important applications in advanced technologies. Therefore, surface characterization is an essential branch of materials science. Techniques which have been applied to investigate surface structures are classified into the following categories: Surface crystallography, Diffraction and imaging, Electron spectroscopy, Incident ion techniques, Desorption spectroscopy, Tunneling microscopy, Work function techniques, Atomic and molecular beam scattering, Vibration spectroscopy etc. Many different and complementary techniques currently used in the field of surface and thin film analysis. The table below lists the information content of various surface analysis techniques.

What do we want to know ?	How do we find this out ?
What does the sample look like ? <ul style="list-style-type: none">• on a macroscopic scale• on a microscopic scale	<ul style="list-style-type: none">• optical microscopy• scanning electron microscopy (SEM)• transmission electron microscopy (TEM)

<ul style="list-style-type: none"> • on an atomic scale 	<ul style="list-style-type: none"> • scanning probe microscopies (STM, AFM ...)
<p>What is the structure of the sample ?</p> <ul style="list-style-type: none"> • internal structure • density • microscopic and atomic scales 	<ul style="list-style-type: none"> • X-ray diffraction (XRD) • stylus profilometry • quartz crystal monitors (QCM) • ellipsometry • low energy electron diffraction (LEED) • reflection high energy electron diffraction (RHEED)
<p>What is the sample made of ?</p> <ul style="list-style-type: none"> • elemental composition • impurities • chemical states 	<ul style="list-style-type: none"> • Auger Electron Spectroscopy (AES) • Energy Dispersive Analysis of X-rays (EDAX) • X-ray Photoelectron Spectroscopy (XPS) • Secondary Ion Mass Spectrometry (SIMS) • Rutherford Backscattering (RBS)
<p>What are the optical properties of the sample ?</p> <ul style="list-style-type: none"> • refractive index, absorption • dielectric properties • as a function of wavelength 	<ul style="list-style-type: none"> • ellipsometry
<p>What are the electrical properties of the sample?</p> <ul style="list-style-type: none"> • device properties 	<ul style="list-style-type: none"> • resistance - four point probe • capacitance

<ul style="list-style-type: none"> • material properties <ul style="list-style-type: none"> ○ resistance / conductance ○ capacitance 	
<p>What are the magnetic properties of the sample ?</p> <ul style="list-style-type: none"> • hysteresis loops 	<ul style="list-style-type: none"> • magneto-optical Kerr effect (MOKE) • ferromagnetic resonance (FMR)
<p>What are the mechanical properties of the sample ?</p> <ul style="list-style-type: none"> • internal stress in films / substrates • friction • adhesion 	<ul style="list-style-type: none"> • stress curvature measurements • pin on disk friction test • adhesion tests

Most of these methods involve bombarding the sample with an incoming (incident) particle and monitoring an ejected particle as shown. The precise method being employed is differentiated from the others according to the identity of the respective particles. Figure 1 illustrates the basic principles and Table 1 lists the most common techniques and their acronyms.



Incident	Ejected	Technique	Acronym
X-ray	Electron	X-ray photoelectron spectroscopy Electron spectroscopy for chemical analysis	XPS ESCA
X-ray	X-ray	X-ray fluorescence spectrometry	XRF
Electron	Electron	Auger electron spectroscopy	AES
Electron	X-ray	Electron probe microanalysis	EPMA (EDAX)
Ion (Ar, Xe, Cs,O)	Sample ion	Secondary ion mass spectrometry	SIMS
Ion (Ar, Xe, Cs,O)	Sample atom	Sputtered neutral mass spectrometry	SNMS
He ion	He ion	Rutherford backscattering spectrometry	RBS

Technique	Application	Comments
SIMS depth profiling	Measurement of: <ul style="list-style-type: none"> • Dopant concentrations • Impurity (co-implant) concentrations • Diffusion effects 	The most sensitive chemical profiling technique Quantification for dilute impurities in dilute matrices with use of reference materials
RBS	Quantitative analysis of: <ul style="list-style-type: none"> • Oxides and Nitrides • Silicides • Compound semiconductors • Optical coatings • Metallurgical coatings 	Without standards
XPS	Analysis of: <ul style="list-style-type: none"> • Polymers • Oxides, nitrides and other compounds • Contamination issues 	Provides chemical state information
Auger	<ul style="list-style-type: none"> • High resolution chemical mapping • Depth profiling • Small area analysis 	Not suitable for analysis of insulators

Analytical method	XPS	AES	SIMS
element identification	Z>2	Z>2	all elements
compound identification	possible	rarely	possible
structure information	no	phys. imaging	phys. imaging
information depth	5-8 nm	5-8 nm	< 1 nm
depth profile	possible	good	inherent
depth resolution	20 nm	20 nm	25 nm
lateral resolution	none	2 μ m	150 μ m
quantification	possible	possible	rarely
sample form	solid/powder	solid	solid/powder
sample size	8-20 mm	2-20 mm	4-20 mm
non-conducting samples	good	difficult	possible
time for measurement	2 h - 1 d	2 h - 1 d	2 - 5 h
time for analysis	4 h - 5 d	4 h - 5 d	4 h - 1 d

These techniques yield subsurface information through the removal of sample material through sputtering with a high energy particle beams. The sputtering rates are of the order of 10 nm/min which mean films of greater than 5 micron thickness require prohibitive amounts of time for analysis. Also these instruments are to be maintained at high vacuums. In short they need very sophisticated components and trained personnel to work on them. As a result these instruments cost a lot.

Photothermal methods possess what is known as the zero-baseline advantage. In plain language, this means signals are generated only if there is an optical absorption event and subsequent conversion to thermal-wave energy above an otherwise zero background signal, even in the presence of large, non-converted optical fields. This feature, coupled with the strong spatial damping of optically generated thermal waves in the vicinity of photon deposition followed by coherent thermal conversion, can yield extremely localized detection of ultraweak absorptions in thin films and fluids at unprecedented sensitivity limits⁶ for absorptances, in the range below 10^{-6} . Because of the extraordinary improvement in dynamic range measurements, significant new physics and industrial and clinical applications have become possible in the past 30 years as a result of combinations of the unique abilities of photothermal techniques and instruments. The applications below are typical of the considerable potential of emerging photothermal diagnostic technologies to successfully address widely disparate scientific and engineering disciplines, including photonic materials science, metallurgical non-destructive depth profilometry, and semiconductor thermoelectronic imaging, through signal-generation processes that yield results that are far superior to those that can be obtained using purely optical techniques

This chapter provides an elementary introduction to the characteristic features of photoacoustic, photothermal and photochemical processes occurring in heterogeneous systems and their detection and analysis. This includes the development of theoretical models in the time and frequency domains, and the fundamental mechanisms involved in photoacoustic, photothermal and photochemical processes. The analysis of these phenomena by different ex-

perimental techniques and their application in spectroscopy, the field of transport processes, and nondestructive evaluation, etc., is discussed.

1.1 Laser Excitation and Induced Processes

1.1.1 Laser Excitation

Lasers are finding a wide variety of applications in the investigation of photoacoustic, photothermal and photochemical processes at interfaces. With their specific qualities, the ability to deliver light of extremely high power, extremely high spectral purity and/or extremely short duration, they are the most important radiation sources in the field today.

One of the most important properties is that of high spectral purity. The laser wavelength determines the nature of the excitation process. Electronic excitation in adsorbate systems including the excitation of surface plasma resonances in small metal particles adsorbed on a substrate, the resonant excitation of molecular multilayer systems from the IR to the UV spectral region and vibrational excitation in the IR and electronic excitation in the VIS and UV regions are the processes investigated in the majority of the studies. The high directionality and beam quality of many laser sources provides the basis not only for localized excitation and heating, but also for localized optical detection of density gradients, geometrical changes of shapes, etc. This will be discussed in more detail in the section considering experimental techniques.

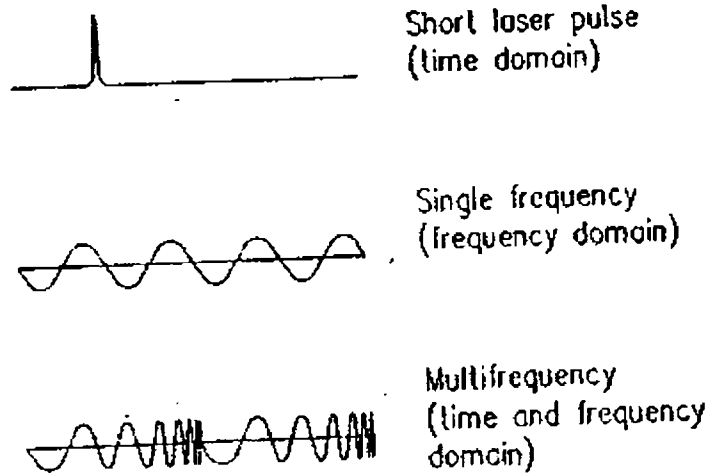


Fig 1.1 Temporal behavior of laser radiation for time domain, frequency domain and combined time and frequency domain analysis

The temporal properties of the laser radiation employed determine the principles of detection and analysis. Short laser pulses are used for detection in the time domain as shown in Fig. 1.1. Even microsecond to nanosecond laser pulses enable time-resolved detection of many processes such as transport phenomena. In the near future, ultrashort laser pulses will become increasingly available commercially and this will have an important impact on future developments. Of course, there is a trade off which relates the duration of light pulses to their spectral purity by the uncertainty principle. Thus, a picosecond pulse covers a frequency range of 5 cm^{-1} and a femtosecond pulse, $5 \times 10^3 \text{ cm}^{-1}$. This spread over a larger frequency range, however, does not create problems in many photothermal and photoacoustic experiments. As shown schematically

in Fig. 1.1, cw laser radiation is also employed for photothermal and photoacoustic analysis. The cw radiation is either modulated with a single frequency, to perform analysis in the frequency domain, or the modulation frequency is varied as indicated in Fig. 1.1. The latter technique is relatively new and possesses features intermediate between the frequency and time domains.

1.1.2 Laser-Induced Processes

With laser radiation a variety of processes can be induced at surfaces and in thin films. Figure 1.2 gives an overview, illustrating schematically a large number of effects that may be stimulated by laser radiation. The absorption of one or several photons can lead to direct quantum effects, e.g., the dissociation of the absorbing molecule and the desorption of the fragments. It has been proved that direct photochemical decomposition of an adsorbed molecule by a laser photon is possible and that multiphoton photoemission of electrons occurs at metal surfaces.

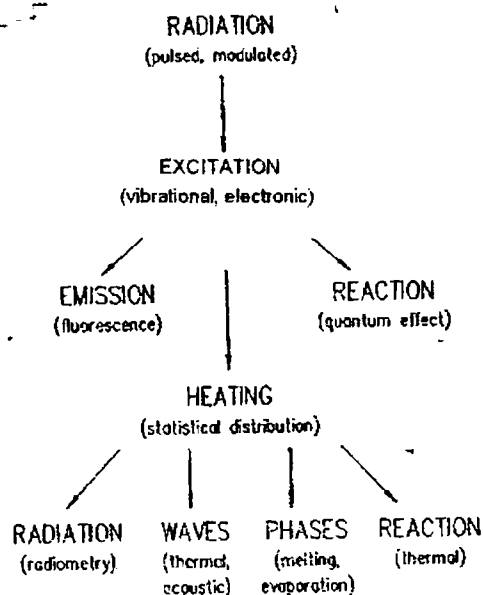


Fig 1.2 Scheme of the processes induced by laser radiation either directly or indirectly by heating

Recent experimental results indicate a limited efficiency of these quantum processes. Direct photodecomposition and high-order multiphoton photoemission seem to be confined to the surface region. This is also true for the direct emission of photons following the excitation process and it is therefore difficult to observe IR and UV fluorescence from the surface. The energy exchange between the excited state and other states and degrees of freedom often occurs on the picosecond time scale in condensed phases. Thus, laser irradiation normally leads to transient heating in the irradiated zone. This transient and localized heating process causes a series of effects as indicated in Fig. 1.2. Transient heating results in variations of the infrared thermal radiation emitted from the irradiated sample region. This effect is used in photothermal

radiometry for remote sensing and nondestructive testing. Another collective effect connected with transient or modulated heating is the creation of thermal waves. The special properties of these thermal waves and their application in thin film analysis, depth profiling and nondestructive evaluation are reviewed extensively in literature. The disadvantage of thermal waves is their efficient attenuation. The detector has to probe the temperature within one thermal diffusion length of the excited area. Therefore, it is often advantageous to detect the acoustic waves generated by the transient temperature profile. The latter causes thermal expansion and a corresponding stress profile leading to the generation of sound waves. These sound waves are essentially unattenuated and thus propagate over long distances. Special types of these acoustic waves are confined to the surface and they are therefore called surface acoustic waves (SAWs).

1.2 Detection Schemes

1.2.1 Temporal Variation of Radiation Intensity

The temporal behavior of the perturbation applied to a system by the impinging radiation determines the nature of the resulting effects and the appropriate detection scheme. Pulse methods use an impulse perturbation and the response of the system is monitored in the time domain (Fig. 1.1). In the quantitative description, the input waveform is modified by the impulse response function, giving the output waveform by a convolution integral. The physical basis of these pulsed methods is the fact that a narrow pulse contains many frequencies probing the sample simultaneously. The high peak powers of pulsed laser sources can be used to produce intense thermal transient, and time-gated detection allows

effective discrimination against spurious signals. On the other hand, pulse measurements possess a low duty cycle of excitation.

Frequency domain measurements are realized by applying a single modulation frequency to a continuous laser beam (Fig. 1.1). The effect of the system consists in a modification of the amplitude and phase. This is described quantitatively by the system transfer function. Multiplication of the input spectrum by this transfer function directly yields the output spectrum. Thus, analysis is simpler in the frequency domain. The much more efficient duty cycle of this method permits a reduction of the amount of energy absorbed by the sample per unit time, and thus, its application to fragile materials.

As mentioned previously, multifrequency modulation can be performed to realize a technique intermediate between the frequency and time domains. This technique uses a variable modulation frequency sweeping linearly over the same range in a short frequency chirp, as shown in Fig. 1.1. An important advantage of this method is its ability to yield information in both domains simultaneously.

1.2.2 Detection Methods

An advantage of the pulse methods is the high optical power density that can be achieved. This enables the experimenter to study nonlinear processes such as multiphoton excitation. The intense thermal transients may also induce phase changes, desorption and ablation of material etc. Figure 1.3a shows schematically the emission of different particles, including electrons, ions, molecules and clusters, following irradiation with a narrow high power pulse. One of the most important methods of detecting these processes is time-of-flight

mass spectrometry, which presents information on the chemical nature, yield and kinetic energy of emitted species. This technique also elucidates the mechanism involved, e.g., the photochemical or photothermal features. A number of detection methods utilize a second low-power probe laser beam to observe photothermal effects induced by the excitation laser. The probe laser beam either travels parallel to the surface or monitors the refractive index gradient caused by a temperature gradient or acoustic wave front, or the probe beam hits the surface and is deflected by the buckling surface as indicated.

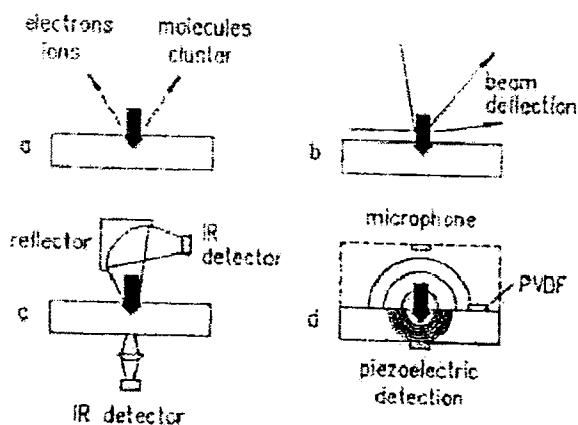


Fig 1.3 Laser induced effects and their analysis (a) particle emission (b) pump-probe detection (c) photothermal radiometry (d) photoacoustic detection

Another optical detection method is that of photothermal radiometry based on blackbody radiation emitted from the heated spot. As shown in Fig. 1.3c, the IR detector may be positioned at the side of the excitation source or on the other side of a thin sample.

Figure 1.3d presents three different configurations for the detection of acoustic waves with a pressure sensor. If the irradiated sample is in contact with a gas atmosphere, a cheap electret microphone can be used for detection. Surface acoustic waves can be detected with a piezopolymer (PVDF) in contact with the irradiated surface. In a similar way, bulk sound waves can be monitored with piezoelectric transducers in contact with any surface of the sample

1.3 Interface Systems

1.3.1 Homogeneous Phases with Ideal Boundaries

A simple model for treating photothermal and photoacoustic phenomena in interface systems is to assume two semi-infinite homogeneous phases, e.g., a gas and a solid, separated by an ideal surface as shown in Fig. 1.4. This means that spatially homogeneous optical and thermal properties are assumed for each phase. To describe heat diffusion, for example, the classical Fourier equation is used in the isotropic media and interfaces are taken into account by appropriate boundary conditions.

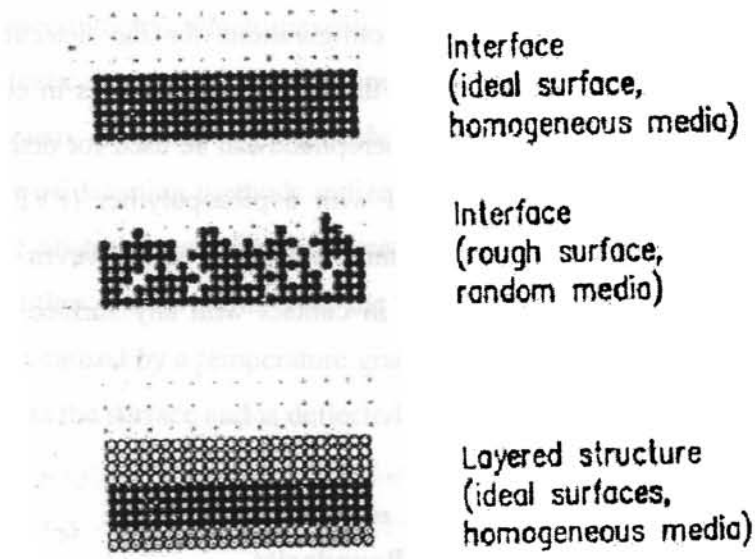


Fig 1.4 Schematic representation of several interface systems including homogenous phases with an ideal interface, random media and a multilayer system

Energy deposition is governed by the optical properties and the energy absorbed by the sample contributes to signal formation. Only the heat generated within one thermal diffusion length of the sample will be able to reach the surface and influence the signal detected there. The thermal diffusion length, however, is a function not only of the material properties but also of the modulation frequency, and it decreases with increasing modulation frequency. Thus, a smaller depth is probed in this case. This is the basis of the depth profiling capability of this method.

1.3.2 Random Media

The photothermal or photoacoustic signal depends on the energy absorbed by the sample, as mentioned previously. Therefore, materials with low optical quality such as rough samples or opaque substrates can be investigated. Disordered structures such as amorphous or sintered materials, as shown schematically in Fig. 1.4, play an increasing role in materials science. Thus, there is considerable interest in describing the properties of such random media. New concepts in the theoretical treatment of diffusion in random media like the concept of fractal geometry to the description of rough surfaces and to their thermal behavior when acting as a heat source have been developed. To analyze heat diffusion in random structures, the dimensionality of the diffusion process is introduced and is discussed in the framework of percolation theory. It is shown that geometrical parameters such as the fractal dimensions of the surface and network can be obtained from simple photothermal experiments. Experimental data is obtained by observation of the average surface temperature evolution at an opaque sample surface with an IR detector, after irradiation with short laser pulses.

1.3.3 Films and Layered Structures

An important application of the photothermal and photoacoustic techniques is in the analysis of thin films. The observation of thermal and acoustic wave phenomena allows the determination of thermophysical film properties, while optical properties may be obtained by varying the laser wavelength. The influence of the thermal diffusion length on the signal generation process makes depth profiling and the inspection of subsurface features possible, but limits the

photothermal analysis to a thin layer near the sample surface. These techniques are thus especially suited to thin film analysis.

In many cases, more complicated layered materials with two or more layers have to be analyzed, as indicated schematically in Fig. 1.4. One well-studied example is the characterization of ferromagnetic films and layers. The great interest in these films is due to the different magnetic properties of the films compared to the bulk material. To optimize specific properties, for example, sandwich layers with alternating magnetic properties can be produced. Several thermal wave detection techniques were applied to these ferromagnetic films for materials characterization, nondestructive evaluation of their magnetic properties and the investigation of the fundamental problems of magnetism.

Systems with complicated layered or distributed structures are often found in biological systems. Here, depth profiling by a nondestructive method is of great importance.

Improved characterization of surfaces and interfaces is of special interest, especially with regard to buried interfaces, because the information available on these transition regions is rather limited.

1.4 Applications

1.4.1 Spectroscopy

Energy deposition in the sample is determined by the wavelength dependence of the optical absorption coefficient. Due to radiationless deactivation, part of the absorbed energy is released as heat and creates the signal. As previously stated, only the heat released within a diffusion length will be detected at the surface. Thus, thermal and also acoustic properties of the sample will affect

the observed spectra and complicate their analysis. In most cases, a quantitative interpretation of the complicated signal generation and detection processes will not be possible. Therefore, the main advantage of these methods is not the quantitative signal analysis, yielding, for example, optical absorption coefficients, but the investigation of materials and layered structures with low optical quality, where conventional transmission spectroscopy cannot be applied. This is especially true for biological samples, where a depth profiling of the chromophore distribution may only be achievable using photothermal techniques.

1.4.2 Distribution of Energy

If the absorbed photon initiates a quantum process, e.g. quantum desorption, a simple quantitative analysis is possible using the law of energy conservation. Measurement of the kinetic energy of the desorbed particles using a time-of-flight technique, for example, allows the determination of the binding energy in the case of quantum desorption.

Efficient energy exchange normally leads to a thermal distribution of at least part of the energy in the irradiated region and a quantitative analysis is much more difficult. Normally, it is not possible to measure the transient temperature generated by light absorption. As a consequence, access not only to spectroscopic but also to thermophysical sample properties is limited. The situation is even more complicated if a certain part of the absorbed photon energy induces chemical reactions, while the other part contributes to the heating effect, due to effective collisional deactivation. In principle, the

amount of energy channeled into quantum processes and into energy dissipation can be determined from this kind of experiment.

1.4.3 Transport Processes

The dissipation of heat from the irradiation region can be described quantitatively and yields accurate values for the thermal diffusivities which were determined for several materials employing the multifrequency modulation technique. However, heat diffusion can also be studied in disordered and highly inhomogeneous materials. These measurements yield the experimental data needed for the development of new models for the theoretical description of inhomogeneous materials. To compare the concept with the experiment, the geometrical aspects of heat diffusion through random structures were selected. The advantage of the heat diffusion process in this respect is the fact that this transport process can be studied with a relatively simple setup in a nondestructive and noncontact experiment.

1.4.4 Nondestructive Evaluation

One of the most important and well-developed applications is that of non-destructive evaluation (NDE). This method is based on the fact that the interaction of thermal waves with faults and changes in morphology lead to signal changes, which can be used as qualitative criteria for inhomogeneities in the material. In this case, depth profiling is not only performed at a single spot, but a scan technique is employed, where either the optical beam is moved across the sample or the position of the sample is changed.

1.5 Discussion of the Literature

Since the advent of laser radiation sources, the number of papers published in the field of photoacoustic and photothermal phenomena at surfaces and in thin films has increased drastically. There are already several books available on the subject in the form of review articles written by experts or as monographs [1.1-5]. Since the Third International Topical Meeting on Photoacoustic and Photothermal Phenomena in 1983, the invited and contributed talks have been published [1.6-8]. These proceedings volumes give an intermediate review of the activities and progress in this field

REFERENCES

- 1.1 Yoh-Han Pao (ed.): *Optoacoustic Spectroscopy and Detection* (Academic, New York 1977)
- 1.2 A. Rosencwaig: *Photoacoustics and Photoacoustic Spectroscopy* (Wiley, New York 1980)
- 1.3 D.S. Kliger (ed.): *Ultrasensitive Laser Spectroscopy* (Academic, New York 1983)
- 1.4 E. Liischer, R. Korpiun, H. Coufal, R. Tilgner (eds.): *Photoacoustic Effect: Principles and Applications* (Vieweg, Braunschweig 1984)
- 1.5 V.P. Zharov, V.S. Lctokhov: *Laser Optoacoustic Spectroscopy*, Springer Ser. Opt. Sci., Vol.37 (Springer, Berlin, Heidelberg 1986)
- 1.6 J. Badoz, D. Fournier (eds.): *Photoacoustic and Photothermal Spectroscopy*, J. de Phys., Colloq. C6 (Les Editions de Physique, Les Ulis 1983)
- 1.7 L. Bertrand, P. Cielo, R. Leblanc, J.P. Monchalin, B. Mongeau (eds.): Proc. 4th Int. Topical Meeting of Photoacoustics, Thermal and Related Sciences, Can. J. Phys. 64, 1023-1344 (1985)
- 1.8 P. Hess, J. Pclzl (eds.): *Photoacoustic and Photothermal Phenomena*, Springer Ser. Opt. Sci., Vol.58 (Springer, Berlin, Heidelberg 1988)

Chapter 2

Photothermal and Photoacoustic Effects and Applications

In spectroscopy, the sample is excited with a tunable light source. In conventional spectroscopy the incident, transmitted and reflected light intensity are recorded as a function of wavelength and from the numerical difference the light absorption in the sample is calculated. If the sample is a weakly absorbing thin film, then the incident and transmitted intensity have to be measured with high precision to determine the small absorbed fraction of the incident light. In photothermal detection schemes only energy absorbed in the sample contributes towards the signal, making these techniques the method of choice for spectroscopic studies of thin films. Due to thermal diffusion, only the heat deposited within a thin layer of the surface of the sample will be detectable at the surface, a feature allows spectroscopy of weakly absorbing thin films on an absorbing substrate and optically opaque films can be addressed by photothermal techniques. Spectroscopy of thin films is, therefore, an extremely important area of application for photothermal analysis.

Since thermal diffusion, sound propagation and possibly other energy transport processes, such as charge transport or excitonic processes in semiconductors, are involved in the generation of the signal, the associated material parameters can be studied.

Compared with more conventional thermal analysis methods, photothermal analysis has the advantage of noncontact generation of a well-defined heat source at the surface or in the volume of the sample of interest. With the high time resolution of some photothermal detection schemes, the transient temperatures at a sample surface or within the volume of the sample can now

be determined in real time with very high time resolution. This allows us to study the thermal properties and the temperature dependence of other physical properties, of which phase transitions or charge distributions are just two examples. Due to the high sensitivity of many photothermal detection schemes, very low intensities suffice for excitation, hence, sample heating is negligible and temperature-sensitive samples or sample properties can be studied.

Laser induced ultrasound allows the convenient noncontact generation of high frequency ultrasonic waves in a sample. Compared to conventional ultrasonic transducers, photothermal generation is always noncontact and free of transducer ringing. Coupling of the sound pulse from the transducer into the sample, subject to acoustic impedance matching etc., in the case of a transducer is no problem with laser generated ultrasound since the sound is generated in the sample, a feature which might prove convenient when studying bulk samples. For ultrasonic analysis of thin films, the wavelength of the probing pulse should be substantially less than the sample thickness. In this case, techniques based on conventional ultrasonic transducers are cumbersome, to say the least, due to the above-mentioned acoustical problems. With a sufficiently short and powerful laser pulse, absorbed in a thin sample, ultrahigh ultrasonic frequencies are easily generated, making the photoacoustic analysis of thin films relatively straightforward.

In imaging, a large number of techniques compete with photothermal imaging and microscopy. Optical microscopy is an extremely well developed, powerful and mature analytical technique. The signal-to-noise ratio in microscopy is excellent and parallel recording and processing of a frame is state of the art.

Quite clearly, photothermal imaging with its relatively low signal-to-noise ratio and complicated signal generation and hence contrast mechanism will never be able to compete with light microscopy. Thermal wave and ultrasonic imaging of thin films are, however, two niches where photothermal imaging is becoming a powerful tool.

One of the key features of photothermal excitation is the fact that it does not require extensive sample preparation or physical contact with the sample. The same is true for a number of the detection schemes. In many applications, excitation and detection of the signal can be accomplished on the same side of the sample, enabling single sided, remote monitoring of the sample under study. This feature makes photothermal analysis a good candidate for industrial and even military applications.

A number of comprehensive books [2.1-4] have reviewed the field of photoacoustics and photothermal phenomena and there are also excellent review articles [2.5-9] which provide good coverage of the field. Advances on the status of the field can be found in special issues of journals that were dedicated to photoacoustics [2.10, 11] and the proceedings of international conferences on photoacoustics [2.12, 13]. The focus of this chapter will be to enable a prospective user of this technique to critically assess the potential of photothermal and photoacoustic methods in the analysis of thin films.

The physical principles of the signal generation process and selected detection schemes are briefly reviewed and various detection schemes are compared in detail. Typical applications in thermal analysis, ultrasonic testing and imaging of thin films are discussed and examples highlighting the advantages and drawbacks of photothermal and photoacoustic techniques are analyzed.

2.1.1 Signal Generation Process

In a prototypical photothermal experiment (Fig. 2.1) a homogeneous thin film with thickness T is excited with a modulated or pulsed light source. The light absorption in the sample can be characterized by a wavelength dependent optical absorption length $A(\lambda)$

$$A(\lambda) = \frac{1}{\beta(\lambda)} \quad 2.1$$

with $\beta(\lambda)$ the commonly used optical absorption coefficient of the sample. Due to radiationless processes, part of the absorbed energy is released as heat. With the incident energy being either modulated or pulsed, the heat generation will show corresponding time dependence. Via heat diffusion then, a temperature profile develops in the sample. For a heat source with the modulation frequency f the heat diffusion can be described by the thermal diffusion length

$$D(f) = \sqrt{\frac{k}{\pi\rho c f}} \quad 2.2$$

where k denotes the thermal conductivity, ρ the density and c the specific heat of the sample. With the thermal diffusivity

$$\alpha = \frac{k}{\rho c} \quad 2.3$$

the thermal diffusion length is a function of this material parameter and the modulation frequency

$$D(f) = \frac{\sqrt{2\alpha}}{2\pi f}$$

2.4

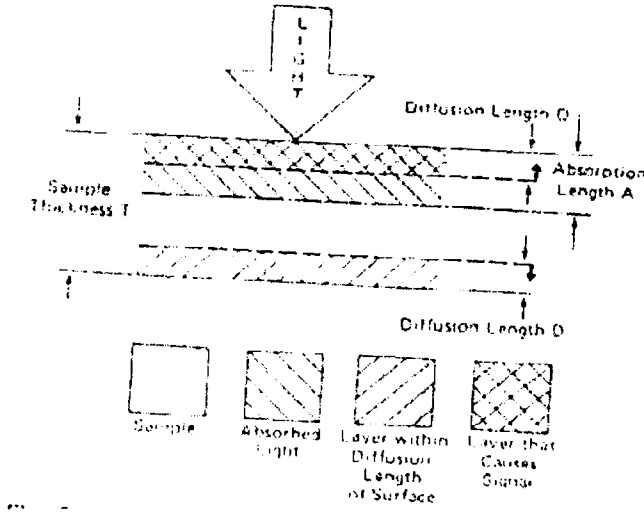


Fig 2.1 Photothermal generation process.

The amplitude of a thermal wave is attenuated by a factor of $\exp(-2\pi)$, i.e., 2×10^{-3} , when diffusing one diffusion length [2.14]. Therefore, essentially only heat generated within one thermal diffusion length of a sample surface will be able to reach this surface. If the sample is in contact with another medium, thermal waves are reflected and transmitted at the interface. Heat diffusion extends into the second medium according to (2.1,2.2) or (2.4) with the material parameters of that medium instead of the sample properties. For pulsed excitation the thermal transit time τ is the relevant parameter. The temperature at a distance l from a pulsed heat source reaches its maximum at a time τ after the excitation. For one-dimensional heat flow the thermal transit time is given by

$$\tau = \frac{l^2}{2\alpha} \quad 2.5$$

the thermal diffusion length $D(t)$, which is defined as the square root of the mean-square distance of thermal energy from the location of a transient point source of heat, at a time t after the heat pulse is the given by

$$D(t) = \sqrt{2\alpha t} \quad 2.6$$

The transient temperature profile in the sample, and where applicable also in the adjacent medium, is accompanied by a stress profile due to thermal expansion. Sound waves are hence generated in the sample, at the surface or interface and in the adjacent material. These sound waves, being essentially unattenuated in the frequency range considered here, can then propagate over long distances. If the heat generation is sufficiently localized, the surfaces or interfaces also buckle slightly.

All detection schemes that detect the temperature at the sample surface directly will have to deal with the peculiar character of thermal waves. Due to the fact that thermal waves are critically damped

- the detector has to probe the temperature within one thermal diffusion length of the excited area and

- only energy deposited within this distance is effective in signal generation.

The first restrictions can be overcome by indirect detection of the surface temperature change; sound waves generated by the photothermal phenomenon propagate essentially unattenuated over large distances. An acoustic detector can therefore be far from the illuminated area of the sample. For moderate light intensities, i.e., below the threshold for ablation of sample material, the amplitude of the observed acoustic signal will depend on the temperature

distribution in the heated sample volume and the adjacent medium, both determined by the thermal diffusion length $D(f, t)$ and the optical absorption length $A(\lambda)$. The sound wave serves as a carrier of the thermal information. Due to this diffusive character of thermal waves, information obtained by the detection of radiation induced thermal and acoustic waves is completely different from conventional optical spectra. Some of the unique features and problems of photothermal and photoacoustic spectroscopy arise from this difference.

In an optically opaque sample with thickness $T > A(\lambda)$, such as shown in Fig. 2.1, the radiation induced heating can always be observed at the illuminated side of the sample. On the back side a temperature increase is, however, only noticeable when light is absorbed within one thermal diffusion length of the back side, i.e., when the condition $T - A(\lambda) < D(f, t)$ is met. This condition is a function of material constants of the sample such as $\beta(\lambda)$, k , ρ and c but also of an experimental variable, the modulation frequency f . As mentioned above, an acoustic transducer will be able to detect a signal on either side of the sample; on the back even if there is no sizeable temperature fluctuation reaching that side! Sample thickness is, therefore, only a minor concern for photoacoustic spectroscopy. It is, however, important to remember that the sound wave serves only as a carrier of the thermal information. The amplitude of the observed acoustic signal will depend on the temperature distribution in the heated sample volume and the adjacent medium, both determined again by the thermal diffusion length $D(f, t)$ and the optical absorption length $A(\lambda)$. For spectroscopy, therefore, the relation between these two parameters has to be analyzed.

Whenever the thermal diffusion length $D(f, t)$ is larger than the optical absorption length $A(\lambda)$, $D(f, t) > A(\lambda)$, and the sample thickness T is larger than the absorption length, $T > A(\lambda)$, all the incident energy is absorbed and contributes to the observed signal. A small variation of the absorption coefficient in this case does not change the observed signal at all. The signal is *saturated* and the observed signal is proportional to the incident energy and $(1 - R)$, R being the reflectivity of the sample. This condition can be avoided by using a thin sample or by increasing the modulation frequency until $D(f, t) < A(\lambda)$ is achieved.

A sample with an optical absorption length smaller than the sample thickness, $A(\lambda) < T$, absorbs all the incident light, hence no light is transmitted. Such an opaque sample is not accessible to conventional transmission spectroscopy. If the thermal diffusion length $D(f, t)$ is, however, smaller than the optical absorption length $A(\lambda)$, $D(f, t) < A(\lambda)$, the energy deposited within this thermal diffusion length is proportional to the absorption coefficient β of the sample. Because the thermal diffusion length decreases with increasing modulation frequency according to (2.2), this condition can, at least in principle, be fulfilled by modulating at a high enough frequency. Photothermal spectroscopy thus allows the recording of *spectra of opaque samples*.

At very high modulation frequencies, only light absorbed in the surface layer contributes to the signal. When using a lower modulation frequency the same surface layer and the adjacent layer generate the signal. By comparing spectra at various modulation frequencies, therefore, surface absorption can be readily distinguished from bulk absorption. In principle, the *depth profile* of a layered structure can thus be obtained in a nondestructive manner.

Spectroscopy of Thermally Thick Sample D < T

	Condition	Optically	Signal
I	$A \ll D$	Opaque	$(1-R)$ None
II	$D \ll A \ll T \ll D$	Opaque	$\beta(1-R)$ None
III	$T \ll A \ll T$	Opaque	$\beta(1-R)$ $\frac{1}{2}(1-R)$
IV	$T \ll A$	Transparent	$\beta(1-R)$ $\beta(1-R)$

Fig 2.2 Schematic of photothermal signal generation process in a thermally thick sample as a function of Absorption length A. The relationship between Thermal diffusion length D and sample thickness T for an increasing A(I-IV) is shown. For these cases the variation in PT signal with Optical reflection coefficient R and absorption coefficient β is given for detection on the front and back sides respectively

In conventional optical transmission spectroscopy, the path length along which absorption occurs has to be known to allow a determination of the absorption



coefficient, a task that can be cumbersome for rough samples, fibers or powders. In photothermal and photoacoustic spectroscopy, however, it is sufficient to ensure that the thermal diffusion length is smaller than the relevant sample dimension such as grain size or fiber diameter, to obtain a qualitative absorption spectrum. For many practical applications a qualitative analysis is sufficient, in which case *no sample preparation* is required. For quantitative analysis, however, and also in PT spectroscopy, extensive calibration procedures are required.

Spectroscopy of Optically Opaque Sample $A < T$

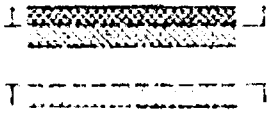
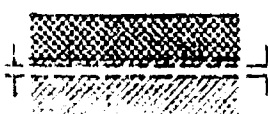
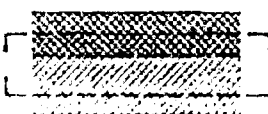
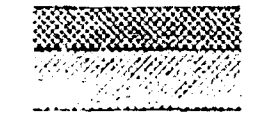
	Condition	Thermally	Signal
I 	$D \ll A$	Opaque	$\beta(1-R)$ None
II 	$A \ll D \ll T-A$	Opaque	$(1-R)$ None
III 	$T-A < D < T$	Opaque	$(1-R)$ $\frac{1}{D} (1-R)$
IV 	$T \ll D$	Transparent	$(1-R)$ $(1-R)$

Fig 2.3 Schematic of photothermal signal generation process in a thermally thick sample as a function of thermal diffusion length D . The relationship between Optical absorption length A and sample thickness T for an increasing D (I-IV) is shown. For these cases the variation in PT signal with Optical reflection coefficient R and absorption coefficient β is given for detection on the front and back sides respectively

In spectroscopy, samples with a wavelength-variable absorption coefficient are, of course, of particular interest. Different parts of the spectrum might then have an absorption length $A(\lambda)$ that could vary from larger than the selected

thermal diffusion length down to much shorter (Fig. 2.2). In this case, parts of the spectrum where $D(f, t) > A(\lambda)$, i.e., with a large absorption coefficient β , will be saturated. On the other hand, the thermal diffusion length $D(f, t)$ is a function of the modulation frequency and the thermal properties of the sample. According to the above considerations, spectra of the same sample will be dependent on the modulation frequency (Fig. 2.3). Furthermore, spectra of samples with identical optical but different thermal properties might be quite different. The same holds true for samples with identical light absorption but different fluorescence yields and therefore different heat generation. Photothermal and photoacoustic spectroscopy thus requires particular care in the selection of the modulation frequency, careful consideration of thermal sample parameters and thickness and an understanding of the signal generation process.

Such a scheme of experimentation provides several interesting special features, which make PT Spectroscopy a very attractive tool for the Chemist, the Physicist, the Materials Scientist and even the industrialist [2.130,131].

These features include

- a) the basic simplicity of the experimental set up,
- b) the convenience of studying samples in a variety of physical forms - crystals, powders, thin films, liquids etc.,
- c) the possibility of investigating opaque materials,
- d) the feasibility of direct measurement nonradiative lifetimes,
- e) the ability to gather information from sub-surface layers,

- f) the absence of stringent requirement on sample preparation and
- g) the scope to obtain information on thermal parameters of the sample.

In fact this technique has been successfully used in a wide variety of applications ranging from semiconductor characterization to eye-lens degradation studies.

2.1.2 Detection Methods

Radiation induced transient effects, thermal as well as mechanical, have been studied for quite some time. Determining the temperature or the energy of a sample has traditionally been the domain of thermometry and calorimetry. Radiation induced mechanical effects were studied using interferometry or ultrasonic transducers. In the last few years interest in radiation induced thermal and acoustic processes has increased substantially, largely due to scientific and industrial applications of lasers. The interaction of electromagnetic radiation with matter causes absorption, emission, and scattering of radiation. Except for emission and scattering, the absorbed electromagnetic energy is converted to heat by various nonradiative processes and induces changes in temperature, pressure, and refractive index of the medium. In photothermal spectroscopy, the effects caused by these changes are monitored by various methods [2.130-140]. The discovery of the photothermal effect dates back to Bell's discovery of the photoacoustic effect in 1880 [2.141], but it is after the invention of the laser that the photothermal spectroscopies became popular. A number of classical detection schemes were adapted for this particular type of application and new detection methods were

developed. Detectors tie into various stages of the signal generation chain described above. In photothermal detection schemes the radiation induced temperature increase in the sample or at the sample surface is monitored by measuring either the temperature directly or a temperature-dependent property of the sample or of the adjacent medium. Photo- and optoacoustic methods detect the acoustic waves caused by the radiation induced heating of the sample itself or a gas or a liquid that is in thermal and/or acoustical contact with the sample. For experiments with the emphasis on surface temperature, classical temperature sensors such as thermocouples are clearly the method of choice because they are easy to calibrate and convenient to use. For spectroscopic measurements, however, sensitivity and convenient coupling of the detector to the sample are the main concern.

The transient heating of a pyroelectric material can, for example, be detected via the induced electrical charge or current. As a matter of fact, many commercially available laser power meters function on this basis. A variation of this technique uses a pyroelectric calorimeter as the substrate for the sample of interest.

In contrast, photothermal radiometry can be utilized with bulk samples and is, moreover, a noncontact technique. Blackbody radiation from the sample is imaged onto a suitable infrared detector [2.19]. A change in surface temperature then effects a change of the observed signal. According to the Stefan - Boltzmann law, the total radiant power of the emitted blackbody radiation is proportional to the fourth power of the temperature of the sample. The radiometry signal, therefore, increases dramatically with increasing base temperature of the sample. This unique feature, together with the fact that

remote, single-ended, noncontact probing of a moving sample can be readily implemented, makes photothermal radiometry the ideal choice for process monitoring of thin films, in vacuum systems, in hostile atmospheres or at high temperatures. Infrared detectors require, however, cryogenic cooling to reach acceptable sensitivities. High sensitivity of the detector is typically accompanied by low time resolution. A sizeable number of detection schemes are based on particles emitted from the sample surface. Electrons [2.20] and atoms [2.21] emitted from a surface that is heated by a short laser pulse have been analyzed to derive the time-dependent surface temperature of the sample. Laser induced desorption of adsorbates [2.22, 23] from a surface or the analysis of the products of a photothermal reaction during laser-assisted chemical deposition of a metal [2.24] has been used successfully to measure surface temperatures. Most of these methods are of limited general utility only, they require UHV conditions, are restricted to few types of samples and are surface specific.

A large number of techniques utilize a *probe laser* to detect thermal effects caused by another light source. The power of the probe laser is typically orders of magnitude smaller than that of the excitation source and different wavelengths are commonly used. A change in temperature in the sample or the adjacent medium is associated with a change in the refractive index of that material. This change in refractive index causes a change in the reflection or transmission of the probe laser [2.25]. Recently, variations of this technique [2.26, 27] achieved a time resolution of the order of 10 ps. The refractive index gradient caused by the temperature gradient in the sample or the adjacent medium forms a transient thermal lens capable of deflecting a

probe laser [2.28]. The same is true for the surface buckling due to localized heating [2.29]. In a similar fashion, acoustic wave fronts give rise to refractive index gradients, and these, along with surface displacement due to acoustic waves can be probed by lasers or other optical techniques [2.30]. All probe laser techniques have the advantage of optical excitation and probing and are therefore noncontact techniques. They do require, however, careful alignment of two lasers, and optically flat samples; criteria that are fairly easy to meet with thin films vacuum deposited on to flat substrates. A large number of publications in the semiconductor area report the use of photothermal deflection schemes to determine the properties of thin films on wafer substrates.

Piezoelectric transducers [2.31], attached to the sample under study convert the sound waves that are generated in the sample into an easily recorded electrical signal. Their main drawback is the requirement of good mechanical contact with the sample and problems inherent in acoustic detection, such as matching of the acoustic impedance of sample and transducer, susceptibility to acoustic noise and trade-offs between sensitivity and time resolution. Transducers using a change in capacitance or inductance [2.32] between sample surface and a reference electrode or inductor to monitor the surface displacement overcome many of the disadvantages of conventional piezoelectric ultrasonic transducers. The main area of application of ultrasonic detection of photothermal transient signals is in ultrasonic material testing; its use in spectroscopy is limited to weakly absorbing samples such as adsorbates or transparent materials. The same holds true for special transducers employed in the detection of surface

acoustic waves [2.33]. If the sample can be in contact with a gas atmosphere, *microphones* are frequently used for detection (see, for example, [2.2]). Besides requiring a gas-filled cell to contain the sample, the frequency range of microphones is rather limited and the suppression of acoustic noise imposes restraints on such systems.

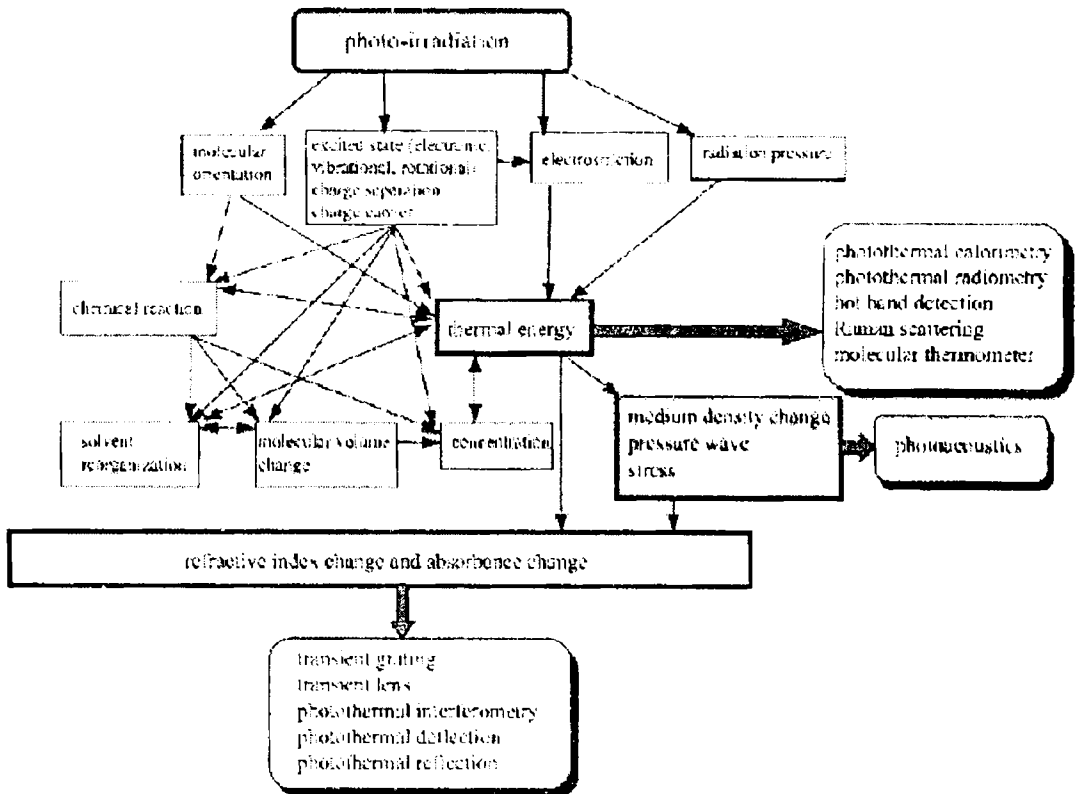


Fig 2.4 Various changes in the medium can thus be monitored by photothermal methods in order to quantify the effects of the temperature rise upon radiationless deactivation

As shown in Fig 2.4 the temperature rise is measured by laser calorimetry, pressure change is sensed by direct and indirect photoacoustic effects, changes

of refractive index are detected by probe beam refraction and diffraction, and surface deformation is quantified by probe beam deflection and optical interference [132,134,136–138]. Furthermore, thermal emission is detected by photothermal radiometry, while reflectivity/absorptivity change is sensed by transient thermal reflectance, transient piezo-reflectance, and transmission measurement. The photothermal method has a number of merits compared with other methods [132,134,136–138]. It is highly sensitive and applicable to different types of materials (gas, liquid, liquid crystal, and solid), transparent and opaque. It can be used in vacuum and in air, and with samples of arbitrary shape. Radiation of any wavelength can be used (radio frequency, microwave, IR, visible, UV, and X-ray, etc.).

Lens spectroscopy [133,134,136,138,140]

Transient lens [TrL] (also known as photothermal lens, thermal blooming, thermal lens [TL], thermal lensing, time-resolved thermal lens). When a sample is excited with a pump beam that has a spatially Gaussian form, the profile of the material response to the light should also be Gaussian. If the refractive index or the absorbance is varied by photoexcitation, its behavior may be written as in equation below

$$n(r,t) = n_0 - \delta n(t) \exp(-r^2/w^2)$$

where w is the radius of the excitation beam and r is the distance from the excitation beam axis. The energy released by nonradiative transitions from excited states heats up the material, and the spatial profile becomes Gaussian. The temperature increase leads to a decrease in the density with corresponding change of the refractive index [141]. A similar shape of temperature distribution in a cylindrical sample tube can be achieved even by uniform

illumination of the sample because of the heat flow to the sample wall (similar to *photothermal deflection*). The expansion (or focusing) of the light at the central portion of the Gaussian profile can be detected as a change of the spatial profile of the beam or the beam density through a pinhole placed in the far (or near) field leading to the transient lens signal. The origin of a transient lens signal is the refractive index change and the terms are obtained by replacing “grating” by “lens” in the above definitions. Absorption contributions (transient absorption and transient bleach) are also included in the transient lens signal, although the main contribution of the transient absorption is to decrease the probe light intensity.

Photoinduced acoustic spectroscopy [130,133,134,136,139]

Photoacoustic spectroscopy [PAS] (also known as optothermal spectroscopy, photoacoustic calorimetry, thermal-wave spectroscopy, resonant laser photoacoustics). Detects photogenerated acoustic waves. The generation is achieved either by amplitude modulation (photoacoustic spectroscopy, PAS) or by a pulse (laser-induced optoacoustic spectroscopy, LIOAS, or photoacoustic calorimetry, PAC). The pressure wave after photoirradiation is induced not only through the thermal expansion, but also through other effects such as radiation pressure, *electrostriction*, thermoelastic expansion, molecular volume change, molecular orientation, gas evolution, boiling, *ablation*, *optical breakdown*. The separation of the thermal contribution from other sources may be achieved by measuring the pressure wave under different conditions, such as a different matrix, temperature, polarization of the excitation light, and excitation wavelength. However, the complete separation is very difficult to obtain experimentally and only few examples have been reported thus far.

Therefore, specific names such as volume acoustic, ablation acoustic have not been used so far. This method was previously called optoacoustic spectroscopy, but since this name is confusing (acousto-optic effect), photoacoustic spectroscopy is preferred. A photoacoustic spectrum consists of a plot of the intensity of the acoustic signal detected by a microphone or a “piezoelectric” detector, against the excitation wavelength or another quantity related to the photon energy of the modulated excitation. Experimentally, there are many versions of this spectroscopy. Designs (resonance condition, shape, etc.) of the cell, detectors, and excitation methods are subject of modifications.

Photothermal radiometry [133,136,137]

(Pulsed) photothermal radiometry (also known as back-scattering photothermal radiometry, direct calorimetry, modulated black-body radiation, Planck radiation detection, radiometric spectroscopy, thermometric method, thermal emission detection, thermal radiation detection, transient IR detection, transmission photothermal radiometry). Infrared (IR) radiation associated with sample heating is detected by an IR detector. The source of IR irradiation is treated as a black-body emitter. According to the Stefan–Boltzmann law, the radiant exitance (or emitted radiant flux) of a black body, M_{bb} , is proportional to the fourth power of the temperature, T , over an infinite spectral detection bandwidth:

$$M_{bb} = \sigma T^4 \quad \text{where}$$

$\sigma = 2 \pi^5 k^4 / 15 h^3 c_0^2 = 5.670 51 (19) \times 10^{-8} \text{ W m}^{-2} \text{ K}^{-4}$ is the Stefan–Boltzmann constant. In real IR emitters, this equation is replaced by:

$M = \varepsilon \sigma T^4$ where ε is the emittance, a material property. Hence the relative change in radiant excittance, M , arising from a temperature change T induced by photoirradiation is, for emittance, $\delta M(T)/M(T) = 4\delta T/T$.

Photothermal calorimetry [133,134,136,137]

It is also known as transient thermography. A temperature change after photoexcitation is directly measured by using, e.g., *thermocouples*, *thermistors*, or *pyroelectric transducers*.

Photothermal interferometry [133,136,137]

Interferometric photothermal displacement, interferometry, phase-fluctuation heterodyne interferometry, phase-fluctuation optical heterodyne spectroscopy, phase-sensitive optical heterodyne spectrum, photothermal interference, photothermal phase-shift spectroscopy are other popular terminology for this. The phase of a monochromatic radiation beam passing through the light-irradiated region relative to the phase of a light beam passing through the reference arm is detected as a change in power at a light detector. Michelson, Mach--Zehnder, Jamin, and Fabry--Perot interferometers are frequently used. The phase difference originates in a refractive index change. The source and the applications are similar to the *grating spectroscopy* and *lens spectroscopy*.

Photothermal deflection [133,136,137]

Photothermal deflection is other wise known as acousto-optical beam deflection, mirage detection, mirage effect, optical probing of the acoustic

refractive gradient, photothermal beam deflection, surface photothermal deflection, probe beam refraction, surface photothermo-elastic effect, transverse mirage effect etc. The photothermal deflection method is defined by a detection of the deflection of a probe beam induced by photoirradiation of a sample. There are two sources of the photothermal deflection effect. One is induced by crossing a nonuniform spatial profile of the refractive index gradient after a photothermal excitation, which is often referred as mirage effect or optical probing of the acoustic refractive gradient. When the temperature change in the medium is nonuniform, it results in a refractive index gradient. The temperature change could be also established by thermal diffusion. The spatial gradient in the refractive index changes the propagation direction of the probe beam. Spatially nonuniform refractive index distribution arises from many sources besides the thermal effect. The other source comes from topographical deformation of the surface, on which the probe beam is deflected. This effect may be called (surface) photothermo-elastic effect or surface photothermal deflection.

Some of the popular detection schemes for deflection are listed below

collinear deflection method

Photothermal deflection method that uses a probe beam that is collinear or quasi-collinear with the pump beam.

(direct) mirage effect

Probe-beam deflection for a probe light that passes on the same side of the photoilluminated interface, which is induced by a nonuniform spatial profile of the refractive index gradient.

reverse mirage effect

Probe-beam deflection for a probe light that passes on the opposite side of the photoilluminated interface.

surface (photothermal) deflection

Probe beam deflected from a surface changes direction when heterogeneous expansion occurs on the surface.

transverse deflection method

Photothermal deflection method in which the probe-beam propagation direction is perpendicular to that of the pump beam.

Photothermal reflection change [136,137]

Photothermal reflection change (surface optical reflectance due to the photothermal effect, thermoreflectance detection). Change of light intensity reflected from the surface due to the photothermal effect. Similar to *photothermal deflection*, there are two types of signal sources. One effect is produced by the temperature- dependent reflectivity of a surface. Similar to other refractive-index-sensitive spectroscopies, not only the thermal effect but also other sources of refractive index change and absorbance change can also affect the reflection. The other source comes from topographical deformation of the surface, on which the probe beam is deflected. This effect may be called “(surface) photothermal topographical deflection” or photothermal surface reflection.

An evaluation of the pros and cons of the major photothermal and photoacoustic detection schemes shows that each of the detectors has its merits, making it the prime choice for certain applications or a particular type of sample. As should be evident from the above discussion, the signal generation and detection process can be rather complicated and may involve a

large number of individual processes. A substantial loss in sensitivity and time resolution is associated with each diffusion or conversion process. These losses become particularly significant when detection occurs at the end of the signal generation chain. Microphone detection in particular has low signal generation efficiency and time resolution and requires the most elaborate theoretical models for the quantitative interpretation of the observed signals. However, even with these limitations, high signal-to-noise spectra can be obtained using a microphone. The spectra can be readily interpreted due to the long history and large body of literature associated with this approach. If highest time resolution is required for studies of extremely thin films, then pyro- and piezoelectric deflection schemes excel. Photothermal deflection schemes seem to be most popular in all applications dealing with semiconductor wafers and thin films on these wafers, i.e., samples of optical quality.

2.1.3 Instrumentation

A typical photothermal setup comprises a suitable light source, the detector and signal recovery electronics (Fig. 2.5). It is important to keep in mind that the signal generation process involves optical, thermal and possibly acoustic properties of the sample.

In spectroscopy, it is important, for example, to eliminate thermal and acoustic artifacts in the recorded spectra. To account for the wavelength dependence of the source, the thermal parameters of the sample and the characteristics of the detector, a reference sample is normally employed. Reference data are obtained in a single beam spectrometer before or after the sample spectrum or, in a dual beam arrangement, simultaneously with the

sample spectrum. Due to the strong influence of the modulation frequency, it is imperative to record both data sets at the same modulation frequency with samples of identical or well-known thermal characteristics.

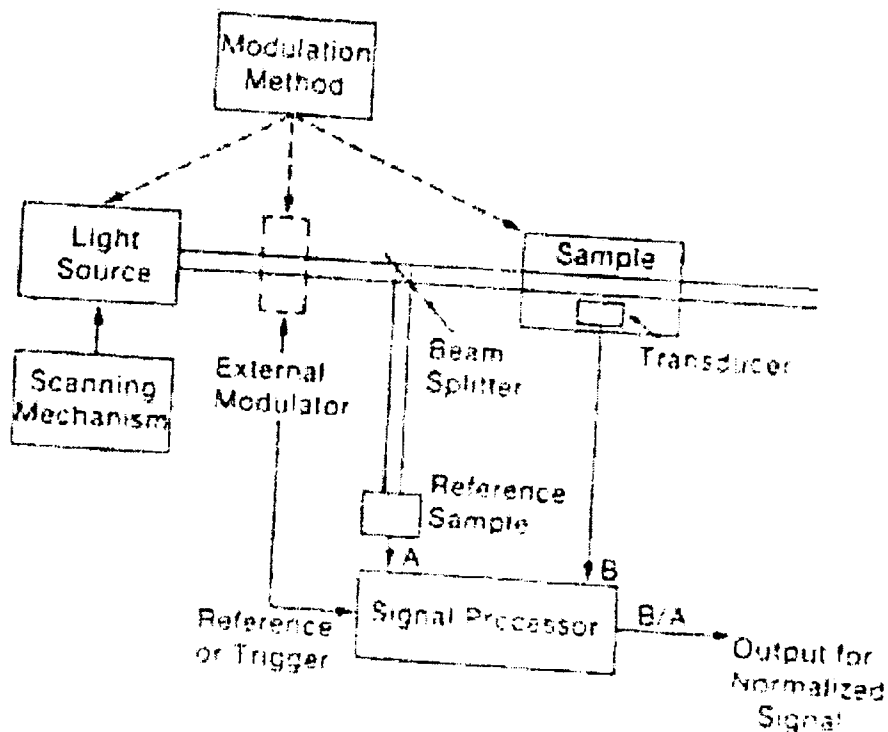


Fig 2.5 A generic photothermal spectrometer

Similarly, for a thermal and acoustic analysis of the sample it is necessary to eliminate the influence of optical sample parameters and distinguish between the thermal and acoustical signal. The thermal diffusion process is quite different from sound propagation, thermal waves are critically damped within one wavelength to less than 1% of their initial amplitude; sound waves, however, propagate at the frequencies considered here over long

distances. The thermal signal can therefore be readily suppressed by a simple delay line. If this is not feasible, the well-defined transit time of a sound pulse can then be utilized to discriminate electronically against the thermal signal by time gating techniques. Thermal diffusion across an interface depends on the thermal diffusivities of both materials; sound transmission is a function of their respective acoustic impedances. Couplers and filters can therefore be designed that transmit thermal but no acoustic energy. Another important difference between thermal and sound waves of the same frequency is the much longer wavelength of sound waves. For most thin film applications, the wavelength of the interrogating wave should be of the order of the film thickness. The ultrasonic analysis of a film requires, therefore, considerably higher modulation frequencies than the thermal analysis of the same film. The cost of high frequency electronics increases dramatically with increasing frequency, making photothermal analysis a less costly alternative and worth looking into.

The light source in a typical experiment will be intensity modulated by a suitable means, such as current modulation of a lamp or a mechanical chopper. Wavelength or polarization modulations are advantageous when small absorptions superimposed on large background absorption are of interest. Where applicable, modulation of the absorption properties of the sample (Stark modulation) or other physical parameters (temperature) that allow modulation of the sample characteristics can be used.

Most commonly, sinusoidal or square wave modulation of the incident light intensity is employed [2.1-4]. In this case a lock-in amplifier is the appropriate tool for signal recovery. It should be emphasized that if a source

of constant intensity is modulated in this way the energy per excitation cycle decreases with increasing modulation frequency. The signal at high modulation frequencies, desirable, for example, because of the above saturation considerations, will then be extremely weak. Excitation with a short light pulse has the advantage of generating a higher surface temperature than with the same energy in a longer pulse or a periodic excitation, due to the fact that heat loss during the short pulse can be neglected. This results in a superior signal/noise ratio but might damage the sample irreversibly or affect temperature-sensitive sample properties. With pulsed excitation, box-car integrators are frequently used to monitor the signal in a small time window [2.34]. Transient digitizers enable one to obtain the complete time domain signal and, if desired, transform this into the frequency domain [2.35]. Recently, another modulation scheme has emerged using noise modulation [2.36] of the light source and transient digitizers for data recording. Time domain type results can then be obtained from the data by cross correlation [2.37] and frequency domain data by Fourier analysis [2.35]. The advantage of this new technique is that many modulation frequencies are probed simultaneously and therefore depth profiles can be obtained in a small fraction of the time required for recording spectra subsequently at several modulation frequencies. If we assume a light source of constant intensity that is modulated by an external modulator, noise modulation makes more efficient use of the light intensity than any other modulation scheme.

Photoacoustic detection is frequently employed in FT-IR studies of thin films or powders. Here the intensity modulation due to the interference fringes can be utilized when a commercial rapid scanning FT-IR spectrometer is used as

the light source. One should, however, be aware of the fact that this results in a much lower modulation frequency for the long wavelength side of the spectra as compared to the short wavelength part of the same spectrum. Therefore a spectrum might be partially distorted for high wave numbers due to saturation. With conventional light sources, only a limited spectral, time and depth resolution can be obtained. Nevertheless, high sensitivity, instrumental simplicity and minimal sample preparation make photothermal detection an interesting alternative to more established techniques, such as diffuse or internal reflectance spectroscopy [2.38]. Photothermal detection, however, offers a unique combination of advantages that are not available with other techniques when combined with the high spectral and time resolution possible with laser excitation: This is evident for spectroscopy, but is also true for thermal and ultrasonic analysis of thin films when using photothermal effects to generate the probe that interrogates the sample under study. Photothermal methods possess what is known as the zero-baseline advantage. In plain language, this means signals are generated only if there is an optical absorption event and subsequent conversion to thermal-wave energy above an otherwise zero background signal, even in the presence of large, non-converted optical fields. This feature, coupled with the strong spatial damping of optically generated thermal waves in the vicinity of photon deposition followed by coherent thermal conversion, can yield extremely localized detection of ultraweak absorptions in thin films and fluids at unprecedented sensitivity limits⁶ for absorptances, in the range below 10^{-6} . Because of the extraordinary improvement in dynamic range measurements, significant new physics and industrial and clinical applications have become possible in the past 30 years

as a result of combinations of the unique abilities of photothermal techniques and instruments. The applications below are typical of the considerable potential of emerging photothermal diagnostic technologies to successfully address widely disparate scientific and engineering disciplines, including photonic materials science, metallurgical non-destructive depth profilometry, and semiconductor thermoelectronic imaging, through signal-generation processes that yield results that are far superior to those that can be obtained using purely optical techniques. In the following section, examples will be presented underlining some of the above features.

2.2 Spectroscopy of Thin Films

Due to its peculiar signal generation and detection process, photothermal spectroscopy has several unique features and is quite different from conventional transmission spectroscopy. Photothermal spectra represent only heat released within the thermal diffusion length of the sample surface. As outlined above this makes photothermal spectroscopy the method of choice for thin film studies. Additional advantages of photothermal detection methods are (1) that they are not affected by scattered light and (2) the depth profiling capability of this technique. If these techniques are so powerful why are they not dominant in spectroscopy? Quite clearly, the fact that thermal and acoustic properties of the sample affect the observed spectra complicate the interpretation of the data considerably. Reference samples with well-defined optical, thermal and acoustical properties are required [2.39] and photothermal spectra of two samples with identical optical absorption are identical only if the samples have identical thermal and acoustic properties, the same depth profile, the same

quantum efficiency for radiationless de-excitation and are recorded at the same modulation frequency. These complications let photothermal spectroscopy complement conventional techniques but not replace them [2.40].

2.2.1 Semiconducting Films

Semiconducting powders and wafers have been used for quite some time to demonstrate the power of photoacoustic detection, mainly using air-filled cells and microphones for detection. More recently, photothermal deflection schemes have been introduced into this field. With semiconductors being well defined and well understood samples, these experiments served at first to develop an understanding of the photoacoustic and later also of the photothermal signal generation process. Later, the advantages of these techniques over conventional spectroscopies were demonstrated and helped to establish credibility in this field. A large number of publications, reviewed for example in [2.4], show that the method is now well accepted in the semiconductor area and methods have been developed to derive the optical absorption coefficient from the data [2.41, 42]. Some of the key issues in semiconductor samples are associated with impurities and defects. Semiconductors are characterized by their band gap, and these impurities and defects cause additional states in the band gap that affect the electrical characteristics of semiconductor devices. Due to the dramatic change in optical density in the region close to the edge of the band, conventional optical spectroscopies with their rather limited dynamic range and very high background are not too suitable for this type of application. Many of the samples of interest are amorphous films, which typically have a rough surface. With conventional transmission spectroscopy, numerical corrections

have to be introduced to account for the scattered light. Measurements of the diffuse reflectance are, however, by no means trivial, cause systematic errors in these corrections of the measured optical transmission. Photothermal methods excel here and enable one to determine the spatial distribution of the defects and to study the relaxation mechanisms of electrons from optically excited states to the ground state via nonradiative pathways, an issue of burning interest for photovoltaic and solid state laser devices.

The emphasis in the last few years has been on studies of amorphous semiconductor films. Due to interest in xerography and photovoltaics, a number of experiments focus on a-Si. Photothermal spectra complement a xerographic analysis of the material and [2.43], enable the effect of compensation on defects to be studied [2.44] and the derivation of the density of gap states in a-Si to be ascertained [2.45-50]. Photoacoustic studies on other systems, many of them reported during the *International Conferences on Amorphous and Liquid Semiconductors*, demonstrate how photothermal deflection spectroscopy can be utilized in the study of amorphous Si-Ge alloys [2.51], the doping of a-Si films [2.52, 53], the optical properties of a-Ge films [2.54, 55] or materials such as a-SiN [2.56, 57] or CuInSe₂[2.58]. Systems such as Cd_{1-x}Zn_xS have been studied with photothermal deflection spectroscopy and the results compared with those of conventional transmission spectroscopy [2.59]. Electroluminescent thin films, otherwise accessible only to sophisticated techniques such as time resolved fluorescence measurements, have been extensively studied with photoacoustic and photothermal methods [2.60-62].

As is evident from the large number of recent publications, photoacoustic and photothermal detection schemes are now at a point where they are able to make unique contributions towards the understanding of thin semiconducting films.

The measurement of photoexcited excess carrier lifetimes (both surface and bulk) and carrier diffusion coefficients in semiconductors is very useful in the characterization of the quality of semiconductor materials and in evaluating the performance of working semiconductor devices. The non-contact method of frequency-domain photothermal radiometry (PTR), is promising for remote on-line or off-line impurity/electronic defect diagnostics.

Semiconductor nanostructures are of current topical interest due to the fact that their properties undergo considerable modification from those of the bulk due to quantum confinement effects. Nanoclusters of these materials embedded in dielectric hosts are known to behave as quantum dots, described rightly as practical examples of 'particle-in-a-box'. Such structures can be prepared by several chemical and physical methods such as ion-exchange reactions, molecular beam epitaxy, ion-implantation, sol-gel techniques etc .

Quantum confinement leads to alterations in the band structure of the bulk. It also systematically shifts the band edge towards higher energy as the quantum dots get smaller and smaller. This is known as the signature 'blue shift' in optical absorption and the process as 'bandgap engineering'.

The physical processes in such structures are governed by their excitonic energy levels, which are difficult to be probed by optical spectroscopy due

their proximity to band-edge absorption, as the optical densities tend to be very large and transmission poor. However, we may seek a technique that directly measures the absorbed energy to investigate these systems. PT spectroscopy has been used successfully to obtain valuable spectroscopic information in such cases.

2.2.2 Dielectric and Metallic Films

Dielectric and metallic thin films are another area where photothermal detection methods can be advantageous. An example is the first direct measurement of the optical absorption of polyacetylene [2.63]. As a result of its complicated fibrillar morphology, polyacetylene is a very complex optical medium. Optical absorption spectra that can be compared with various theoretical models had to be inferred from transmission spectra of thin films. It was found that these films scatter several percent of the incident radiation diffusely. Transmission measurements cannot distinguish between scattering and absorption. Therefore absorption constants derived from transmission measurements, even when using specular or diffuse reflectance data for correction, can exhibit systematic errors that make a comparison between various theoretical models almost arbitrary. Photothermal deflection spectra provided the first reliable measurement of the absorption edge of polyacetylene and showed a Urbach-type behavior.

Electrode supported films are of considerable interest in electrochemical studies. One problem with this type of sample is that the sample is deposited onto a metal. Since the amplitude of the light intensity vanishes close to the metal, conventional spectroscopies suffer from a lack of sensitivity. This effect was

clearly seen in FT-IR studies of Prussian Blue and cupric hexacyanoferrate on various electrodes [2.64]. In another experiment [2.65] the distance between a silver surface and the chromophore was varied using a varying number of transparent Langmuir-Blodgett spacer layers. Thus the amplitude of the electric field vector of the standing light wave in front of the silver was actually mapped.

Many of the problems in electrochemistry are usually addressed *ex situ* with surface scientific methods requiring ultrahigh vacuum. *Ex situ* transmission and reflection measurements complement these experiments. To ensure that the sample preparation is not introducing artifacts, *in situ* experiments are also desirable. Recording photoacoustic spectra *in situ* not only of grown electrochemical films but also monitoring the spectra of growing films was successfully done [2.66].

2.2.3 Spectroscopy of Layered Films

Photographic color reversal films with their intricate but well-defined layered structure have served as a model system to demonstrate the depth-profiling capability of photoacoustic [2.67] and photothermal [2.68] detection schemes. As discussed in Sect. 2.1.1 and shown in Fig. 2.3, with decreasing modulation frequency a thicker layer of the sample contributes towards the observed signal. With a sample such as a color reversal film, the observed spectra depend strongly on the modulation frequency and would, at least in principle, allow the reconstruction of the depth-profile, i.e., optical density as a function of wavelength and depth, of the sample.

2.2.4 Nonradiative Quantum Yield

Absorption spectroscopy is the prevalent application of photothermal and photoacoustic spectroscopy. Since radiationless de-excitation of the electronic excited state is a key step in the signal generation chain, the relevant quantum yield for nonradiative processes can be determined. To demonstrate the determination of nonradiative yields and to highlight the frequency dependence of spectra, let us consider a trilayered sample with a weakly absorbing layer 1 separated from another absorbing layer 3 by a transparent spacer layer 2. The spectra were recorded at two different modulation frequencies with a thermal detector at the back of the sample [2.69]. At a low modulation frequency, an absorption-like spectrum is observed. Light absorbed converted into heat. This heat diffuses across the sample and is detected on the back side. At high modulation frequencies the much shorter thermal diffusion length does not allow heat generated to reach the detector. Only light that is transmitted by the layer 2 and then absorbed by the layer 3 will contribute to the observed signal. The observed spectrum is, therefore, a transmission spectrum. If the structure of the film or its thermal properties are known, additional information can be derived from these spectra. The thermal diffusivity or the thickness of the spacer layer can be derived from a comparison of the signals. A more important parameter is that of the quantum yield for radiationless de-excitation. In the transmission spectrum light that has been *absorbed* by the layer 1 is missing. In the absorption spectrum, only that fraction of the light that has been *absorbed and converted into heat* contributes to the signal. The ratio of both signals is then the probability of nonradiative decay of the optically excited state. Since both signals are measured with the same detector and then

ratioed, no calibration of the detector is required to determine the absolute quantum yields. This technique allows the measurement of quantum yields of thin films and even of monolayers [2.65].

By nature, thermal diffusion waves can only be generated following conversion of some form of excitation energy to heat. For this reason, it is not surprising that photothermal signals are linearly dependent on the non-radiative quantum efficiency (or quantum yield), $\eta_{NR}(\lambda)$, of an absorbing sample at the excitation wavelength λ . The precise spectral measurement of the energetic complement of this parameter, the radiative quantum yield, $1 - \eta_{NR}(\lambda)$, is extremely important for the assessment of the optical activity (or the lack thereof) and the suitability of photonic solids or liquids as laser or optical materials within a desirable emission band. Unfortunately, the spectral measurement of $\eta_{NR}(\lambda)$ has always been difficult at best. The problem is that optical signals from such materials contain the hard-to-deconvolute $\alpha(\lambda) \eta_{NR}(\lambda)$ product (optical absorption coefficient). Ultra fast methods can be used to track down one or more specific de-excitation pathways, but they cannot track down the entire de-excitation energy manifold and they cannot track across broad spectral ranges. Photothermal spectroscopy as detailed above is capable of measuring the complementary spectrum quite easily. The key to success for this measurement is in the deconvolution of the $\alpha(\lambda) \eta_{NR}(\lambda)$ product spectrum through signals generated by the same instrument.

2.3 Thermal Analysis of Thin Films

Photoacoustic and photothermal spectroscopy can be cumbersome due to the thermal diffusion step in the signal generation process. In the thermal analysis of thin films the same process is now advantageous. Photothermal excitation of a light source facilitates the implementation of a well-defined heat source for the probing of the thermal properties of thin films. The heat source requires no mechanical or thermal contact with the sample and can be tailored to the application by simply changing the temporal shape or wavelength of the light source and by changing the size and the location of the illuminated area. Combined with the high sensitivity and time resolution of many photoacoustic and photothermal detection schemes, the thermal analysis of temperature sensitive properties of extremely thin films becomes a viable proposition.

2.3.1 Thermal Diffusivity

The thermal diffusivity of a thin film can be determined by generating a transient heat source at the front of the sample and monitoring the subsequent temperature increase at the back. When using amplitude modulation of a light source to generate the heat source the amplitude or phase of the transmitted temperature wave can be analyzed [2.70]. For a film with thickness l , an amplitude decrement

$$A = \ln \frac{\Theta(0)}{\Theta(l)} \quad 2.7$$

is observed, with $\Theta(0)$ and $\Theta(l)$ being the amplitude of the temperature oscillation on the front and back of the sample. For a thin film of diffusivity α , the frequency dependence of the amplitude decrement is given by

$$A = \frac{I}{\sqrt{\alpha}} \times \sqrt{\pi f} \quad 2.8$$

In addition, a phase lag Δ , where

$$\Delta = \Phi(f) - \Phi(0) \quad 2.10$$

is observed between the temperature at the front and the back, with Φ being the phase angle between the modulated light source and the observed temperatures, with Δ being equal to A . For very thin films, however, their resolution is also insufficient. The solution to this problem is to measure at higher frequencies. From the data the thermal diffusivities of thin films can be derived using numerical models. Experimental requirements for photoacoustic diffusivity measurements of the thermal diffusivity of thin films, first introduced by *Adams and Kirkbright* [2.71], are modest. Due to the limited bandwidth of microphone detection, photothermal methods are currently dominating the field. With the sample directly coated onto a pyroelectric sensor highest time resolution can be obtained and extremely thin films can be studied [2.72-76]. However, this technique involves special sample preparation. Other methods typically require optical access to the front and the back of the sample [2.75], a problem which can be overcome by measuring the lateral heat flow in the sample [2.74]. Still another way is to determine the surface temperature as a function of time while heat diffuses from the surface of the sample into the interior. Photothermal radiometry [2.76, 77] and photothermal deflection schemes [2.78, 79] have demonstrated their utility in this type of noncontact, single-ended measurement. Even photoacoustic schemes can be adapted for samples with inaccessible back

sides [2.80] and corrections for the geometry of the cell improve accuracy considerably [2.81].

Laser excitation combined with one of the photothermal detection schemes facilitates measurements of thermal transport coefficients in thin films. Whereas frequency domain experiments are very straightforward in their interpretation, time domain experiments with pulsed light sources for excitation require extensive analytical or numerical efforts to derive transport coefficients from the observed data.

2.3.2 Film Thickness

The above discussion on thermal diffusivity assumed that the thickness of the sample can be derived by other methods. But quite clearly (2.8) can be utilized to determine the thickness of a sample with known thermal diffusivity. A large number of more conventional techniques, many of them mechanical or optical, are available to measure film thickness conveniently and with the desired precision. Most of the reported thermal thickness measurements demonstrate only the validity of models underlying the derivation of (2.8) and show that results determined with this technique are consistent with other measurements. Why bother with a technique whose accessible thickness range is severely limited by the thermal diffusion length (2.2) or (2.6)? One application might be the optical measurement of thin films on opaque substrates of low reflectivity such as SiO_2 on Si [2.82]. All of the optical measurements require an independent measurement of the refractive index of the material to derive the film thickness. By a combination of thermal and optical interferometric techniques, the thickness of the film can be determined in situ without an off-line measurement of the refractive index [2.83].

2.3.3 Phase Transitions

Heat deposited by a laser beam in a sample can increase the temperature of the sample, as discussed in Sect. 2.3.1 on thermal diffusivity or, if the sample undergoes a first-order phase transition, it can provide the latent heat of that transition without changing the temperature at all. This well-known phenomenon was first observed in the context of photoacoustics by *Florian et al.* [2.84]. Anomalies in the amplitude and the phase of the observed signal [2.85-87] were interpreted [2.88] as an oscillation of the liquid-solid phase boundary in the sample during the periodic illumination. Photoacoustic experiments have been complemented by photopyroelectric measurements of phase transitions [2.89]. These experiments on model systems established photothermal methods and the associated theory for the study of phase transitions. Most recently, these methods have been applied to the glass-crystal phase transition of semiconductors [2.90] and to real-time studies of laser annealing [2.91]. During the laser pulse, the sample, a thin tellurium film, is heated by the laser and subsequently cools down. With increasing laser fluence, the peak temperature of the film does not follow that increase due to the latent heat of the melting and boiling transition. At high time resolution the sample melts during the first part of the laser pulse and is heated all the way up to the boiling point by the remainder of the pulse. During the cool down latent heat is released during crystallization, keeping the sample temperature constant for an extended period of time. The amount of latent heat is proportional to the amount of material left after boiling off part of the film. The crystallization is, therefore, finished earlier for samples of smaller mass, i.e., samples that remained at the boiling temperature longer due to larger laser

fluence. Compared with frequency domain experiments, time resolved data do not require sophisticated models for their interpretation. Frequency domain experiments fostered the understanding of the photoacoustic signal generation process but have only limited appeal to users of conventional thermal analysis equipment. Time domain studies might, however, be very attractive tools for studies of laser induced thermal processes, such as annealing and ablation. Their high time resolution combined with excellent sensitivity enables real-time studies of single transient events which are crucial in that type of research.

2.4 Ultrasonic Analysis of Thin Films

Pulsed lasers have been used by many authors as a convenient and flexible means for the generation of ultrasound in thin films or solids; for recent reviews on this subject see [2.92-94], For the ultrasonic analysis of a thin film, the wavelength of the sound wave used to monitor the thickness of the sample and its acoustic properties should be less than the sample thickness. With a sound velocity of the order of 5×10^3 m/s, a film thickness of the order of $1 \mu\text{m}$ requires a pulse of less than 200 ps to meet this criterion. Conventional techniques are very cumbersome at the corresponding frequencies, whereas photothermal techniques are relatively straightforward.

As in the photothermal generation of a heat source the key advantage of photoacoustic generation of a sound source is the fact that the photoacoustic method requires no mechanical contact with the sample. The timing and location of the sound source can be selected by simple optical techniques and arrays of coherent sources can be readily implemented. A number of

photothermal detection schemes are based on optical probing of the sample surface [2.30]. The detection of the ultrasonic pulse can, therefore, also be without mechanical contact with the sample. For semiconductor applications this means, amongst other things, that no contamination will be introduced by a coupling medium. In addition, the excitation source as well as the detector can be scanned readily across the sample. As long as the intensity of the excitation stays well below the thresholds for evaporation or ablation of the sample, no irreversible processes are anticipated and the method can be considered truly nondestructive.

Conventional piezoelectric ceramic and single crystal transducers are excellent mechanical resonators. When stimulating such a transducer with a short pulse, its mechanical resonance is excited, causing the transducer to ring for quite some time after the pulse. The time resolution of the transducer and hence the thickness of the sample that can be studied is limited by this effect. Numerical corrections or electronic filters can compensate partially for this transducer transfer function. Piezopolymers enable one to overcome this problem due to the large internal damping of these materials [2.95] associated, however, with a much lower conversion of mechanical energy into an electrical signal.

Coupling of the transducer to the sample of interest is another issue that can be eliminated in photothermal studies. Coupling of acoustic energy is a function of the acoustic impedance of the sample and the transducer. Impedance matching can be accomplished by selecting appropriate materials and geometries. Since the choice of piezoelectric materials is rather limited, it might not be possible to match the acoustic impedance of the sample of interest by this technique. Antireflection layers, the other alternative,

unfortunately have a limited bandwidth and thus cause severe distortions in a pulsed mode. At the high frequencies desirable for thin film studies, attenuation in the coupling medium can become a serious problem. Light, however, can be readily coupled into virtually any material.

Lasers delivering nanosecond pulses have been available for quite some time at a reasonable cost. Generation of ultrasonic pulses with these lasers has, therefore, been dominating the literature, references [2.96-98] serve merely as examples of these applications. High power picosecond lasers are just becoming available commercially. The cost of picosecond lasers and the fast electronics required to take advantage of the ultrashort pulses for the analysis of thin films is, however, still rather prohibitive and maintenance of these lasers is labor intensive. Researchers [2.99, 100] have been able to take advantage of this emerging diagnostic tool.

2.5 Nondestructive Evaluation of Thin Films

In a rigorous sense, spectroscopic, thermal and ultrasonic analysis of a thin film constitute nondestructive evaluation of the material, if excitation and detection of the probing thermal and ultrasonic waves are accomplished in a nondestructive way. Evaluation in a wider sense refers here to well-developed applications that are potentially of industrial interest. Among nondestructive testing (NDT) methodologies, the diffusion-wave technique known as thermal-wave detection is growing in importance because of its ability to monitor subsurface structures and damage in materials well beyond the optical penetration depth of illumination sources, i.e., below the range of optical imaging for opaque materials. The amplitude and phase of the thermal wave in inhomogeneous materials carry information about any heat transport disruption

or change below the surface. Due to singularities in the solution of the thermal-wave inverse problem, great care must be taken in generating appropriate mathematical models for inverting these signal channels so as to yield reliable depth reconstructions of the spatially variant thermal diffusivity of the sample. In recent years, several successful attempts have been made to invert these data and thus reconstruct arbitrary thermal diffusivity (or conductivity) depth profiles. These unique feature of photothermal and photoacoustic techniques allow nondestructive mapping of geometrical, optical, thermal and, where applicable, acoustic sample properties [2.101].

2.5.1 Depth Profiling

The depth profiling capability of photothermal and photoacoustic methods has been mentioned several times in this chapter. As far as thin films, semiconducting thin films in particular, are concerned, the key issue is to distinguish surface absorption from bulk and interface absorption. This problem can be addressed by recording photothermal or photoacoustic spectra of the sample of interest at two or more modulation frequencies (2.4) or at different times after pulsed excitation (2.6). Instead of recording these spectra, data can be obtained subsequently by modulating the light source with several frequencies at the same time and using Fourier transform techniques to retrieve amplitudes and phases of the individual frequency components [2.35]. With pulsed excitation, individual time domain signals can be recorded and analyzed to distinguish contributions due to the surface and bulk of the sample. From these data then, the location of the absorber can be inferred in analogy to the procedure used in Sect. 2.2.4. These methods have been utilized to determine, for example, the surface passivation of amorphous silicon films

[2.102], to separate volume from interfacial absorption in $\text{TiO}_2/\text{SiO}_2$ multilayered films [2.103] or to establish the influence of subsurface defects on plasma-sprayed coatings [2.104].

Thermal and acoustic waves can be utilized to measure or profile temperature- or pressure-dependent properties of the thin film. Pyroelectric [2.105] and piezoelectric properties of thin films can be determined readily with these techniques. Using time resolved measurements, the depth profile of charge or field distributions can also be determined. Techniques employing laser induced thermal [2.106] or pressure pulses [2.96] are the standard methods for measurements of charge or field distributions in dielectric films [2.106]. Here, the fact that only the excited layer of the sample induces an electrical signal and that the excitation sweeps across the sample is utilized to derive the depth profile.

Polymer electrets such as β -polyvinylidene fluoride (PVDF) are frequently used in pyro- and piezoelectric transducers for the detection of radiation induced transients. The polarization profile in these materials determines the ultimate time resolution of the transducer and serves as an example to highlight some of the differences between thermal and ultrasonic analysis of a sample. The rise time of the signal is fast and excitation from the front and back of the film results in almost identical signals. This behavior would be expected for a homogeneously poled film. The photothermal response of thick unpoled layer shows that one side of the transducer has a fast rise time and the polarization reaches the bulk value only far away from the surface.

For a qualitative interpretation such as above, photothermal analysis has the advantage that for the same spatial resolution a much lower time resolution suffices. With the bandwidth of commercial electronics limited to approximately 6 GHz, and that at very substantial expense, photothermal analysis might be the method of choice rather than photoacoustic analysis. The qualitative interpretation of acoustic signals is, however, straightforward. While the pressure pulse traverses the sample, it induces a signal that is a direct measure of the polarization. The depth of the sample is directly mapped into the time dependence of the observed signal. Since thermal pulses diffuse into the sample, the main contribution to the signal is always caused by the surface. While the pulse diffuses into the sample, successive layers of the sample add up to this surface signal. The deconvolution of the observed signal into a depth profile is, however, possible by solving the heat diffusion equation for this geometry. A number of algorithms have been developed to accomplish this deconvolution [2.107],

2.5.2 Imaging

Maps of the geometrical, optical, thermal and acoustical features can be obtained by scanning the excitation across the sample or by using masks to illuminate different combinations of pixels subsequently [2.108, 109]. With optical spectroscopy being a well-developed technique and with the parallel processing of all pixels, i.e., viewing or recording of one complete picture, now being state of the art, photothermal and photoacoustic techniques cannot compete in the area of geometry and optical imaging. Thermal and acoustical images do, however, bring some of their own unique properties to bear.

Due to the complicated signal generation process, interpretation of photothermal and photoacoustic images can be ambiguous [2.110, 111]. The capability of these microscopes to image subsurface features is, however, of considerable technological interest. Defect maps in thin dielectric films [2.112], maps of radiation induced defects [2.113] or thickness measurements of Si membranes [2.114] represent just a few examples of applications in thin films. The bulk of the application is, however, in the area of integrated circuits and thin film devices. Two machines have been marketed successfully using either an electron beam [2.115] or a laser for excitation [2.116]. Detection is accomplished with an ultrasonic transducer inserted into a modified electron microscope or using laser beam deflection.

At very high resolution, SEM contrast is too poor for any conclusions to be drawn. The thermal wave picture clearly shows a subsurface fracture in the critical gap area of the head.

A number of applications in the area of semiconductor process technology can be found in the literature [144]. With the use of photothermal technologies, researchers have recently discovered that because of the rapid diffusion of photo excited carriers to the back surface of the sample, depletion conditions there can affect the entire spatial-density gradient. This has led to the emergence of a new, depth-profilometric, photothermal-electronic ("thermoelectronic") lifetime imaging technique. The photothermal signal is caused by direct coherent IR photon emission from the damaged region at the laser modulation frequency, following diffusion of photocarriers to the spot and enhanced recombination in defect states introduced by the damage. This nascent photothermal technology offers unusual sensitivity to the electronic

condition of Si wafer surfaces and intermediary bulk regions, which are thermally and optically remote to the upper 1- μ m-deep surface region, where active device processing occurs. This unique photothermal capability heralds the emergence of a potentially powerful diagnostic imaging technology for electronic, depth profilometric defect mapping in process semiconductors.

The great potential of this imaging technique would justify considerable efforts being made to improve equipment and interpretation of the images.

2.6 Miscellaneous Thin Film Applications

Besides those applications discussed previously, a number of publications have dealt with the photoacoustic or photothermal detection of surface plasmons and the use of ferromagnetic resonance phenomena to excite the sample selectively.

2.6.1 Plasmon Detection

Plasmons are collective oscillations of electrons that have been extensively studied with conventional spectroscopic techniques for quite some time. The plasmon surface polariton is extremely sensitive to surface roughness and the thickness and dielectric constant of the adjacent materials. Using conventional cell-microphone techniques to detect the nonradiative decay, it was possible to demonstrate that the sensitivity of this method is superior to conventional attenuated total reflection measurements and that the influence of the dye monolayer on the amplitude and width of the resonance was readily observed [2.117]. With the same technique, it was shown that radiative and nonradiative deexcitation channels complement each other [2.118]. With

diffraction gratings on the sample surface, instead of a prism coupler, the photothermal detection of plasmons was further enhanced [2.119.2.120]. The field enhancement at a silver surface due to resonant surface plasmon excitation has been observed [2.121] and the influence of Langmuir-Blodgett monolayer assemblies on the resonance has been studied in detail [2.122]. The attention in this field has been focused on the properties of silver island films [2.123], on the influence of dye overlayers on these island films [2.124] and on the optical absorption of small, oblate silver spheroids [2.125]. After demonstrating that photoacoustic methods duplicate results obtained with other techniques, the field then developed into experiments that provide data that cannot be observed with any other spectroscopic tool.

2.6.2 Ferromagnetic Resonance

Ferromagnetic resonance, similar to conventional optical spectroscopy, allows one to tailor the excitation such that only one layer is excited in a photoacoustic or photothermal experiment. Optically opaque layers can be penetrated by microwaves and allow the excitation of a selected layer deep in the sample.

At first, microphones were employed to detect the ferromagnetic resonance with photoacoustic techniques [2.126], photothermal deflection was explored next [2.127] and the effects of sinusoidal versus square wave modulation of the incident microwave power were compared [2.128]. Later magnetic media were imaged with these techniques, demonstrating the power of this specialized tool for the three-dimensional mapping of defects in complex layered structures [2.129].

2.7 Conclusion

Using well-prepared and characterized test samples, photoacoustic and photothermal techniques have been able to establish credibility for the experimental methods and interpretation of the data. The thermal diffusion process makes these techniques unique in that it limits the access to a thin layer at the sample surface. For thin films, however, thermal diffusion poses no major problems. It even allows the monitoring of subsurface features and the derivation of depth profiles. Due to the complex signal generation and detection process, the interpretation of photothermal and photoacoustic data is rarely unambiguous. Nevertheless, many of the applications are becoming established and photothermal and photoacoustic-analysis is nowadays able to complement conventional thin film analytical tools.

REFERENCES

- 2.1 Y. H. Pao: *Optoacoustic Spectroscopy and Detection* (Academic, New York 1977)
- 2.2 A. Rosenwaig : *Photoacoustics and Photoacoustic Spectroscopy*, Chemical Analysis, Vol. 57 (Wiley, New York 1980)
- 2.3 V. P. Zharov, V. S. Letokhov: *Laser Optoacoustic Spectroscopy*, Springer Ser. Opt. Sci., Vol. 37 (Springer, Berlin, Heidelberg 1986)
- 2.4 A. Mandelis (ed.): *Photoacoustic and Thermal Wave Phenomena in Semiconductors* (Elsevier, Amsterdam 1987)
- 2.5 C.K. N. Patel, A. C. Tam: Rev. Mod. Phys. 53, 517-550 (1981)
- 2.6 J. B. Kinney, R. H. Staley: Annu. Rev. Mater. Sci. 12, 295-321 (1982)
- 2.7 G. A. West, J. J. Barrett, D. R. Siebert, K. V. Reddy: Rev. Sci. Instrum. 54,797-817(1983)
- 2.8 Tam A. C.: Rev. Mod. Phys. 58, 381-431 (1986)
- 2.9 H. Vargas, L. C. M. Miranda: Phys. Rep. 161, 43-101 (1988)
- 2.10 Special Issue: IEEE Trans. UFFC-33 (5) (1986)
- 2.11 Special Issue: Appl. Phys. B 43, 1(1987)
- 2.12 Special Issue: Can. J. Phys. 64, 9 (1986)
- 2.13 P. Hess, J. Pelzl (eds.): *Photoacoustic and Photothermal Phenomena*, Springer Ser. Opt. Sci., Vol. 58 (Springer, Berlin, Heidelberg 1987)
- 2.14 H. S. Carslaw, J. C. Jaeger: *Conduction of Heat in Solids* (Clarendon, Oxford 1960)

- 2.15 H. Coufal: In [2.10], pp. 507-512
- 2.16 R. Zenobi, J. H. Hahn, R. N. Zare: Chem. Phys. Lett. 150, 361-365 (1988)
- 2.17 P. Baeri, S. U. Campisano, E. Rimini, J. P. Zhang: Appl. Phys. Lett. 45, 398-400(1984)
- 2.18 K. Tanaka, R. Satoh, A. Odajima: Jpn. J. Appl. Phys. 22, 592-594 (1983)
- 2.19 P. E. Nordal, S. O. Kanstadt: Phys. Ser. 20, 659-662 (1979)
- 2.20 R. T. Williams, M. N. Kabler, J. P. Long, J. C. Rife, T. R. Royt: in *Laser and Electron Beam Interactions with Solids*, ed. by B. R. Appleton, G. K. Keller (North-Holland, New York 1982) pp. 97-102.
- 2.21 B. Stritzker, A. Pospieszczyk, J. Tagle: Phys. Rev. Lett. 47, 356-368 (1981)
- 2.22 I. Hussla, H. Coufal, F. Trager, T. Chuang: Ber. Bunsenges. Phys. Chem. 90, 240-245(1986)
- 2.23 M. Buck, B. Schafer, P. Hess: Surf. Sci. 161, 245-254 (1985)
- 2.24 P. B. Comita, T. T. Kodas: Appl. Phys. Lett. 51, 2059-2061 (1987)
- 2.25 A. Rosencwaig, J. Opsal, W. L. Smith, D. L. Willenborg: Appl. Phys. Lett. 46, 1013-1015(1985)
- 2.26 S. V. Bondarenko, E. V. Ivakin, A. S. Rubanov, V. I. Kabelka, A. V. Mikhailov: Opt. Commun. 61, 155-158 (1987)
- 2.27 G. L. Eesley, B. M. Clemens, C. A. Paddock: Appl. Phys. Lett. 50, 717-719 (1987)
- 2.28 D. Fournier, A. C. Boccara, N. M. Amer, R. Gerlach: Appl. Phys.

- Lett. 37, 519-521 (1980)
- 2.29 M. A. Olmstead, N. M. Amer, S. Kohn: Appl. Phys. A 32, 141-154 (1983)
- 2.30 For a review see for example J. P. Monchalin: In [2.10], pp 485-499
- 2.31 A C. Tam, C. K. N. Patel Opt. Lett. 5, 27-29 (198)
- 2.32 H. M. Frost: In *Physical Acoustics*, Vol. 14, ed. by W. P. Mason, R. N. Thurston (Academic, New York 1979) pp. 179-276
- 2.33 R. E. Lee, R. M. White: Appl. Phys. Lett. 12, 12-14 (1968)
- 2.34 A C. Tam, C. K. N. Patel Appl. Opt. 18, 3348-3358 (1979)
- 2.35 H. Coufal: J. Photoacoustics I, 417-428 (1984)
- 2.36 A. Mandelis : In [2.10], pp. 590-614
- 2.37 Y. Sugitani, A. Uejima, K. Kato: J. Photoacoustics 1, 217-236 (1982)
- 2.38 P. R. Griffiths, J. A. de Haseth: *Fourier Transform Infrared Spectrometry* (Wiley, New York 1986) •
- 2.39 H. Coufal: Appl. Opt. 21, 104-109 (1982)
- 2.40 J. M. Bennett: Thin Solid Films 123, 27-44 (1985)
- 2.41 K. Driss-Khodja, A. Gheorghiu, M. L. Theye: Opt. Commun. 55, 169-173 (1985)
- 2.42 T. Hata, T. Hatsuda, T. Komatsu: Jpn. J. Appl. Phys. 24, 1463-1466 (1985)
- 2.43 G. P. Ceasar, M. Abkowitz, J. W. P. Lin: Phys. Rev. B 29, 2353-2355 (1984)
- 2.44 N. M. Amer, A. Skumanich, W. B. Jackson: J. Non-Cryst. Solids

- 59-60, 409-412(1983)
- 2.45 R. Mostefaoui, J. Chevallier, S. Meichenin, F. Auzel: *J. Non-Cryst. Solids* 77-78, 307-310(1985)
- 2.46 D. Jousse, E. Bustarret, F. Boulitrop: *Solid State Commun.* 55, 435-438 (1985)
- 2.47 T. L. Chu, S. S. Chu, S. T. Ang, A. Duong, C. G. Hwang: *J. Appl. Phys.* 59, 3122-3125(1986)
- 2.48 M. Favre, H. Curtis, A. V. Shah: *J. Non-Cryst. Solids* 97-98, 731-734 (1987)
- 2.49 K. Pierz, B. Hilgenberger, H. Mell, G. Weiser: *J. Non-Cryst. Solids* 97-98, 63-66(1987)
- 2.50 R. C. Van Oort, M. J. Geerts, J. C. Van Den Heuvel: *J. Non-Cryst. Solids* 97-98, 1427-1430(1987)
- 2.51 S. Guha, J. S. Payson, S. C. Agarwal, S. R. Ovshinsky: *J. Non-Cryst. Solids* 97-98, 1455-1458(1987)
- 2.52 A. H. Mahan, R. C. Kerns, G. Devaud: *J. Electron. Mater.* 12, 1033-1049 (1983)
- 2.53 D. Jousse, J. C. Bruyere, E. Bustarret, A. Deneuveille: *Philos. Mag. Lett.* 55,41-46(1987)
- 2.54 J. S. Payson, R. C. Ross: *J. Non-Cryst. Solids* 77-78, 579-582 (1985)
- 2.55 M. L. Theye, A. Gheorghiu, K. Driss-Khodja, C. Boccara: *J. Non-Cryst. Solids* 77-78, 1293-1296(1985)
- 2.56 C. H. Seager, J. A. Knapp: *Appl. Phys. Lett.* 45, 1058-1059 (1984)
- 2.57 T. Hata, T. Hatsuda, T. Miyabo, S. Hasegawa: *Jpn. J. Appl. Phys.*

- Suppl. 25-1, 226-228(1986)
- 2.58 J. P. Roger, D. Fournier, A. C. Boccara: Thin Solid Films **128**, 11-20 (1985)
- 2.59 M. Fathalla, M. Ben Said, R. Bennaceur: Phys. Status Solidi A **99**, 521-526 (1987)
- 2.60 F. Coriand, H. G. Walther, E. Welsch: Thin Solid Films **130**, 29-35 (1985)
- 2.61 O. Gode, W. Heimbrodt, F. Sittel: Phys. Status Solidi A **93**, 277-282(1986)
- 2.62 E. Welsch, H. G. Walter, H. J. Kuhn: J. de Phys. **48**, 419-424 (1987)
- 2.63 B. R. Weinberger, C. B. Roxlo, S. Etemad, G. L. Baker, J. Orenstein: Phys. Rev. Lett. **52**, 86-89 (1984)
- 2.64 M. D. Porter, D. H. Karweik, T. Kuwana, W. B. Theis, G. B. Norris, T. O. Tiernan: Appl. Spectrosc. **38**, 11-16 (1984)
- 2.65 W. Knoll, H. Coufal: Appl. Phys. Lett. **51**, 892-894 (1987)
- 2.66 J. K. Dohrmann, U. Sander: Ber. Bunsenges. Phys. Chem. **90**, 605-609(1987)
- 2.67 P. Helander, I. Lundstrom: J. Appl. Phys. **52**, 1146-1151 (1981)
- 2.68 J. Pelzl, R. Grygier, H. Coufal: In *Progress in Basic Principles of Imaging Systems*, ed. by F. Grazer, E. Moisar (Vieweg, Braunschweig 1986) p. 695
- 2.69 H. Coufal: Appl. Phys. Lett. **45**, 516-518 (1984)
- 2.70 C. Starr: Rev. Sci. Instrum. **8**, 61-64 (1937)
- 2.71 M. J. Adams, G. F. Kirkbright: Analyst **102**, 678-682 (1977)

- 2.72 H. Coufal, P. Hefferle: *Appl. Phys. A* 38, 213-219 (1985)
- 2.73 P. K. John, L. C. M. Miranda, A. C. Rastogi: *Phys. Rev. B* 34, 4342-43(1986)
- 2.74 C. C. Ghinzoni, L. C. M. Miranda: *Phys. Rev. B* 32, 8392-8394 (1985)
- 2.75 O. Pessoa, Jr., C. L. Cesar, N. A. Patel, H. Vargas, C. C. Ghinzoni, L. C. M. Miranda: *J. Appl. Phys.* 59, 1316-1318(1986)
- 2.76 W. P. Leung, A. C. Tam: *Opt. Lett.* 9, 93-95 (1984)
- 2.77 R. E. Imhof, F. R. Thornley, J. R. Gilchrist, D. J. S. Birch : *J. Phys. D* 19 1829-1841(1986)
- 2.78 A. Skumanich, H. Dersch, M. Fathalla, N. M. Amer: *Appl. Phys. A* 43, 297-300 (1987)
- 2.79 J. P. Roger, F. Lepoutre, D.Fournier, A. C. Boccara: *Thin Solid Films* 155, 165-174 (1987)
- 2.80 G. Benedetto, R. Spagnolo: *Appl. Phys. A* 46, 169-172 (1988)
- 2.81 T. Hashimoto, J. Cao, A. Takaku: *Thermochim. Acta*, 120, 191-201 (1987)
- 2.82 A. Mandelis, E. Siu, S. Ho: *Appl. Phys. A* 33, 153-159 (1984)
- 2.83 M. E. Abu-Zeid, A. E. Rakhshani, A. A. Al-Jassar, Y. A. Youssef: *Phys.Status Solidi A* 93, 613-620 (1986)
- 2.84 P. Florian, J. Pelzl, M. Rosenberg, H. Vargas, R. Wernhardt: *Phys.Status Solidi A* 48, K35-K38 (1978)
- 2.85 C. Pichon, M. Le Liboux, D. Fournier, A. C. Boccara: *Appl. Phys. Lett.* 35,435-436(1979)
- 2.86 M. A. A. Siqueira, G. G. Ghinzoni, J. I. Vargas, E. A. Menez, H.

- Vargas, L. C. M. Miranda: *J. Appl. Phys.* **51**, 1403-1406(1980)
- 2.87 P. S. Bechthold, M. Campagna, T. Schober: *Solid State Commun.* **36**, 225-231 (1980)
- 2.88 Korpiun, J. Baumann, E. Luscher, E. Papamokos, R. Tilgner: *Phys. Status Solidi A* **58**, K13-K16 (1980)
- 2.89 A. Mandelis, F. Care, K. K. Chan, L. C. M. Miranda: *Appl. Phys. A* **38**, 117-122(1985)
- 2.90 A. L. Glazov, S. B. Gurevich, N. N. Hyashenko, N. P. Kalmykova, K. L. Muratkov, N. A. Rogachev: *Sov. Tech. Phys. Lett. (USA)* **11**, 59-60(1986)
- 2.91 H. Coufal, W. Lee: *Appl. Phys. B* **44**, 141-146 (1987)
- 2.92 A. B. Scruby, R. J. Dewhurst, A. A. Hutchins, S. B. Palmer: In *Research Techniques in Nondestructive Testing*, Vol. 5, ed. by R. S. Sharpe (Academic, New York 1982) pp. 281-327
- 2.93 G. Birnbaum, G. S. White: In *Research Techniques in Nondestructive Testing*, Vol. 7, ed. by R. S. Sharpe (Academic, New York 1984) pp. 259-365
- 2.94 A A Hutchins: *Physical Acoustics*, Vol. 18, ed. by W, P. Mason, R. N. Thurston (Academic, New York 1986)
- 2.95 C. Tam, H. Coufal: *Appl. Phys. Lett.* **42**, 33-35 (1983)
- 2.96 G. M. Sessler, J. E. West, G. Gerhard: *Phys. Rev. Lett.* **48**, 563-566 (1982)
- 2.97 H. Sontag, A. C. Tam: *Appl. Phys. Lett.* **46**, 725-727 (1985)
- 2.98 H. Sontag, A. C. Tam: *Can. J. Phys.* **64**, 1330-1333 (1986)
- 2.99 G. L. Eesley, B. M. Clemens, C. A. Paddock: *Appl. Phys.*

- Lett. 50,717-719(1987)
- 2.100 C. Thomson, H. J. Maris, J. Tauc: Thin Solid Films 154, 217-223 (1987)
- 2.101 A. Rosenwaig: J. Photoacoust. 1, 371-386(1983)
- 2.102 R. C. Frye, J. J. Kumler, C. C. Wong: Appl. Phys. Lett. 50, 101-103(1987) H. G. Walther, E. Welsch: Thin Solid Films 142, 27-3.5 (1986)
- 2.103 S. Aithal, G. Rousset, L. Bertrand: Thin Solid Films 119, 153-158 (1984)
- 2.104 H. Coufal, R. Grygier, D. Horne, J. Fromm: J. Vac. Sci. Technol A 5, 2875-2889(1987)
- 2.105 G. Li, Q. R. Yin, W.G. Luo, Z.W. Yin: Jpn.J. Appl. Phys. Suppl. 24, 425-426(1985)
- 2.106 G. M. Sessler, R. Gerhard-Multhaupt: Radiat. Phys. Chem. 23, 363-370 (1984)
- 2.107 H. Coufal, U. Moller, S. Schneider: Appl. Opt. 21, 116-119(1982)
- 2.108 H. Coufal, U. Moller, S. Schneider: Appl. Opt. 21, 2339-2343 (1982)
- 2.109 J. C. Murphy, J. W. Maclachlan, L. C. Aamodt: In [5.10], pp. 529-541
- 2.110 L. D. Favro, P. K. Kuo, R. L. Thomas: In [2.4], pp. 69-96
- 2.111 W. C. Mundy, R. S. Hughes: Appl. Phys. Lett. 43, 985-987 (1983)
- 2.112 M. Guardalben, A. Schmid: Phys. Rev. 35, 4026-4030 (1987)
- 2.113 J. I. Burov, D. V. Ivanov: J. de Phys. 47, 549-552 (1986)

- 2.114 A. Rosencwaig, J. Opsal: In [2.10], pp. 516-528
- 2.115 A. Rosencwaig: In [2.4], pp. 97-135
- 2.116 H. Taalat, H. D. Dardy: In *1983x Ultrasonics Symposium Proceedings*, ed. by B. R. McAvoy (IEEE, New York 1983) pp. 700-703
- 2.117 B. Rothenhausler, J. Rabe, P. Korpiun, W. Knoll: *Surf. Sci.* 137, 373-383 (1984)
- 2.118 T. Inagaki, M. Motosuga, E. T. Arakawa, J. P. Goudonnet: *Phys. Rev. B* 32, 6238-6245 (1985)
- 2.119 T. Inagaki, M. Motosuga, E. T. Arakawa, J. P. Goudonnet: *Phys. Rev. B* 31, 2548-2550 (1985)
- 2.120 C. S. Jung, G. Park, Y. D. Kim: *Appl. Phys. Lett.* 47, 1165-1167 (1985)
- 2.121 R. K. Grygier, W. Knoll, H. Coufal: *Can. J. Phys.* 64, 1067-1069 (1986)
- 2.122 T. Inagaki, J. P. Goudonnet, P. Royer, E. T. Arakawa: *Appl. Opt.* 25, 3635-3639 (1986)
- 2.123 V. N. Rai: *Appl. Opt.* 26, 2395-2400
- 2.124 P. Royer, J. P. Goudonnet, T. Inagaki, G. Chabrier, E. T. Arakawa: *Phys. Status Solidi A* 105, 617-625 (1988)
- 2.125 C. L. Cesar, H. Vargas, H. Pelzl: *J. Appl. Phys.* 55, 3460-3464 (1984)
- 2.126 Netzelmann, U. Krebs, J. Pelzl: *Appl. Phys. Lett.* 44, 1161-1162 (1984)
- 2.127 M. Davies: *J. Phys. D* 18, 1655-1663 (1985)

- 2.143 S. E. Braslavsky and K. N. Houk. *Pure Appl. Chem.* 60, 1055 (1988).
- 2.144 J. W. Verhoeven. *Pure Appl. Chem.* 68, 2223 (1996).
- 2.145 IUPAC. *Quantities, Units and Symbols in Physical Chemistry* (the 'Green Book'), prepared for publication by I. Mills, T. Cvitaš, K. Homann, N. Kallay, K. Kuchitsu, Blackwell Scientific, Oxford (1988).

Chapter 3

Photothermal Spectrometer: design and use

A compact setup which integrates sample displacement stage, as well as the probe laser and optics has been described by Charbonnier and enjoys celebrity status as a basic setup upon which a large majority of mirage experiments are founded. A commercial version exists, as well as numerous "standard" variants for different applications. The block is shown here.

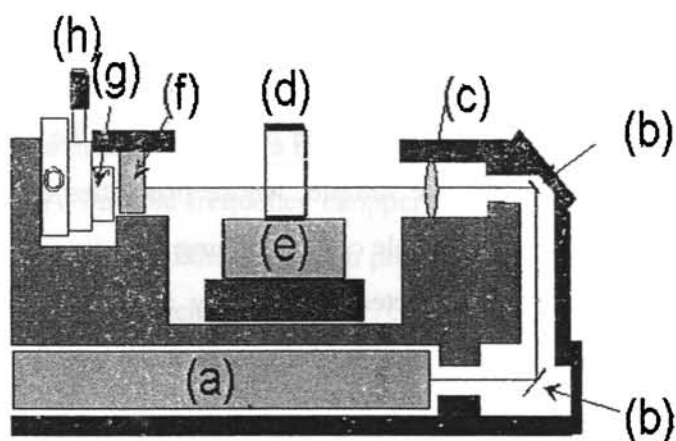
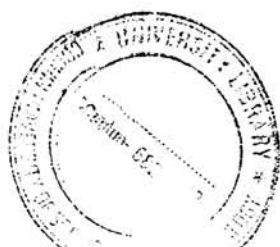


Figure 3.1

The base of the block serves as housing for the HeNe or diode probe laser (a). The beam is directed by aluminum mirrors (b), then passes through a glass lens (c) which focuses the beam at the center of the sample (d), which is positioned by the sample holder and stage (e). The beam then passes through an



interference (optical notch) filter (f) which rejects stray reflections and is directed onto a photodiode position sensor (g), also positioned on an x-y stage. The mirage signal is detected by the position sensor (photodiode pair), associated to a Lock-in amplifier.

This set up houses only the probe and detector assembly and does not include pump beam, modulator and its accessories.

We have designed a compact set up which takes care of the above. The main components of our transverse PBD set up are

- Pump beam which produces the RIG in the sample
- Mechanical chopper which modulate the pump beam
- A probe laser beam to detect the RIG
- The sample, whose properties are to be studied and a sample cell containing CCl_4
- A detector assembly and the associated electronics to measure the deflection of the signal
- All of the above mounted on a vibration isolation table

In addition this set up can operate in manual as well as automated mode. All the micrometer movements can be motor driven under the control of a computer program.

The finer details of the main components of the transverse PBD set up are given below.

3.1.1 THE PUMP SOURCE

The excitation source should be a light source with sufficient power density to produce the RIG. We can use a cw laser, a pulsed dye laser or a tungsten arc lamp with a monochromator. When a cw laser or an arc lamp is used, a mechanical chopper modulates the output. The chopped light beam must be focused upon the sample. Usually a laser is used as the pump beam so as to permit tight focusing.

In our experiments we used an Nd-YAG laser of wavelength 5320 \AA with an output power of 25mW and a He-Ne laser of wavelength 6328 \AA with an output power of 10mW.

3.1.2 THE MECHANICAL CHOPPER

The pump beam is modulated with a mechanical chopper so as to detect the photothermal effect. A variable frequency chopper is used for the purpose. When the pump beam is modulated the deflection produced on the probe beam is also modulated at the same frequency.

The optimum range of the chopper frequencies is governed by the characteristic time of the sample. An observable signal is obtained for samples even at high frequencies like 250 Hz.

A mechanical chopper which can be used in the range 0-4 K Hz is used as the modulator in this case.

3.1.3 THE PROBE BEAM SOURCE

A weak source must be used as the probe beam because it should not cause any heating in the sample.

In the present case a He-Ne laser of power 1mW is used as the probe beam. The probe beam is arranged so that it just grazes through the sample surface, perpendicular to the pump beam axis. Using a convex lens such that its focal spot is at the point where the pump beam is incident on the sample, the signal amplitude can be considerably increased. The focal length of the lens was 10 cm. Using this lens the pump beam diameter was reduced to .34mm from 1mm.

3.1.4 THE SAMPLE CELL

The sample cell is such that the sample can be placed easily inside it and the cell can be rotated for correct alignment. The selection of the coupling medium for the sample is to be done with care. The coupling medium should not react with the samples and the temperature coefficient of refractive index should be large. Since the temperature coefficient of refractive index (dn/dT) for liquids is of the order of $10^{-4} / ^\circ\text{C}$,³ which is of two orders greater than that for air, it is advantageous to use liquids as coupling fluid.

Carbon tetrachloride satisfies the conditions needed for the coupling fluid. It is almost transparent in the whole of visible region and it has

$$\frac{dn}{dT} = 5 \times 10^{-4} / K$$

The sample must be placed in a closed cell, which is usually made of materials like quartz, so that the probe beam after passing through the cell is not absorbed or scattered by the cell wall. By placing the sample in the cell the noise due to room vibrations can be reduced to a considerable extend. The sample can be easily introduced into the cell containing CCl_4 . The cell is

placed at an exact position so that the pump and the probe beams fall at the correct position.



Figure 3.2

3.1.5 THE DETECTOR ASSEMBLY AND SIGNAL MEASUREMENT

The probe beam passing through the region of varying index of refraction gets deflected and is detected using a position sensor. We use a bicell detector (EG&G, UV-140, BQ-2) for the purpose. There are two photodiodes, which acts as the position sensors. The position sensors convert deflection into a varying output voltage depending upon the deflection of the beam.

The best method to recover the signal is to use a lock in amplifier, which will help us to recover even feeble signals. The output of the sensor is fed into a lock-in amplifier⁵ which extracts the signal. The lock-in amplifiers locks the center frequency of the narrow band amplifiers to the modulation frequency allowing increased narrow banding without the instability normally associated with tuned amplifiers. The output of the lock-in amplifier (SR830DSP) can be recorded on a strip-chart or x-y recorder.

3.1.6 VIBRATION ISOLATION TABLE

All the above optical components are placed on an optical breadboard placed on a vibration free table. The alignment is made carefully and the detection is done.

When Does an Optical System Require a Table or Breadboard?

A table is desirable for breadboarding an optical system, test or experiment if any one or more of the following conditions exists or is required.

1. More than one optical path in the setup
2. Optical path runs in more than one horizontal direction
3. Vibration isolation is desired
4. Components are numerous or are relatively massive

Typical examples of applications where one should use optical tables are listed below.

1. Multiple-path interferometers—Mach-Zehnder, Twyman Green, Michelson. Stability of the mirror separation is critical to a fraction of a micron. **Vibration isolation** is also desirable.
2. Holography. Long-term vibration isolation is required. Rigidity and maintenance of specific separation between components also are required..

Tables for this use usually contain small **inner tubes** that provide both **support and vibration isolation**.

3. Research laser systems. The laser mirrors require rigid mounts to ensure stable output. Associated devices such as Q-switches, frequency doubling crystals, amplifiers, and optical power meters require a stable mounting surface. For convenience, components often are mounted at angles to the original laser beam path.



Figure 3.3. Example of a high-quality optical table. This table has pneumatic isolation legs, a lower accessory shelf (for mounting a laser) and beam-steering mirrors.

Vibration isolation: Vibrations induced into the surfaces can cause slight but significant movement in the table, and consequently the optical components. Vibrations can be induced in the table from the floor through the support structure by mechanical vibrations or through the air by acoustic disturbances.

Vibrations are *vertical vibrations* (where table ends flex up and down) and *horizontal vibrations* (where the table moves laterally). Generally, the vibrations of concern are relatively low-frequency (less than 100 hertz). In

addition, the tabletop itself can vibrate in a number of torsional and bending modes. Several of the lower order modes are shown in Figure.

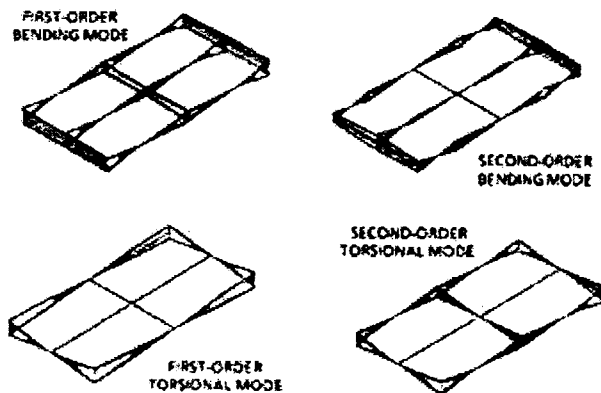


Figure 3.4 Low-order bending and torsional modes of a uniform rectangular plate.

Vibrations that result from motion of the laboratory floor usually occur in approximately the 5-Hz to 30-Hz range. Modern isolation optical table systems usually are suspended on pneumatic legs that are designed to resonate mechanically at about 1 Hz when loaded with a tabletop. The mechanical resonance is far lower in frequency than typical floor vibrations. So, little energy is transferred from the floor to the table surface.

The pneumatic isolation support system combined with the metal honeycomb damping materials make modern optical tables an excellent surface on which to conduct vibration-sensitive experiments. For these reasons—in addition to convenience and cost—steel honeycomb table systems with pneumatic

supports have replaced solid metal or granite tabletops in most electro-optical laboratories.

In many applications, excellent vibration isolation isn't needed, but the convenience of a mounting surface and predrilled holes is desired. In such cases, optical "breadboards" often are used as a lower-cost alternative to honeycomb isolation tables. Figure shows one example of an optical breadboard.

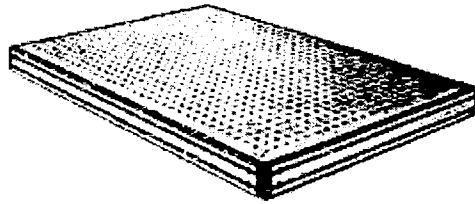


Figure 3.5 A modern optical breadboard

Like honeycomb isolation tables, these breadboards come in a variety of stock and custom sizes and hole patterns. Typical hole patterns are 1/4-20 holes on 1-in centers. But, metric holes (usually M6 on 25-mm centers) are also available. The breadboard shown in Figure permits equipment to be "hung off" the side using bolts and captive nuts.

If you need some degree of vibration isolation, you can suspend breadboards on firm tabletops with small-diameter inner tubes or sheets of foam rubber. In some cases, these "budget" isolation surfaces make sense as a significantly lower-cost alternative to pneumatic isolation tables.

As discussed earlier, optical tables are susceptible to *induced vertical and horizontal vibrations*. These vibrations are undesirable in applications that involve very precise optical alignment systems because they result in *relative movement between the optical components mounted to the table*.

One can understand *vertical vibrations* within the table surface by visualizing a *very small, periodic bending motion*, or flexing, in the table—similar to a diving board. These vibrations originate *as floor or building resonant vibrations*. *They're induced through the table supports*. The *frequencies of these vibrations typically range from 5 to 30 Hz*.

We can isolate some vibration in a rigid-frame table support by placing *rubber pads* between the table legs and the floor and between the support and the table surface. You'll get much more effective isolation by using *air pistons* in the table legs. (See Figure) These pistons actually "float" the tabletop and provide isolation from vertical floor vibrations. Vibration-isolation systems are similar to a high-frequency cutoff filter, insofar as they pass low-frequency vibrations and isolate all frequencies above some design value. *Air pistons provide vertical isolation for frequencies above 5-10 Hz*, and generally require a source of compressed air in the laboratory.

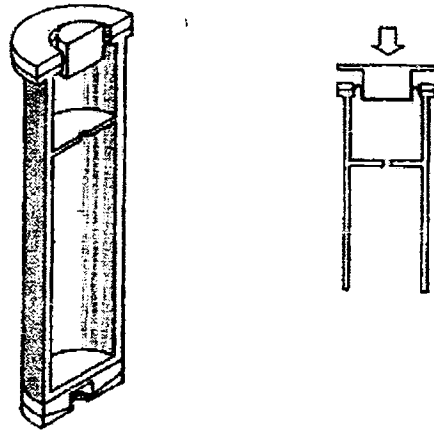


Figure 3.6 Air piston for optical table vibration isolation

Typical determination of the response of a table in each of the three axis directions to an induced vibration is using accelerometer, cable and scope as shown in Figure . The accelerometer should be in the vertical position (circular end facing up), and directly over the approximate center of the tabletop. This will now indicate vibration in the vertical axis.

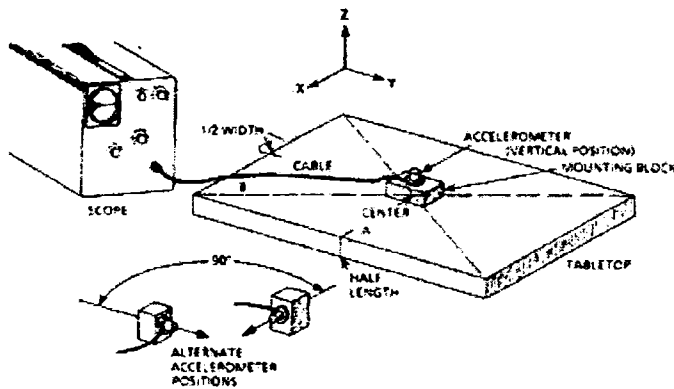


Figure 3.7

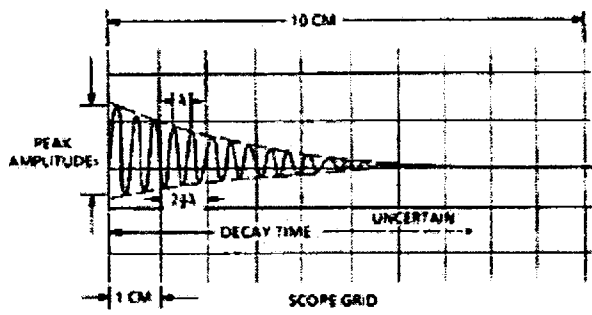


Figure 3.8 Analysis of vibration data

The attempts by other groups in building low cost vibration isolation are outlined below. The table consists of three components; a small piece of carpet, a small 12-18 inch diameter inner tube, and a metal plate, see figure 3.9. The carpet should be

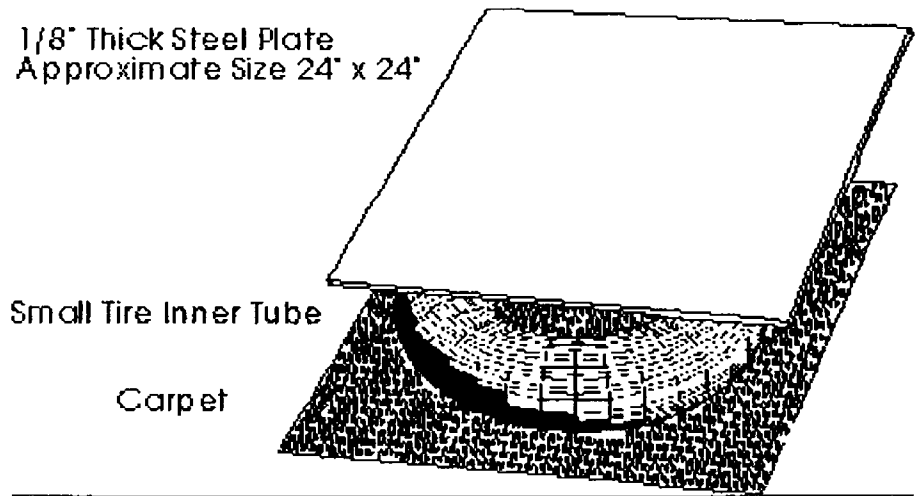


Figure 3.9

large enough so that the inner tube can lay on it without hanging over the edge. The inner tube has just enough air for it to be filled but still remain very soft. In other words you could squeeze the sides of it together easily. The top metal plate is the working area and should be about the same size as the carpet. The metal should be thick enough so that it doesn't flex when components are placed on it. The plate used is 3/16" thick. If you cannot get a metal plate you can substitute 3/4" or thicker plywood, with a thin sheet of metal adhered to the top (working) side.

In another design the interferometer, specimen mount, associated measuring and positioning equipment, pulser, and other components were installed on a heavy, magnetic tabletop originally used for holographic demonstrations. The tabletop in turn was supported by four **air-filled** inner tubes, which damped out vibrations as low as about 5 Hz. The resulting **anti-vibration table** in turn was set on a heavy lab bench top supported by four **water-filled** inner tubes to further damp building vibrations. This homemade arrangement was inexpensive and very effective in suppressing building vibrations.

W. C. Bigelow et al at University of Michigan had reasonably good success isolating a SEM from building traffic vibrations by setting it on a platform that was supported by four inflated inner tubes from garden tractor tires. One could probably work out a similar scheme for a light microscope for very little cost and effort, using inflatable cushions or smaller inner tubes.

The table shown below, suspended on the inner tube, is an air flotation system that will settle out vibrations rapidly and can be used successfully in isolating

an object and optical components from vibration up to half the wavelength of 6328Å light.

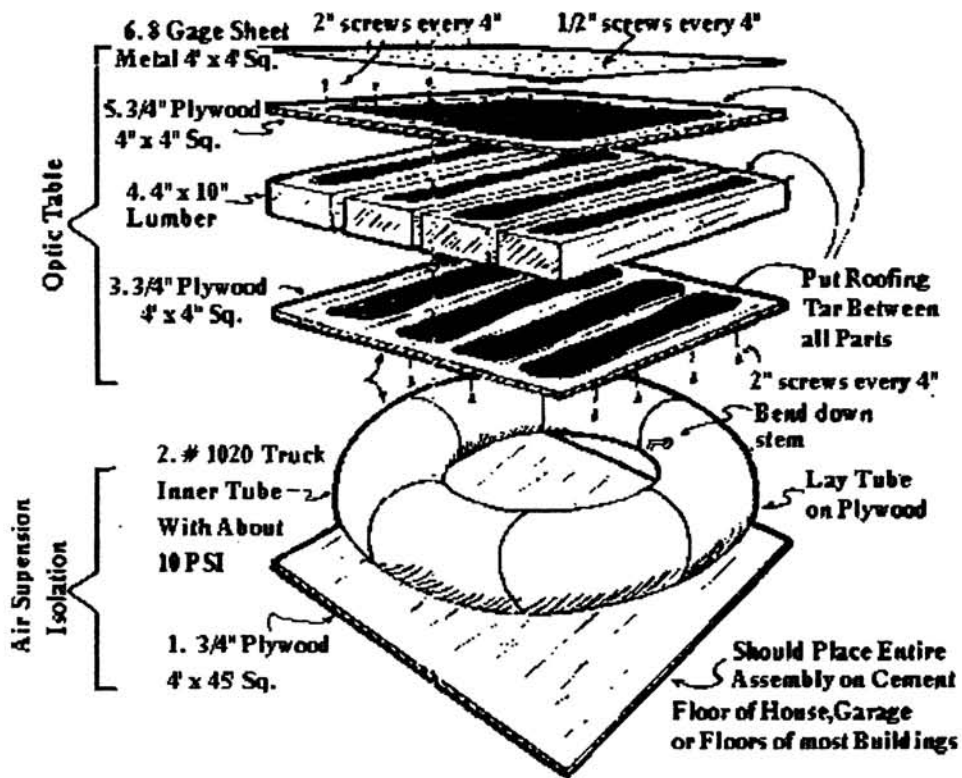


Figure 3.10

Taking all this into stock we designed the table with spring, shock absorber combination and air filled rubber tube. The photograph of the home made vibration isolation table is shown.

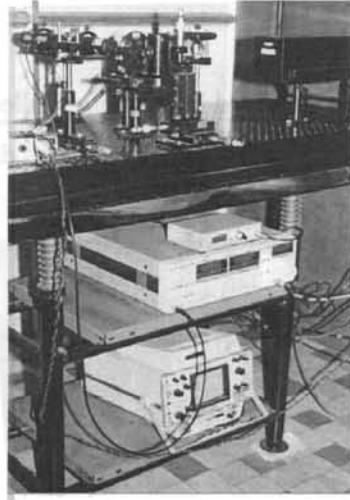


Figure 3.11

The table support was built with 1" MS pipes as shown. The table top was initially isolated from floor pick-up using the spring-damper combination on all four legs which supports a MS steel top weighing 40 kg.

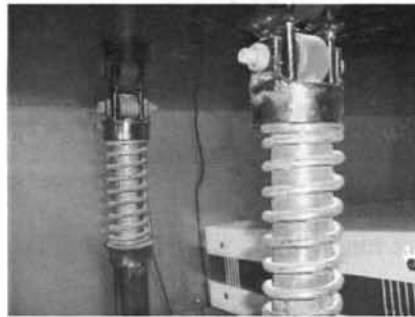


Figure 3.12

The next level of isolation is provided by three air filled inner tubes which supports a similar MS top of same dimension but double the thickness weighing 80 kg.

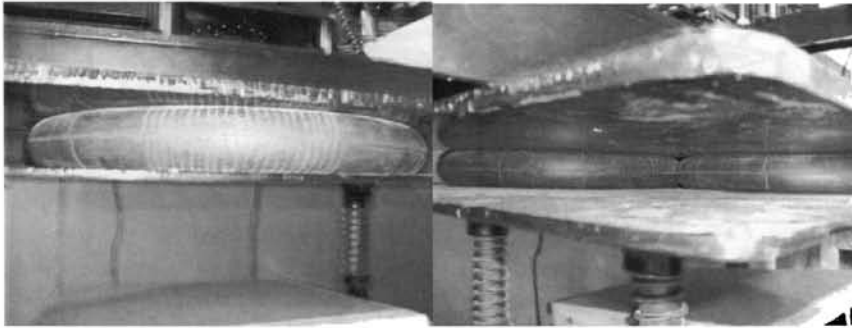


Figure 3.13

An optical bread board supports our compact photothermal spectrometer.

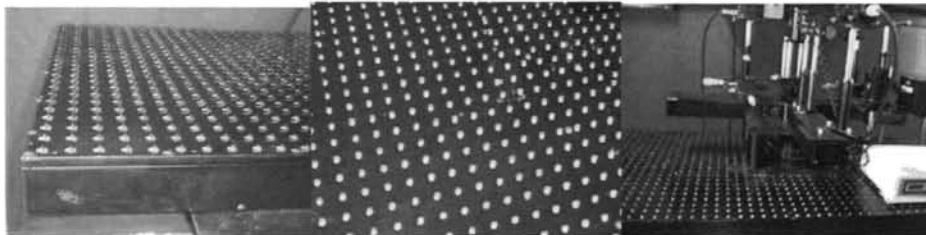


Figure 3.14

The table was studied for isolation against normal sources of vibration in the lab. The results are also shown.

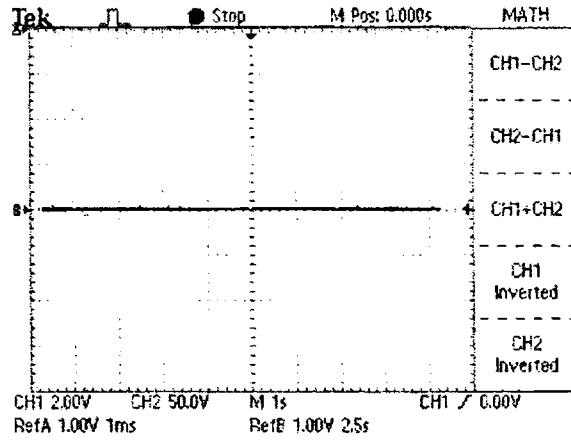


Figure 3.15 Air conditioner switched off

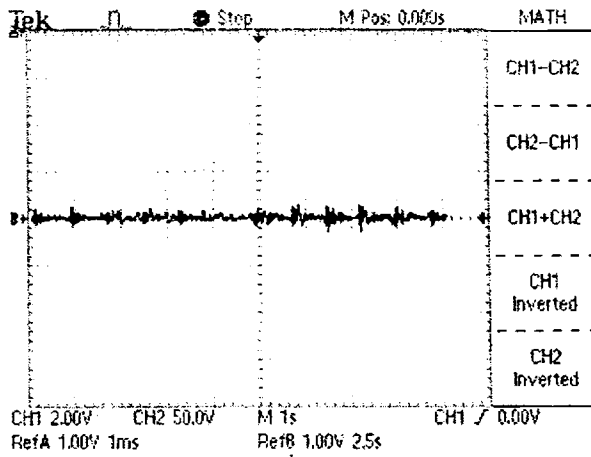


Figure 3.16 Air conditioner switched on

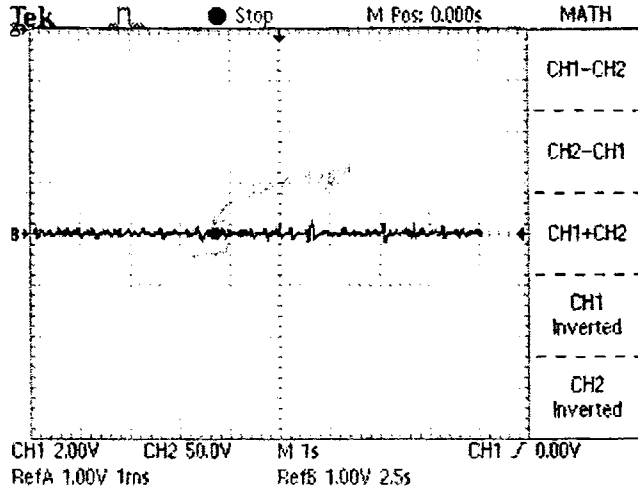


Figure 3.17 Instance of a chair dragged on the floor of the lab

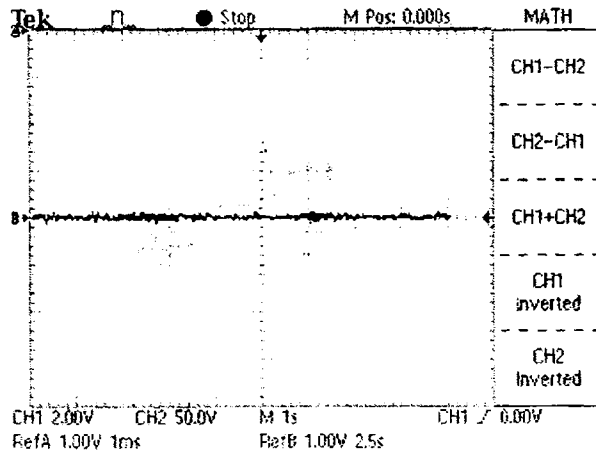


Figure 3.18 Instance of outer door opening , a person peeping through inner door and outer door closing

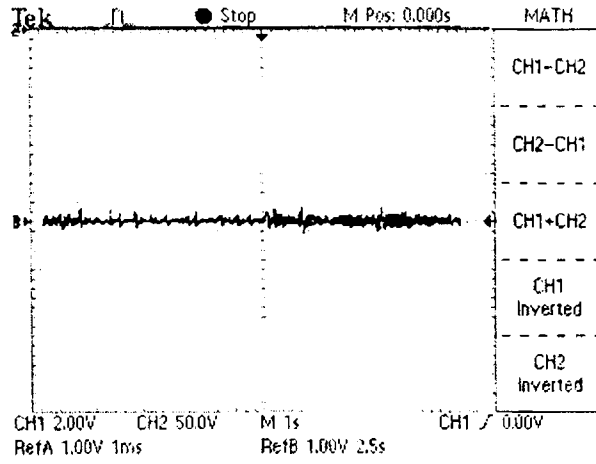


Figure 3.19 NCC brisk march in the corridor

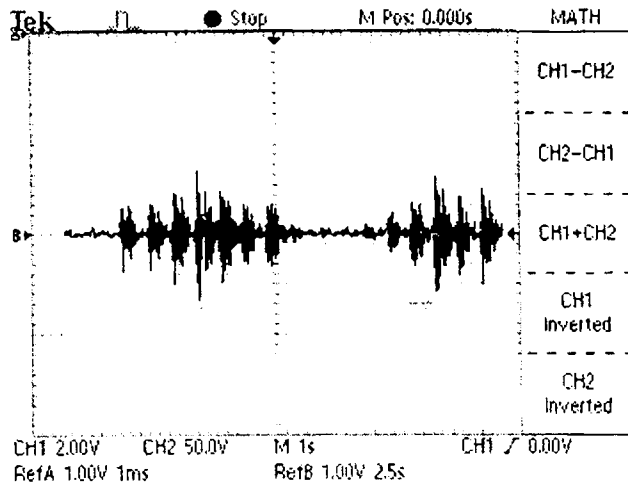


Figure 3.20 A person approaching the table, walking past the table, stopping and receding

3.2 RESULTS AND DISCUSSIONS

The samples analysed were

- CuInSe₂ samples prepared using Chemical Bath Deposition Technique
- In₂S₃ prepared using Chemical Spray Pyrolysis Technique
- CuInS₂ samples prepared using Chemical Spray Pyrolysis Technique
- CII Rubber with EPDM
- Poly Urethane with various fillers
- He⁺ implanted CdS

3.2.1 CuInSe₂

Copper Indium di Selenide is a ternary chalcopyrite compound with an ideal PV bandgap of 1eV. Solar cells made of them have reported efficiencies greater than 17%. CBD is a simple technique for the deposition of large area solar cells. These CuInSe₂ samples were prepared using Chemical Bath deposition techniques. The samples were prepared at room temperature at a pH value of 6.5 with citrate as the complexing agent for Copper and Indium and sodium selenosulphite. By varying the Indium ratio from 7.5 ml to 10ml, 15 ml, 20 ml, 25 ml and 30 ml samples labeled CIS 1 – CIS 7 were obtained. The volume of

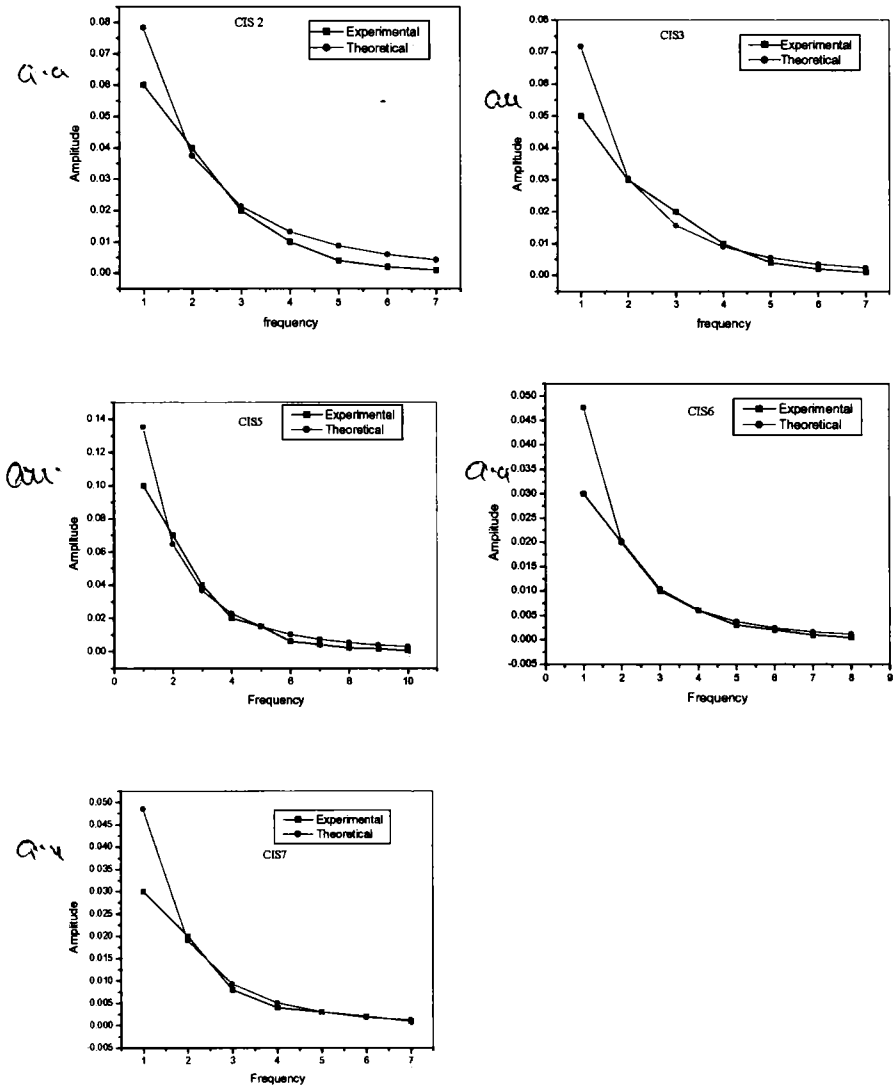


Fig 3.21 PTD amplitude vs frequency of various CIS samples copper citrate and sodium selenosulphite was kept constant at 7.5 ml and 20 ml respectively.

Uzup

The thermal diffusivity variation from sample to sample was calculated from the theoretical fit as tabulated below

Sample	Thermal diffusivity $\times 10^8$ <i>variation in a.u.</i>
CIS 2	1.35
CIS 3	1.528
CIS 5	1.68
CIS 6	2.2
CIS 7	2.4

3.2.2 In₂S₃ thin films

In₂S₃ is one of the numerous compounds in the In-S phase system [3.1]. Three well defined modifications of In₂S₃ have been reported in the literature. The cubic α -form [3.2] is stable above 693 K and crystallizes in the defect spinel structure ($a = 10.77 \text{ \AA}$). The stable room temperature phase is β -In₂S₃ [3.3]. A third modification (γ -In₂S₃) with trigonal symmetry has been reported above 1047 K [3.4].

It belongs to the III-VI compounds, is a wide band gap semiconductor with high photoconductive and luminescent properties. Thus the material finds its application as buffer layer in solar cells. Eventhough CdS is very efficient in achieving promising cells, it is undesirable from the point of view of environmental safety. Moreover a wider band gap material than CdS can reduce optical absorption losses at short wavelengths.

The physical properties and structure of indium sulfide [Fig. 3.22] thin films are given below. Indium atoms are in red colour and sulfur in blue colour.

Structure	: Tetragonal
Colour	: Yellow
Appearance	: Crystalline solid
Melting Point	: 1050°C
Density	: 4450 kg/m ³
Lattice Parameters	: a = b = 7.619 Å and c = 32.329 Å

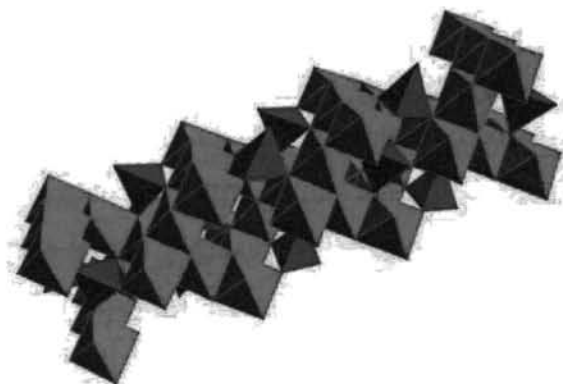


Fig. 3.22 structure of indium sulfide

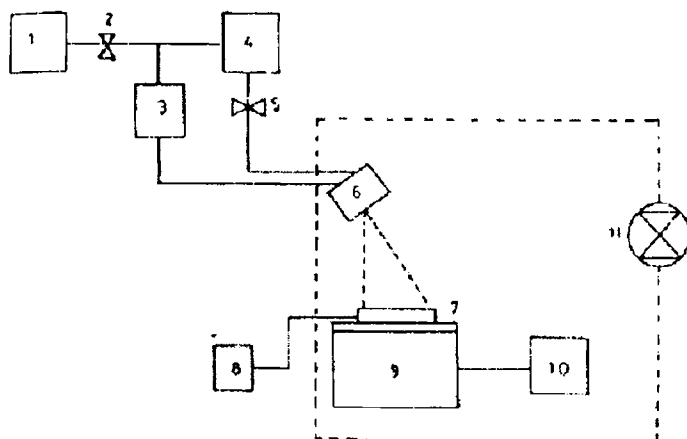
The crystal structure of indium sulfide has been studied by Hahn et al [3.2] who ascribed to it the cubic structure of a disordered cation deficient spinel. C. J. X Rooymans [3.3] found that some “extra lines” in the X-Ray diagram were conclusive evidence indicating that In_2S_3 was in fact tetragonal. The tetragonal unit cell is formed by the superposition of three spinel blocks, a four-fold screw axis appears as the result of indium vacancy ordering.

Chemical Spray Pyrolysis is a simple and low cost method for the fabrication of In_2S_3 thin films. In the present case photoconductive β -Indium sulfide thin films were prepared using Chemical Spray Pyrolysis (CSP) technique at different substrate temperatures and various indium to sulfur ratios. The knowledge of variation of photosensitivity of this material with deposition, structural or stoichiometric parameters are very much essential for photovoltaic device application. It is to be specifically noted that in CSP technique, it is comparatively easy to make variation in stoichiometry of the sample. A detailed study on the structural, compositional, optical and electrical properties was done on these films.

Experimental Details

Experimental set-up for the deposition is schematically shown in Fig. 3.23 Cleaned glass slides were placed on a thick iron block ($15 \times 9 \times 1 \text{ cm}^3$), which can be heated to the required temperature with a controlled heater. Temperature of substrate holder was measured using a digital thermometer (Thermis, series 4000) and temperature control was achieved using a variable transformer. Sprat head and heater with substrate are kept inside a chamber provided with a n exhaust fan for removing gaseous by- products and vapour of the solvent (here water). During spray, temperature of substrate was kept constant with an accuracy of $\pm 5^\circ\text{C}$. Pressure of carrier gas was noted using a manometer and was kept at $90 \pm 0.5 \text{ cm of Hg}$. Spray rate was 20 ml/min. , and distance between spray head and substrate was $\sim 15 \text{ cm}$. In order to get uniform composition and thickness, spray head was moved to either side manually with uniform speed.

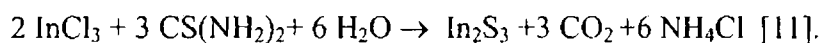
In_2S_3 thin films were deposited over glass substrates ($37 \times 12 \times 1.4 \text{ mm}^3$) from aqueous solutions of indium chloride (InCl_3) and thio-urea ($\text{CS}(\text{NH}_2)_2$) using compressed air as carrier gas. Thiourea was chosen as the source of sulfur ions in spray solution because it avoids precipitation of metallic sulfides and hydroxides since it forms complexes with indium ions easily [3.5]. Aqueous solutions of these salts were prepared in distilled water. Indium to sulfur ratio in the solution was varied by varying the molar concentration of InCl_3 and $\text{CS}(\text{NH}_2)_2$. Total volume of the solution sprayed was 400 ml in all cases. Samples were prepared at different substrate temperatures in the range 150°C to 380°C with an accuracy of $\pm 5^\circ\text{C}$ keeping In/S ratio at 2/3. Then the molar concentration of sulfur in the solution was varied by keeping the indium concentration at 2 so that In/S ratio varied from 2/1 to 2/8. For this, molarity of indium chloride was kept at 0.025 M and that of thiourea was varied. Later keeping the sulfur concentration at 3, 6 and 8, concentration of indium was varied from 1.2 to 2.5 with the aim of studying the variation in photoresponse of the sample. In all these cases substrate temperature was kept at 300°C .



- | | |
|--------------------------------|---------------------------|
| 1. Air compressor | 2. Gas flow control valve |
| 3. Manometer | 4. Solution reservoir |
| 5. Solution flow control valve | 6. Spray head |
| 7. Substrate | 8. Thermometer |
| 9. Substrate heater | 10. Heater control |
| 11. Exhaust fan | |

Fig. 3.23 Experimental set-up for spray pyrolysis system

Formation of In_2S_3 results from the chemical reaction:



Samples having various thicknesses were also prepared by varying the total volume of the solution sprayed as 400 ml, 600 ml, 800 ml and 1000 ml.

Thickness of the films prepared at 300°C was found to be $1 \mu\text{m}$ from Stylus measurement

Variation of Thickness

Thickness of the indium sulfide thin films was varied by varying the total volume of the solution sprayed. Volume of the solution was varied as 400 ml, 600 ml, 800 ml and 1000 ml. For this the molarity of InCl_3 solution was kept at

0.025 M and that of thiourea was kept at 0.0375 M so that the In/S ratio becomes 2/3.

Thicknesses of the samples were measured using stylus method.

Volume of the solution (ml)	Thickness (μm)	
400	1	
600	2.05	
800	2.11	2.42 from PTD
1000	4.1	

Transmission spectra were taken in the wavelength range 450-2500 nm. The percentage of transmittance decreased from $\sim 80\%$ to $\sim 40\%$ on increasing the thickness of the films. The variation in transmittance for different volume of the solution sprayed is shown in Fig.3.24.

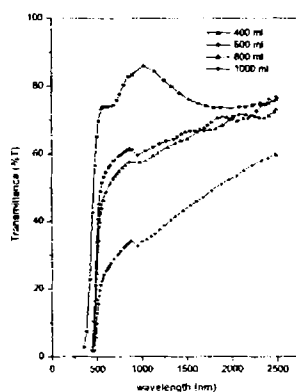


Fig. 3.24 Variation in transmittance for various volumes of the solution sprayed

In₂S₃ samples of different thickness were analysed using both He-Ne laser and Nd-YAG laser. The thermal diffusivity of the sample was found out. The samples sprayed with 400ml solution was known to have a thickness of one micron. Experiments were performed using Nd-YAG laser on four samples sprayed with 400ml, 600ml, 800ml and 1000ml of the solution. The deflection amplitude showed clear variation with thickness and using this technique it could be inferred that the thickness increased with the amount of the solution sprayed.

DETERMINATION OF THERMAL DIFFUSIVITY

The sample was scanned along the pump beam profile and the phase was recorded from the lock-in amplifier. The plot of phase versus normal offset was made (Fig 3.25a and b). The slope of the graph was found whose reciprocal gives the characteristic length. This will be equal to the thermal diffusion length for high diffusivity samples.

$$\frac{1}{\text{slope}} = \sqrt{\frac{D}{\pi f}}$$

The *diffusivity* of the In₂S₃ was found out to be $0.196 \text{ cm}^2 \text{ s}^{-1}$. This is equal to the thermal diffusivity value found in literature.

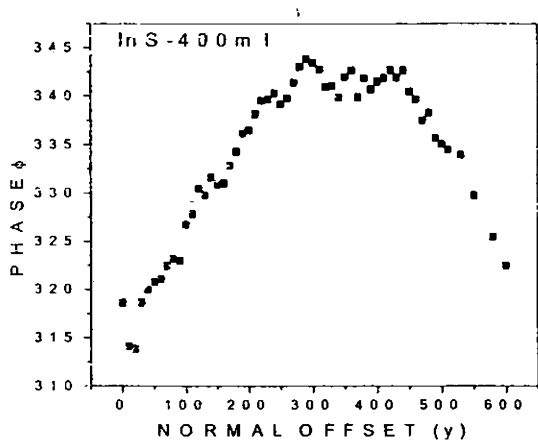


Fig 3.25(a) Normal offset dependency of phase

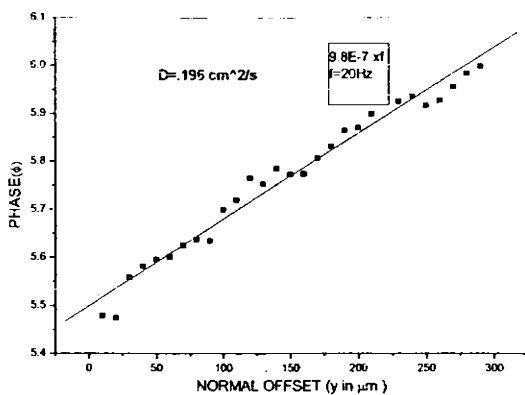


Fig 3.25(b) Linear fit of phase Vs normal offset curve

DEPENDENCE OF DEFLECTION AMPLITUDE ON FILM THICKNESS

The In_2S_3 samples were irradiated using Nd-YAG laser and the deflection amplitude was noted by increasing the chopping frequency. The deflection amplitude was different for the four samples and the deflection amplitude of sample sprayed with 1000ml solution was found to be the highest Fig. As the thickness is increased, the amount of energy absorbed by the sample increases and therefore photothermal generation and thus the deflection signal amplitude also increases. As the deflection amplitude depends on the film thickness this method can be used to check the uniformity of the sample thickness.

The experiment was repeated for two samples (sprayed with 400ml and 800ml) using He-Ne laser and we obtained the same result.

DEPENDENCE OF DEFLECTION AMPLITUDE ON FREQUENCY

As the frequency is increased the deflection amplitude falls off exponentially Fig 3.26 a to c . After a particular frequency the change in deflection amplitude is negligible. The signals obtained were as expected.

As explained in chapter 2, the deflection amplitude becomes a constant when the film thickness becomes equal to the thermal diffusion length. The thermal diffusion lengths were calculated for the frequencies corresponding to the point where the deflection amplitude was a minimum. This value would be equal to the film thickness.

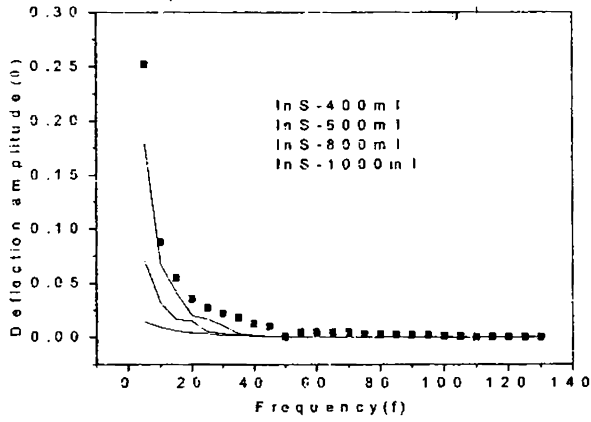


Fig 3.26(a) Deflection amplitude dependence on frequency

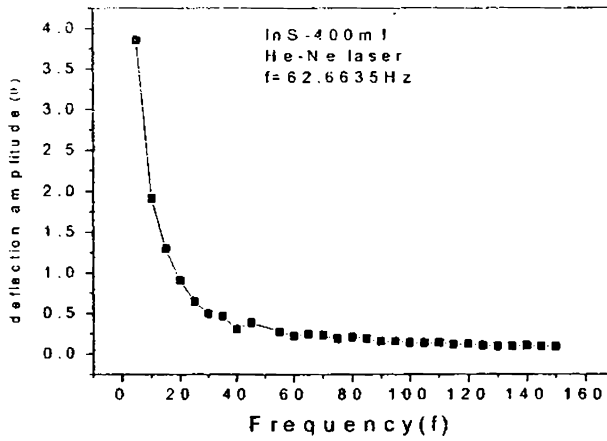


Fig 3.26(b) Deflection amplitude dependence on frequency

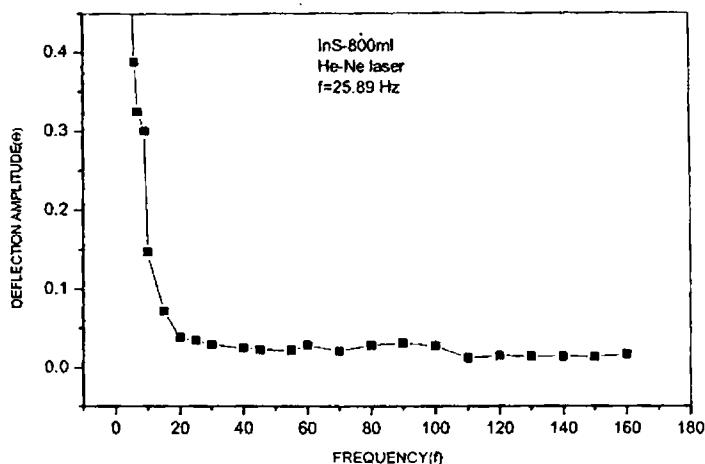


Fig 3.26 (c) Deflection amplitude Vs frequency (He-Ne laser)

The thickness of In_2S_3 -400ml was known to be about 1 micron. The ratio of the thermal diffusion lengths of In_2S_3 -800ml to In_2S_3 -400ml was found to be 2.42

Thus the method can be used to compare the film thickness directly, if the value of one film is known we can determine the thickness of other samples.

3.2.3 CuInS_2 thin films

CuInS_2 is a promising material for photovoltaic application due to its optimum direct and gap of 1.5eV, ease of type conversion and nontoxic constituents. It has been successfully used to fabricate both homojunction and heterojunction devices with appreciable conversion efficiencies.

The structure [Fig.3.27] and physical properties of copper indium sulfide thin films are given below.

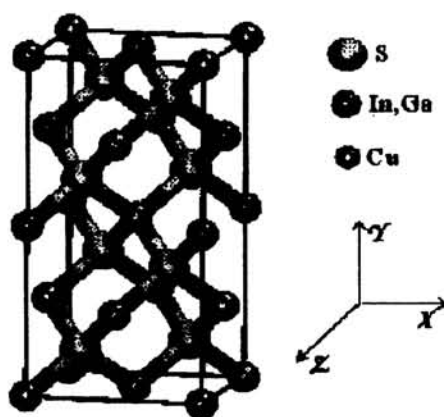


Fig.3.27 The tetragonal chalcopyrite structure of CuInS_2

Structure	: Tetragonal chalcopyrite
Colour	
Melting Temperature	: 1000 - 1050°C
Density	: 4739 kg/m^3
Lattice Parameters	: $a = b = 5.52 \text{ \AA}$ and $c = 11.13 \text{ \AA}$

The main function of this component is to absorb light and to convert its electromagnetic energy into the energy of electron-hole pairs. This last energy is of a chemical nature [3.6]. CuInS_2 possesses several exceptional material properties, which make it potentially well suited for photovoltaic applications. The energy gap of the absorbing material should match the spectral region

where the cell is expected to operate. CuInS_2 is having a direct band gap of 1.5 eV, which is the optimum value for solar energy conversion. The optical absorption coefficient of the absorber material has to be high in order to absorb most of the illumination energy within the thin layer. Indirect semiconductors, where the energy gap for indirect transitions is smaller than the energy gap for the direct ones, usually show too small optical absorption and require a complicated light-trapping scheme. Typical chalcopyrite semiconductors for solar cell applications like CuInSe_2 and CuInS_2 (CIS) are direct semiconductors, so that large absorption coefficients can be achieved here. This material can be prepared both in p-type and n-type form so that homojunction is possible. Messè et al predicted theoretical efficiencies between 27% and 32% for the CuInS_2 homojunction and this is the highest figure for any photovoltaic device [3.7].

Chemical Spray Pyrolysis (CSP) is a cost effective method by which uniform polycrystalline CuInS_2 thin films can be deposited over a large area. As Cu/In ratio as well as S/Cu ratio in the film directly depends on the concentration of CuCl_2 , InCl_3 and thiourea in the spray solution, one can easily control the stoichiometry of the sample using this technique. CuInS_2 thin films were deposited using chemical spray pyrolysis method on glass substrates. Experimental setup that has been used for deposition is schematically shown in the Fig 3.2. Cleaned glass slides are placed on a base plate with heater rods embedded in it to facilitate heating. The substrate temperature is maintained with the help of a feedback circuit that controls the heat supply. Temperature of the substrate can be varied from room temperature to 732K. Spray head and

the heater with substrate are kept inside a chamber provided with an exhaust fan for removing gaseous byproducts and vapors of solvent. During spray, temperature of substrate is kept constant with an accuracy of $\pm 5\text{K}$. The carrier gas and the solution are fed into the spray nozzle at predetermined and constant pressure and flow rate. Large area uniform coverage of the substrate is affected by scanning spray head employing electromechanical arrangements. In this work CuInS_2 thin film samples of varying thickness is studied. Thickness is varied by varying the volume of solution sprayed. The flow rate is kept a constant at $1\text{ml}/\text{min}$ and time of spraying is varied producing films of different thickness. Films are prepared using 20ml, 30ml, 40ml and 60ml volume of solution. Studies were carried out on CuInS_2 samples prepared with 20ml, 30ml, 40ml and 60ml solution using Automated spray pyrolysis technique. The variation in Thickness, Mobility and Thermal diffusivity of each sample was analyzed and the results are discussed below.

ANALYSIS OF THICKNESS

The Thickness was measured for different samples and was found to increase with increase in volume of the spray solution taken. A linear variation was found between the volume of sprayed solution and thickness as shown in Fig 3.28. The highest value of thickness was for sample prepared by spraying 60 ml solution ($0.33\ \mu\text{m}$) and lowest thickness was for sample prepared from 20 ml solution ($0.14\ \mu\text{m}$). The value of thicknesses measured was in agreement with the values obtained using standard stylus measurement.

ANALYSIS OF MOBILITY

Mobility of CuInS_2 thin films with different thickness were calculated using PTD method. It was seen that mobility increased with increase in volume of spray, from 20ml to 30ml . But interestingly mobility calculated for sample sprayed using 40 ml showed a decrease. The variation in mobility with volume of spray is shown in Fig 3.29. From XRD analysis as shown in Fig 3.30 a and b it was observed that this sample was having better crystallinity. The decrease in mobility may be attributed to the increase in surface roughness of the sample which may be due to the scattering of charge carriers. It was observed that films deposited with volume of solution greater than 40ml were highly porous. Mobility of sample prepared using 60 ml solution showed a sharp increase compared to other samples. This can be due to the difference in the preparation method of the sample. We had used multiple spray technique in preparing the sample in which CuInS_2 is deposited in 2 layers. During the preparation of the sample, at first a 40 ml solution was sprayed and annealed for half an hour and was allowed to cool, and over that a film was deposited by spraying 20 ml solution. The reported values of mobility measured by Hall method were found to be comparable with our measurements.

ANALYSIS OF THERMAL DIFFUSIVITY

Thermal diffusivity of CuInS_2 samples was studied for various volumes of sprayed solution. The plot for variation in thermal diffusivity with volume of spray is shown in Fig 3.31.

G9076

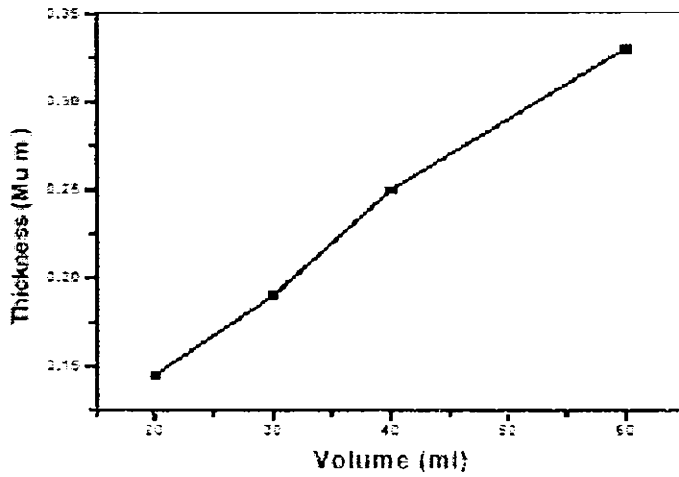


Fig 3.28 Variation between Thickness of sample and volume of sprayed solution

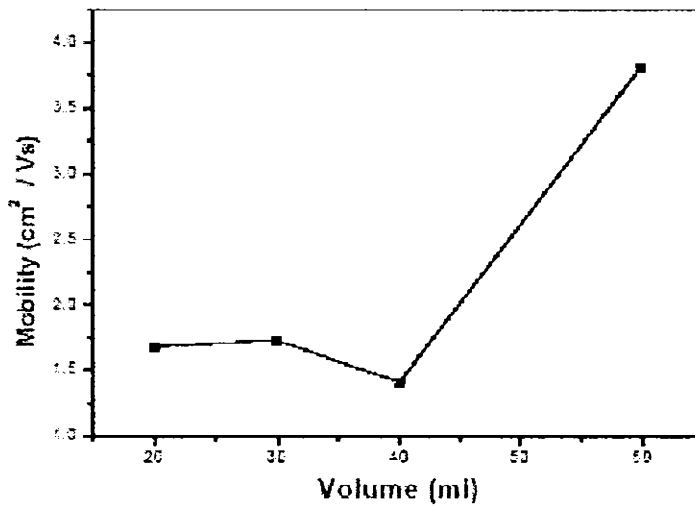


Fig 3.29 Variation in mobility with volume of sprayed solution

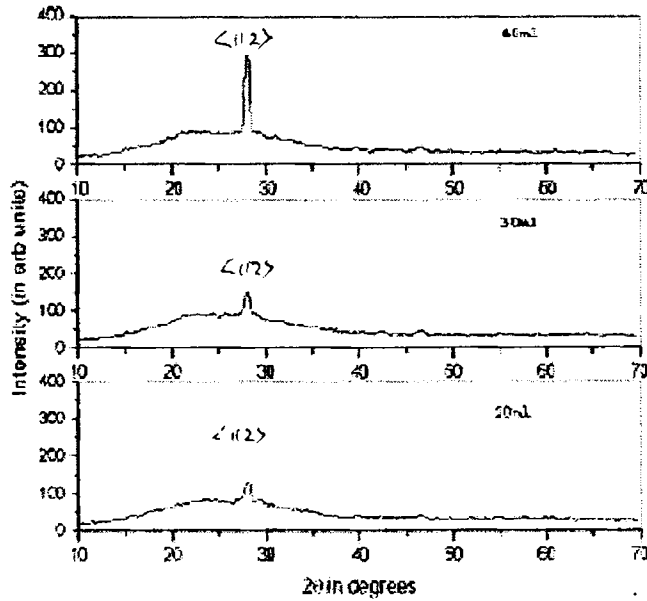


Fig 3.30 a XRD pattern for samples prepared using single spray.

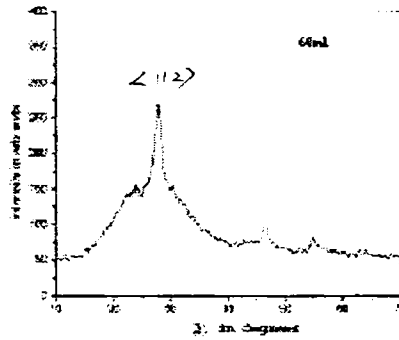


Fig 3.30 b XRD pattern for sample prepared using multiple spray.

Handwritten note: *Handwritten note: (112) XRD*

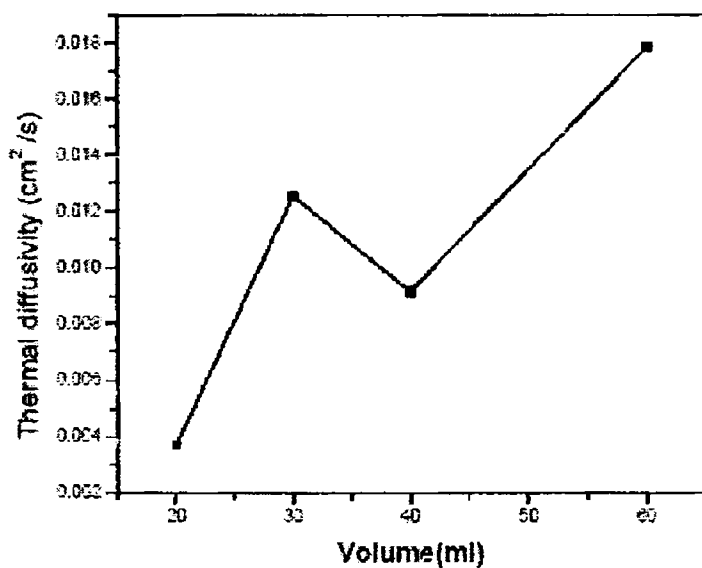


Fig 3.31 : Variation in Thermal diffusivity with volume of spray solution

Volume of solution sprayed(ml)	Mobility ₂ (cm ² /Vs)	Thermal Diffusivity ₂ (cm ² /s)
20	1.682	0.004
30	1.730	0.013
40	1.409	0.009
60	3.809	0.018

Comparison of Mobility and Thermal diffusivity for different samples

Volume of solution sprayed (ml)	Thickness measured by PTD (μm)	Thickness measured by Stylus (μm)
20	0.145	0.13
30	0.19	0.18
40	0.23	0.23
60	0.33	-

Comparison between thicknesses measured using PTD and stylus probe for different samples

Photothermal deflection spectroscopy can be used as an efficient tool for the determination of the thickness of thin films. The nondestructive, highly sensitive and contactless PBD technique can be used to decide the quality of thin films prepared by different methods such as chemical bath deposition, spray pyrolysis, and vacuum evaporation method. Based on the principle of optical beam deflection, transport parameters- thermal diffusivity and mobility of CuInS_2 thin films has been measured using Photothermal deflection technique. Its use as an efficient tool for the determination of thickness of thin films has been successfully demonstrated by this work. The thickness of CuInS_2 films deposited using the automated spray pyrolysis unit has been characterized. A linear dependence between the thickness of the film deposited and volume of sprayed solution has been realized. Thus dual beam PTD offers a novel means of characterizing thin films.

3.2.4 Rubbers

This group includes those materials in the Class A designation (no requirement regarding volume swell due to oil) and Types A and B designations (for continuous use not exceeding 70 and 100°C).

Natural rubber (NR, AA): The commercial base for natural rubber is latex, a milklike serum, generated by the tropical tree, *Hevea Brasiliensis*. The latex is collected in much the same fashion as maple sap. However, latex should not be confused with the sap of the tree. Latex is secreted in the inner bark of the tree, and a tree can be severely harmed if a tapping cut is deep enough to draw sap as well as latex. Naturally occurring latex is a dispersion of rubber in an aqueous serum containing various inorganic and organic substances. The rubber precipitated out of this solution can be characterized as a coherent elastic solid.

All other rubbers should be measured against natural rubber. For centuries it was the only rubber available, and it was used extensively, even before the discovery of vulcanization in 1839.

Synthetic rubbers have been developed either by accident or as the result of pressures of political upheaval or wartime restrictions and consequent unavailability of the natural product. However, no synthetic material has yet equaled the overall engineering characteristics and consequent wide latitude of application available with NR.

As with other rubbers, many grades and types of NR are available, produced by varying impurity levels, collection methods, and processing techniques. Natural rubber is generally considered to be the best of the general-purpose

rubbers -- those having properties and characteristics suitable for broad engineering applications. Compounds can be produced over a wider stiffness range with natural rubber than with any other material. Natural rubber is often the best choice for most applications except where an extreme performance or exposure requirement dictates the use of a special-purpose rubber, often at some sacrifice of other, less-critical characteristics.

Natural rubber has a large deformability capacity. This, coupled with its ability to strain crystallize, gives it added strength while deformed. Its high resilience, which is responsible for a very low heat buildup in flexing, makes NR a prime candidate for shock and severe dynamic loads. Thus, in applications where properties such as flexure, cut resistance, abrasion resistance, and general endurance would be adversely affected by heat in less-resilient rubbers, NR is recommended because of its low heat buildup.

NR also has low compression set and stress relaxation; these characteristics favor its application in sealing devices where maintenance of sealing forces and the surface conformability of high-quality soft stocks are important. Further advantages are excellent green (uncured) strength, building tack, and general processing characteristics.

Natural rubber does have some shortcomings. The useful service temperature of NR ranges generally from -65 to (in special cases) 250°F. Other drawbacks of NR such as poor oil, oxidation, and ozone resistance can be minimized, either by proper design accommodation and/or by compounding. Degradation from such environments are essentially surface effects that can be tolerated or minimized by using thicker cross sections, by shielding, or by adding antioxidants and antiozonants.

Natural rubber can often be the first choice for many high-performance applications if it can be made to survive in the service environment. It remains the best choice for tires, shock mounts and other energy absorbers, seals, isolators, couplings, bearings, springs, and dynamic applications.

Synthetic natural rubber (IR; AA): The synthetic rubber that is closest to duplicating the chemical composition of natural rubber is synthetic polyisoprene. It shares with natural rubber the properties of good uncured tack, high unreinforced strength, good abrasion resistance, and those characteristics that provide good performance in dynamic applications. However, because of some of the inherent impurities in the natural product that affect vulcanization characteristics in a positive fashion, natural rubber scores somewhat better on overall ratings.

A significant disadvantage of IR is its lack of green strength. IR can be used interchangeably for natural rubber in all but the most demanding applications. Specific product applications are about the same as those for natural rubber.

Styrene butadiene (SBR; AA, BA): This material emerged as a high-volume substitute for NR during World War II because of its suitability for use in tires. Despite the fact that the basic feedstock for SBR is crude oil, it has remained competitive in cost because of the extensive production capacity for SBR in the U.S.

SBR continues to be used in many applications where it replaced NR, even though it does not have the overall versatility of natural rubber and the other general-purpose materials. For most applications, SBR must be reinforced

(hence, stocks are stiffer) to have acceptable tensile strength, tear resistance, and general durability. SBR is significantly less resilient than NR, so it has higher heat buildup on flexing. Further, it does not have the processing and fabricating qualities of NR, lacking both green strength and building tack.

An important reason for the continued high volume use of SBR is that it did a creditable job in passenger car tires, having good abrasion resistance and general durability. Recently that picture has changed, however, because of the greater need for the green strength and building tack of natural rubber in radial tires and for the better low-temperature flexibility of natural rubber for snow tires. High-performance tires, such as for trucks and aircraft, have always been made from natural rubber if it was available.

Polybutadiene (BR; AA): This general-purpose, crude-oil-based rubber is even more resilient than natural rubber. It was the material that made the solid golf ball possible. It is also superior to natural rubber in low-temperature flexibility and in having less dynamic heat buildup. However, it lacks the toughness, durability, and cut-growth resistance of NR. It can be used as a blend in natural rubber or SBR to improve their low-temperature flexibility. Silicones have superior low-temperature flexibility, but this is achieved at a much higher price and at a sacrifice in other properties such as tensile strength, tear resistance, and general durability.

A large volume of polybutadiene is used in blends with other polymers to enhance their resilience and reduce heat buildup. It is also used in products

requiring high resiliency over a broad temperature range such as industrial tires and vibration mounts.

Butyl (IIR, CIIR, AA, BA): The two types of rubber in this category are both based on crude oil. The first is polyisobutylene with an occasional isoprene unit inserted in the polymer chain to enhance vulcanization characteristics. The second is the same, except that chlorine is added (approximately 1.2% by weight), resulting in greater vulcanization flexibility and cure compatibility with general-purpose rubbers.

Butyl rubbers have outstanding impermeability to gases and excellent oxidation and ozone resistance. The chemical inertness is further reflected in lack of molecular-weight breakdown during processing, thus permitting the use of hot-mixing techniques for better polymer/filler interaction.

Flex, tear, and abrasion resistance approach those of natural rubber, and moderate-strength (2,000 psi) unreinforced compounds can be made at a competitive cost. Butyls lack the toughness and durability, however, of some of the general-purpose rubbers.

The attribute responsible for the high-volume use of butyl rubber in automotive inner tubes and tubeless tire interliners is its excellent impermeability to air. Butyls are also used in belting, steam hose, curing bladders, O-rings, shock and vibration products, structural caulks and sealants, water-barrier applications, roof coatings, and gas-metering diaphragms.

Ethylene propylene (EPR, EPDM; AA, BA, CA): Like the butyls, the EP rubbers are of two types. One is a fully saturated (chemically inert) copolymer of ethylene and propylene (EPR); the other (EPDM) is the same as this plus a third polymer building block (diene monomer) attached to the side of the chain. EPDM is chemically reactive and is capable of sulfur vulcanization. The copolymer must be cured with peroxide.

Physical properties of EPR and EPDM are not as good as those obtainable with NR. However, property retention is better than that of NR on exposure to heat, oxidation, or ozone. Bonding is somewhat more difficult, especially with EPR. These materials have broad resistance to chemicals but not to oils and other hydrocarbon fluids. Electrical properties are good.

Typical applications are automotive hose; body mounts and pads; O-rings; conveyor belting; wire and cable insulation and jacketing; window channeling; and other products requiring resistance to weathering. EPDM sheeting, either unsupported or reinforced, is used in roofing and as liners for water conservation and pollution-control systems.

Photothermal studies were carried out on CIIR / EP samples with varying EP content on its impact on the thermal properties. The results are shown below in Figures 3.32 and 3.33

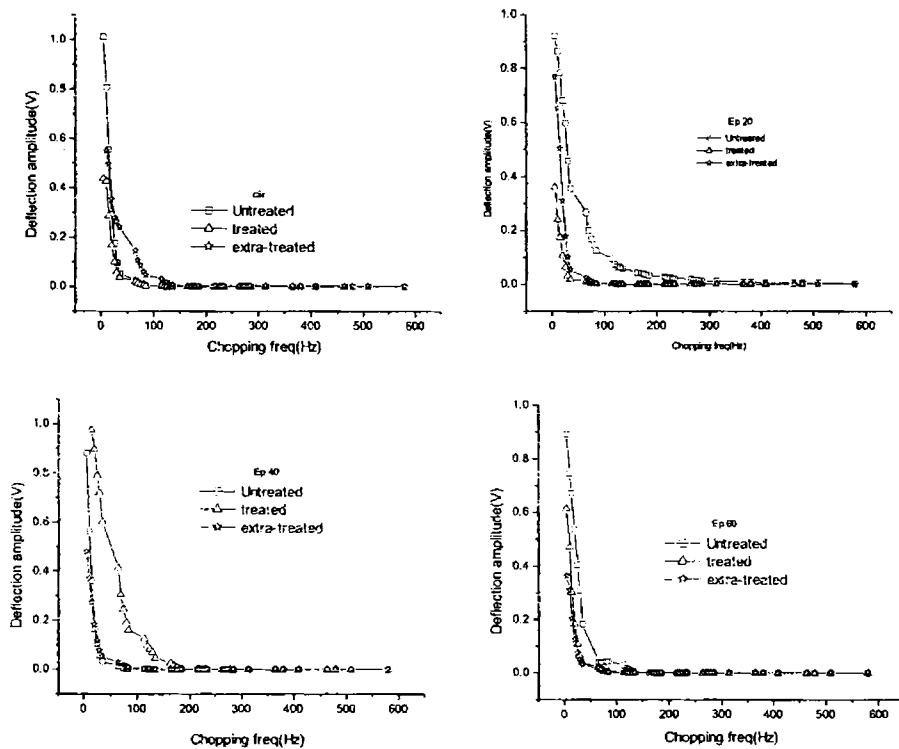
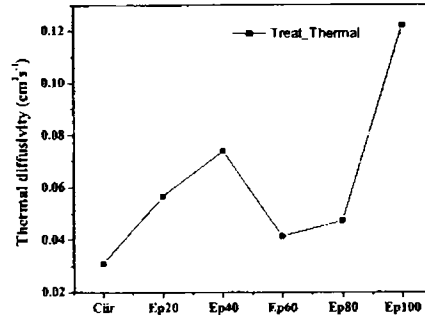
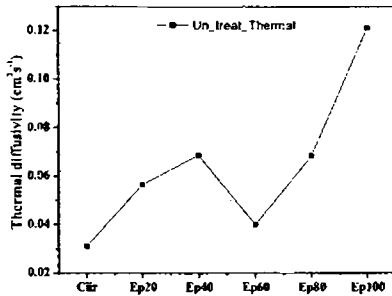
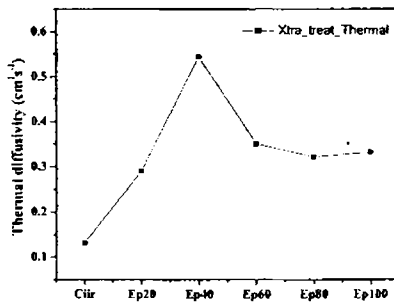


Fig 3.32 PTD signal for CIIR, EP20, EP40, EP60 samples for various heat treatment



Sample Untreated	Dth(cm ² /s)
Ciir	0.031
Ep20	0.0565
Ep40	0.0685
Ep60	0.0399
Ep80	0.0682
Ep100	0.1211

Sample Treated	Dth(cm ² /s)
Ciir	0.031
Ep20	0.0565
Ep40	0.0739
Ep60	0.0414
Ep80	0.0473
Ep100	0.1221



Sample Xtra treated	Dth(cm ² /s)
Ciir	0.1319
Ep20	0.2909
Ep40	0.5445
Ep60	0.351
Ep80	0.3212
Ep100	0.3327

Figure 3.33 Thermal diffusivity dependence on % of EP and heat treatment

3.2.5 Poly Urethane with fillers

Effect of addition of fillers on the thermal properties of Poly Urethane studied with Photothermal Spectrometer.

Sample details

The sample used for this measurement was from a composition which was developed for encapsulating/potting heat generating devices. Polyurethane prepared from Empeyol sp101 and MDI Cosmonate LK from Manali petrochemicals , Chennai was used as the polymer matrix. The thermal conductivity of PU was enhanced by addition of fillers[Fig 3.34].

Preparation of sample

The required amount of SP 101 and Cosmonate LK were weighed out in the ratio (100 : 30) to prepare samples. This was mixed thoroughly and filler was added immediately. Stirring was continued till the filler got dispersed in the polymer. Entrapped air was removed by applying vacuum . The mixture is then poured into mould for casting samples. The samples were removed after 24 hours.

Sample	sample id	Thermal diffusivity ($\times 10^{-6} \text{m}^2/\text{s}$)
PolyUrethane(PU)	1a	0.00113
PU+Mica	2a	0.02561
PU+BN(1g)	3a	0.2951
PU+BN(0.1g)	4a	0.1112
PU+ZnO(1g)	5a	0.0313
PU+BN(0.5)+Mica(0.5)	6a	0.0503
PU+BN(0.5)+Silica(0.5)	7a	0.3513
PU+Silica(1g-ppt)	8a	0.2879
PU+BN(0.1)+ZnO(0.9)	9a	0.4115
PU+BN(0.1)+Al ₂ O ₃ (0.9)	10a	0.09034
PU+Al ₂ O ₃ (1g)	11a	0.1122
PU+Silica(1g-Ultrafine)	12a	0.0615
PU+BN+ZnO(2.5)	13a	0.0485

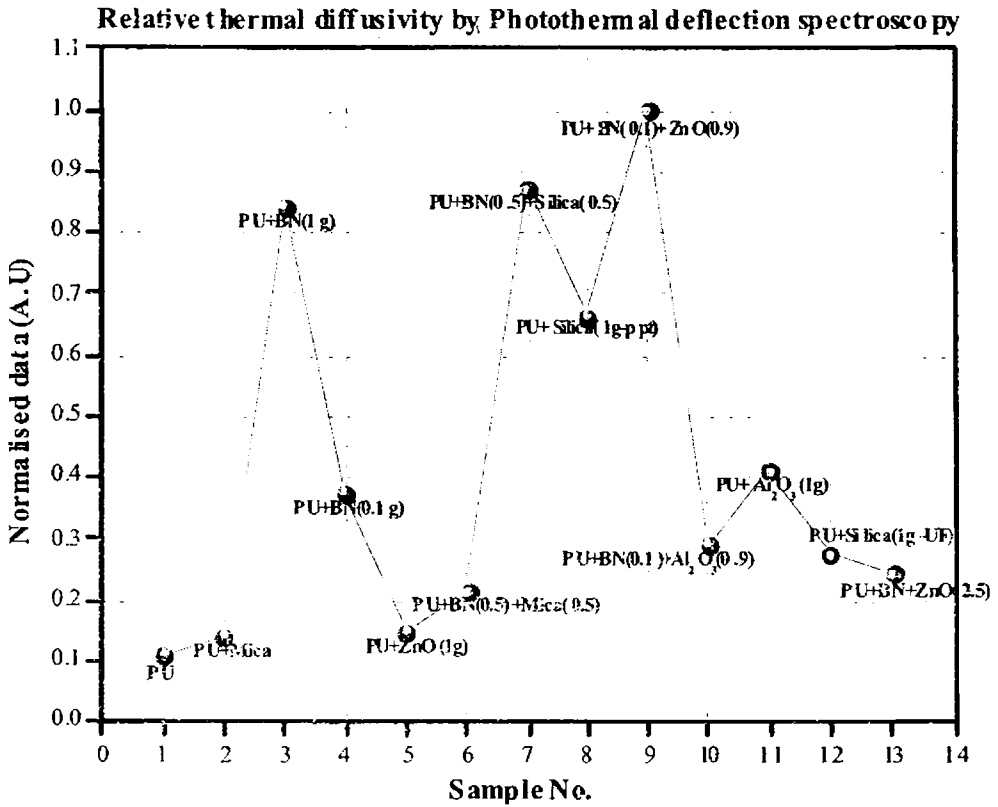


Figure 3.34 Variation in thermal property due to filler addition

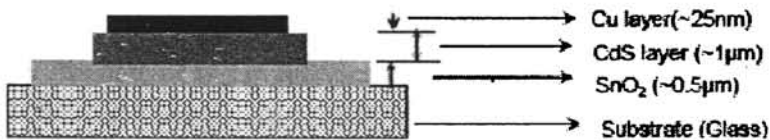
Thus it was proved that the synergy of fillers yielded a low cost alternative to Boron Nitride with the addition of ZnO. Addition of 0.1 gm of BN to 0.9 gm of ZnO yielded the sample with thermal diffusivity higher than that of BN alone.

3.2.6 He⁺ implanted CdS

Cadmium sulfide had long been used widely in opto electronics and microelectronics due to its good optical and electrical properties. Pure and doped monocrystals and thin layers of this material are often used in photoconducting, photovoltaic and optoelectronic devices [3.8]. CdS is well known for its tendency to form nonstoichiometric compound, having excess cadmium, leading to n-type conductivity. The kind and number of defects and hence the electric, optical and luminescent properties of the material depend on the technique of sample preparation and its thermal history [3.9]. Thin films of CdS have been prepared by several techniques such as sputtering [3.10], evaporation [3.11], serigraphy [3.12], chemical vapor deposition [3.13], chemical spray pyrolysis [3.14] and chemical bath deposition [3.15, 16]. Production of large surface area CdS thin films by easy and low cost techniques for industrial use is of great importance. Chemical spray pyrolysis method has proved to be a reliable technique for this [3.17-20]

He⁺ ion implantation in CdS thin film samples

Cu was deposited using vacuum evaporation technique, at pressure of 10^{-5} torr over a masked area on "Type I" sample as shown below.



He⁺ ions were also implanted in this sample, using a low energy accelerator (J-15 Sames 150 kV accelerator) for various accelerating voltages from 60 keV, 80 keV, 100 keV and 120 keV maintaining a constant dosage of 5×10^{16} He⁺

ions/cm². Beam current was maintained around 0.5 to 0.8 μA , to avoid heating effect during ion implantation. Implantation was carried out at room temperature in vacuum (10^{-5} torr). The idea of increasing the acceleration energy of the ions is to penetrate deeper into the material.

The proposed structure of an ion-implanted semiconductor wafer is schematically presented in Fig 3.35. A three-layer structure is assumed: a surface layer, an ion-implanted layer, and a substrate layer. The surface layer represents a region traversed by the implanted ions. The ions do not reside within this region. The thickness of this upper layer depends on the implantation species and energy. The second region represents the implanted layer where damage is maximum. The thickness of this implanted layer depends on both the implantation energy and the implantation dose. For a given species, the thickness is mainly controlled by the implantation energy. For a given energy the thickness increases with increasing implantation dose. The third region is the remaining wafer and features transport and optical properties similar to the intact bulk wafer. The thicknesses of the three layers are denoted as L_1 , L_2 , and L_3 , respectively.

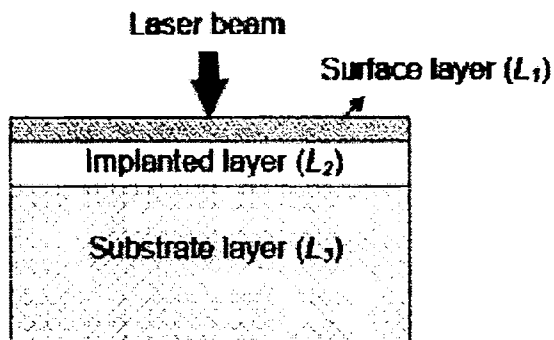
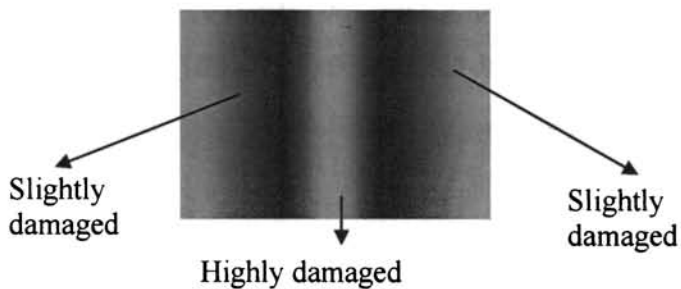


Fig 3.35 Proposed 3 layer model of Ion implanted CdS

Since the actual damage profile in the substrate material is a continuously inhomogeneous region of compromised integrity above a crystalline substrate rather than regions with distinct boundaries, the optical and electrical properties, as well as the thickness, of the second layer in the assumed model represent weighted averages over the region affected by implantation. When the thickness of the damaged layer is small relative to the carrier diffusion length in the material the actual inhomogeneous layer can be expected to have effects on the carrier density wave, and consequently the signal, similar to that of a discrete homogeneous damaged layer with transport properties that are a weighted average of the actual property profile and the assumed layer thickness.

Similarly, when the thickness of the damaged region is small relative to the optical absorption depth of the excitation source the influence of the actual damage profile on the optical intensity as a function of the depth can be expected to be similar to that of a homogeneous layer with optical properties determined by some average of the actual optical property profile and the assumed layer thickness.

Sample structure

Various energies			
	L1(μm)	L2(μm)	L3(μm)
60 keV	0.21	0.83	0.5
80 keV	0.35	0.65	0.5
100 keV	0.5	0.51	0.5
120 keV	0.72	0.3	0.5

Various dosages

$\text{He}^+_{\text{ion}}/\text{cm}^2$	L1(μm)	L2(μm)	L3(μm)
1×10^{15}	0.4	0.3	0.5
1×10^{16}	0.3	0.3	0.5
1×10^{17}	0.6	0.43	0.4

Photothermal studies on He^+ implanted CdS on the damage model yielded the damage distribution as given in table above. Attempts to arrive at appropriate theoretical model are on at this point of time.

REFERENCE:

- 3.1 H. G. Ansell and R. S. Boorman *J. Electrochem. Soc.* 118 (1971) 133
- 3.2 H. Hahn and W. Klinger *Z. Inorg. Chem.* 260 (1949) 97
- 3.3 C. J. X. Rooymans *J. Inorg. Nucl. Chem.* 260 (1959) 78
- 3.4 J. V. Landuyt, H. Hatwell and S. Amelinckx *Mater. Res. Bull.* 3 (1968) 59
- 3.5 M. Ortega – Lopez and A. Morales- Acevedo *Thin Solid Films* 330 (1998) 96
- 3.6 P. Würfel *Physica E* 14 (2002) 18
- 3.7 J. M. Meese, J. C. Manthuruthil and D. R. Locker *Bull. Amer. Phys. Soc.* 20 (1975) 696
- 3.8 E. Gutsche and J. Voigt, *Proceedings of 7th International Conference on IIVI, Semiconducting Compunds*, held at New York, USA (1967) pp 755.
- 3.9 M. Grus and A. Sikorska, *Physica B*, 266 (1999) 139.
- 3.10 V. D. Vankar and K. L. Chopra, *Phys. Stat. Sol. (a)*, 45 (1978) 665.
- 3.11 S. Vodjani, A. Sharifnai and M. Doroudian, *Electron. Lett.*, 9 (1973) 128.
- 3.12 S. D. Sathaya and A.P.B. Sinha, *Thin Solid Films*, 37 (1976) 15.
- 3.13 Alok K. Berry, P. M. Amirtharaj, Jack L. Booney and Don D. Martin, *Thin Solid Films*, 219 (1992) 153.

- 3.14 B.K. Guptam, O.P. Agnihotri and A. Raza, *Thin Solid Films*, 48 (1978)153.
- 3.15 Inderjeet kaur, D.K. Pandya and K.L. Chopra, *J. Electrochem. Soc.*, 127(1978) 943.
- 3.16 K.L. Narayanan, K.P. Vijayakumar, K.G.M. Nair and G.V.N. Rao, *Bull.Mater. Sci.* 20 (1997) 287.
- 3.17 M. A. Martinez, G. H. Herrero and M. T. Gutierrez, *Sol. Energy Mater.Sol. Cells*, 45 (1997) 75.
- 3.18 B. T. Boike, G. S. Khripunov, V. B. Yurchenko and H.E. Ruda, *Ibid.*, 45(1997) 303.
- 3.19 J. Touskova, D. Kindl and J. Tousek, *Thin solid films*, 293 (1997) 272.
- 3.20 A. Niemegeers and M. Burgelman, *J. Appl. Phys.*, 81 (1997) 2881.

This work was started with the financial support from DST vide a project under SERC scheme.

“Some of the significant and interesting results obtained in ongoing projects were as follows

- A Photothermal Deflection Spectroscopy (PDS) system to record absorption spectrum in the range 400nm to 2200nm has been set up at the Cochin University of Science and Technology, Kochi. Several samples of ion implanted and amorphous semiconductors have been studied.

From the annual Report DST Govt. of India, 2000-2001”

Reference for vibration isolation:

Ealing Electro-Optics Product Guide. Ealing Electro-Optics, Inc., 22 Pleasant Street, South Natick, MA 01760,617/655-6029.

Melles Griot Opt Guide 3. Melles Griot, 1770 Kettering Street, Irvine, CA 92714,714/261-5600

The Newport Corporation Catalog of Precision Laser/Optics Products. *No 100*. Newport Corporation (formerly NRC), 18235 Mount Baldy Circle, Fountain Valley, CA 92728-8020,714/963-9811.

Oriel Corporation Catalog Vol. I of Tables, Benches. Micropositioners, Optical Mounts. Oriel Corporation, 250 Long Beach Boulevard, Stratford, CT 06497-0872,203/377-8282.

Chapter 4

Lock in Detection

4.1 Why lock in detection?

There are many instances in scientific measurement when we are looking for a small signal that is often embedded in large amounts of background and/or noise. The situation is especially bad when the signals are constant in time, because $1/f$ noise becomes very important at low frequencies. To improve the ability to measure small signals, one of the most important solutions is to modulate the signal in some way. If the desired signal depends on specific variables, then by modulating these variables (intensity, voltage, etc) and looking for the resulting change in signal, the signal-to-noise ratio can be improved.

In a spectroscopy experiment looking at fluorescence, for example, one could modulate the intensity of light impinging on the sample, the wavelength of excitation, or the polarization of light (if you expect the signal to be polarization dependent, such as spectroscopy at a surface or interface). In an electrical measurement of current, one could modulate the applied voltage. There are many quantities that can be varied to produce a modulation of the signal one is looking for. The essential point is that by modulating one of these quantities as a function of time (at a specific frequency), one can put the desired signal at that frequency, well away from important noise sources (such as $1/f$ noise, electrical noise, etc.). It is then possible to extract the desired signal from the “noise” by using a variety of filtering techniques. The most important of these is the use of “synchronous demodulation”, which is a

way of measuring the component of signal that is synchronized in frequency and phase with a reference signal. Synchronous demodulation is often termed “phase-sensitive” detection and is often accomplished with a “lock-in” amplifier.

The modulation of an experimental quantity can be accomplished in a number of ways. The simplest method is to modulate the amplitude of a signal, which is generically referred to as “amplitude modulation”. For slowly-varying signals, the modulation can consist of a number of methods. These include:

a) Modulation the intensity of light using a mechanical chopper or other device,

b) Modulating an applied voltage, as in impedance spectroscopy measurements
In effect, the application of a modulation can be thought of in two different regimes: one a “small-amplitude” modulation and the other a “large-scale” modulation.

The second approach to modulation is to use *large-amplitude* modulation. In which a signal is essentially modulated between an “off” state and an “on” state. A good example would be the use of an optical chopper to turn a light source off and on.

Once the signal is modulated, it can be amplified, filtered, and processed in a number of ways.

4.2 The basic lock in strategy

Ultimately, one needs to measure the amplitude of the signal. There are two fundamentally distinct ways of doing this:

4.2.1 Asynchronous detection:

In this case, we simply measure the amplitude of the AC signal. The simplest way of doing this is to pass the AC signal through a diode, and measure the RMS voltage across the diode. This method is commonly used in radio and microwave circuits.

4.2.2 Synchronous (“lock-in”) detection:

In this case, we measure the amplitude of the signal using reference signal that has a well-defined phase with respect to the signal. Synchronous detection is much better at reducing noise. In fact, synchronous detection can even reject noise at the same frequency as the signal, because “noise” will have a random phase, while the lock-in looks for signals with the same frequency and phase as the reference signal. The lock-in amplifier is one of the most important electronic instruments for measuring small signals; it is available as a stand-alone instrument, and is also built into many common laboratory instruments.

The lock-in amplifier typically consists of the following essential components:

- 1) A phase-locked loop, usually also including a phase shifter
- 2) A mixer (demodulator)
- 3) A low pass filter

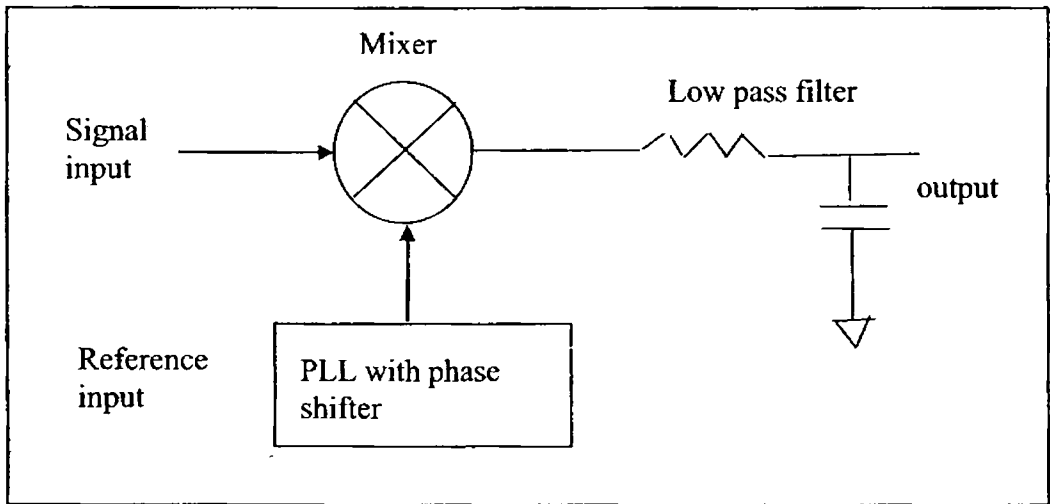


Fig 4.1 Block diagram of Lock in amplifier

The purpose of the phase-locked loop is to create a well-defined reference signal that is “clean” --meaning that it has a well-defined shape (typically either a square wave or a sine wave) and has fixed amplitude. Many times when a signal is modulated, the modulation signal X_{mod} may have a poorly defined shape or might have amplitude that is not a precise, fixed value. A phase-locked loop is almost always used to create a more precise, fixed-amplitude reference signal. Additionally, the PLL almost always includes a phase shift circuit, in order to make sure that the phase of the reference signal matches that of the signal.

4.2.3 The theory of lock in detection

The mixer (“synchronous demodulator”) is the heart of the lock-in. Its primary function is to multiply the cleaned-up reference signal $\cos(\omega_{\text{ref}}t)$ by the input

signal $S(t) = \cos(\omega_{\text{sig}}t)$. In general, the reference signal should be sinusoidal with a possible phase shift, $R(t) = R_0 \cos(\omega_{\text{ref}}t + \phi)$.

If the signal $S(t)$ is represented as its Fourier series:

$$S(t) = S_{\text{DC}} + A_{1\omega} \cos(\omega t) + A_{2\omega} \cos(2\omega t) + A_{3\omega} \cos(3\omega t) + \dots \\ + B_{1\omega} \sin(\omega t) + B_{2\omega} \sin(2\omega t) + B_{3\omega} \sin(3\omega t) + \dots \quad 4.1$$

where we have included both cosine and sine terms.

Then the product gives:

$$R(t) * S(t) = S_{\text{DC}} \cos(\omega t) + A_{1\omega} \cos(\omega t) \cos(\omega t) + A_{2\omega} \cos(2\omega t) \cos(\omega t) + A_{3\omega} \cos(3\omega t) \cos(\omega t) + \dots \\ + B_{1\omega} \sin(\omega t) \cos(\omega t) + B_{2\omega} \sin(2\omega t) \cos(\omega t) + B_{3\omega} \sin(3\omega t) \cos(\omega t) + \dots \quad 4.2$$

If the “reference” and the “signal” have the same frequency but are phase shifted, then the output of the lock-in is decreased; when they have exactly the same phase the signal is maximized. So, to optimize the response of the single-phase lock-in amplifier, one must look at the output signal and adjust the phase-shifter until the signal is maximized. In many cases this is difficult to do, especially for extremely small signals. Consequently, it is common to use a dual-phase lock-in amplifier. In this case, a second reference signal is generated, 90° out of phase with the first, and the signal is applied to two mixers as shown in Fig 4.2

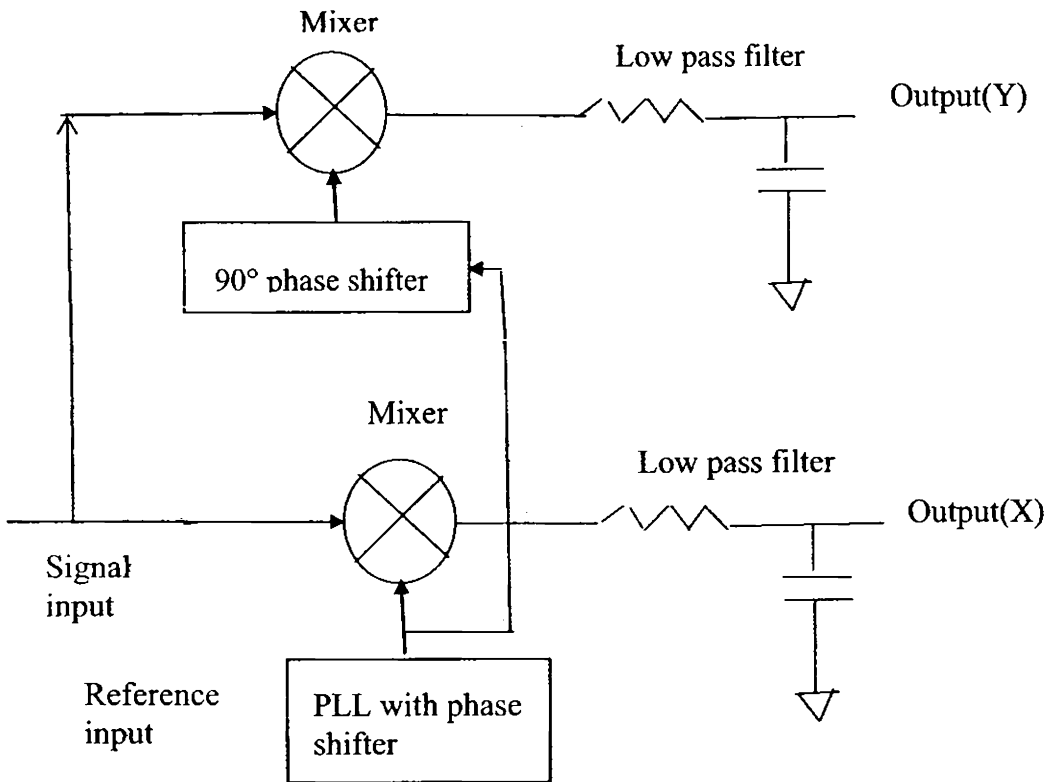


Fig 4.2 Block diagram of Dual phase lock-in amplifier

Each mixer sees the same “signal” input, but they see “reference” signals that are shifted in phase by 90° with respect to one another. The advantage of the dual-phase lock-in is that it simultaneously extracts both the Fourier cosine and Fourier sine coefficients of the input signal. Output “X” is the same as the single-phase lock-in, but the second output “Y” gives the out-of-phase component. By the Pythagorean theorem, the total magnitude of the signal at the reference frequency can be found as

$$\langle S(t)_{RLC} \rangle = \sqrt{X^2 + Y^2} \quad 4.3$$

and if the internal phase shifter is set to zero, then the phase of the signal with respect to the input signal can be found as

$$\phi = \tan^{-1} \left(\frac{Y}{X} \right) \quad 4.4$$

The primary advantage of the dual-phase lock-in is that if one is only interested in the magnitude of the signal, then there is no need to adjust the internal phase shifter that is part of the PLL. If the internal phase shifter is adjusted to zero (so that the signal applied to the “X” mixer is in phase with the original reference signal input), then one can directly extract both the magnitude and phase of the signal without any adjustments.

A full, stand-alone lock-in will have several other features. Common features include:

- 1) Variable gain amplifiers at the input
- 2) Internal current-to-voltage converter for measuring currents if desired
- 2) Bandpass and/or high-pass filters on the input before the mixer
- 3) Additional gain stages after the mixer

4.4 Harmonics:

The functioning of the lock-in is based on the assumption that the reference signal consists of a perfect sine wave. If the reference signal has some other waveform, then we need to consider all the Fourier components of the reference signal as well. Most important is the fact that if $\text{Ref}(\omega t)$ is a square wave, then in addition to the component at ω , it contains Fourier components at 3ω , 5ω , and all other odd harmonics. If such a reference signal is mixed with an input signal $S(t)$, then the Fourier components of $\text{Ref}(t)$ at 3ω will mix with the signal components at 3ω , producing additional, non-zero contributions to the averaged output. The influence of harmonic signals is reduced by:

- 1) using a good-quality sine wave as the reference input, and
- 2) Using a bandpass filter on the input signal $S(t)$ centered at the reference frequency ω , to attenuate any signals that, when mixed with possible harmonics of the reference signal, could generate an output signal at zero frequency.

We assumed that signals that have frequencies different from that of the reference signal are averaged away. While is largely true; however, there are limits. If a “noise” signal is 1 Hz away from our signal, then after mixing the “noise” will produce an output signal at 1 Hz; the low-pass filter on the output of the lock-in usually has a low cutoff, but in order to rid of these very low-frequency components, the output filter must be set to be extremely low in frequency, which also means very sluggish operation of the lock-in. (If the low-pass filter is set to a time constant of 1 second, then if the desired input signal is varying in time, you must wait approximately 3- 5 times this (i.e., 3 -5 seconds) before the lock-in output will accurately settle to the final value. The

lock-in is essentially a filter having a bandpass equal to $1/T$, where T is the time constant of the output filter. Time constants of ~ 0.1 second to ~ 3 seconds are commonly used.

4.5 The Typical Lock-In Amplifier

The block diagram of a typical lock-in amplifier is shown in figure 4.3.

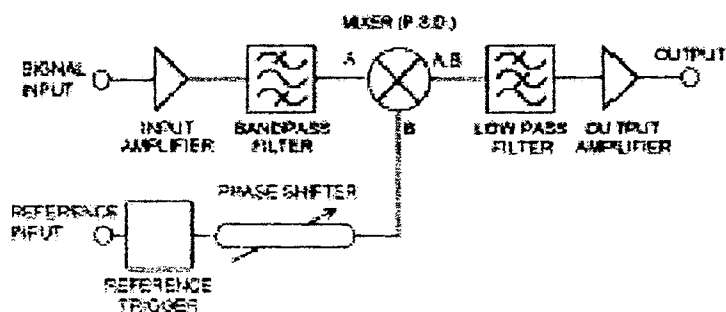


Fig 4.3 The block diagram of a typical lock-in amplifier

4.5.1 Signal Channel

In the signal channel the input signal, including noise, is amplified by an adjustable-gain, AC-coupled amplifier, in order to match it more closely to the optimum input signal range of the Mixer or Phase Sensitive Detector (P.S.D). Instruments are usually fitted with high impedance inputs for voltage measurements. Many also incorporate low impedance inputs for better noise matching to current sources, although in some cases the best results are obtained through the use of a separate external preamplifier. The performance of the PSD is usually improved if the bandwidth of the noise voltages reaching it is reduced from that of the full frequency range of the instrument. To achieve this, the signal is passed through some form of filter, which may be simply a band rejection filter centered at the power line frequency and/or its second

harmonic to reject line frequency pick-up, or alternatively a more sophisticated tracking bandpass filter centered at the reference frequency.

4.5.2 Reference Channel

It has been shown that proper operation of the PSD requires the generation of a precision reference signal within the instrument. When a high-level, stable and noise-free reference input is provided, this is a relatively simple task. However there are many instances where the available reference is far from perfect or symmetrical, and in these cases a well designed reference channel circuit is very important. Such circuits can be expensive and often account for a significant proportion of the total cost of the instrument. The internally generated reference is passed through a phaseshifter, which is used to compensate for phase differences that may have been introduced between the signal and reference inputs by the experiment, before being applied to the PSD.

4.5.3 Phase-sensitive Detector

There are currently three common methods of implementing the PSD, these being the use of an Analog Multiplier, a Digital Switch or a Digital Multiplier.

4.5.3.1 Analog Multiplier

In an instrument with an analog multiplier, the PSD comprises an electronic circuit which multiplies the applied signal with a sinewave at the same frequency as the applied reference signal. Although the technique is very simple in principle, in practice it is difficult to manufacture an analog multiplier which is capable of operating linearly in the presence of large noise, or other interfering, signals. Non-linear operation results in poor noise rejection and thereby limits the signal recovery capability of the instrument.

4.5.3.2 Digital Switching Multiplier

The switching multiplier uses the simplest form of demodulator consisting of an analog polarity-reversing switch driven at the applied reference frequency. The great advantage of this approach is that it is very much easier to make such a demodulator operate linearly over a very wide range of input signals. However, the switching multiplier not only detects signals at the applied reference frequency, but also at its odd harmonics, where the response at each harmonic relative to the fundamental is defined by the Fourier analysis of a squarewave. Such a response may well be of use if the signal being detected is also a squarewave, but can give problems if, for example, the unit is being used at 1 kHz and there happens to be strong interfering signal at 7 kHz. As discussed earlier, the use of a tuned low-pass or bandpass filter in the signal channel prior to the multiplier modifies the response of the unit so that it primarily detects signals at the reference frequency. However, in order to fully reject the 3F response, while still offering good performance at the reference frequency, very complex and expensive filters would be required. These are impractical for commercial instruments, so units fitted with filters tend to show some response to signals and noise at the third and fifth harmonics of the reference frequency and relatively poor amplitude and phase stability as a function of operating frequency. PerkinElmer Instrument's analog lock-in amplifiers use an alternative and more sophisticated type of switching demodulator which replaces the single analog switch with an assembly of several switches driven by a Walsh function. This may be thought of as a stepped approximation to a sinewave. Careful selection of components allows such a demodulator to offer all of the advantages of the switching demodulator

with one additional benefit, which is the complete rejection of the responses at the third and fifth harmonics and reduced responses for higher orders. Such a demodulator, when used with a relatively slow roll-off, 4th-order, low-pass filter in the signal channel, produces an overall response very near to the ideal. In this case the demodulator rejects the third and fifth harmonic responses and the higher orders are removed by the signal channel filter.

4.5.3.3 Digital Multiplier

In an instrument employing this type of multiplier the input signal is amplified and then immediately digitized. This digital representation is then multiplied by a digital representation of a sinewave at the reference frequency. A digital signal processor (DSP) is used for this task and the output is therefore no longer an analog voltage but rather a series of digital values. The technique offers the advantages of a perfect multiplication with no inherent errors and minimizes the DC coupled electronics that are needed with other techniques, thereby reducing output drift. It has been used for a number of years in such applications as swept-frequency spectrum analyzers. There are, however, a number of major problems with this method when applied to recovering signals buried in noise. The most important of these is dynamic range. Consider the case of an input signal in the presence of 100 dB (100,000 times larger) of noise. If the signal is to be digitized to an accuracy of “n” bits then the input converter must handle a dynamic range of $2^n \times 100,000$ to fully accommodate the signal and noise amplitudes. With a typical value for n of 15, this equates to a range of $3.2 \times 10^9:1$, corresponding to 32 bits. An analog to digital converter (ADC) can be built with such an accuracy, but would be extremely expensive and quite incapable of the sampling rates needed in a

lock-in amplifier operating to 100 kHz. Practical digital lock-in amplifiers use a 16 or 18-bit ADC. Consequently, in the presence of strong interfering signals, the required signal may only be changing the least significant bits of the converter, and indeed may actually be so small that there is no change at all in the ADC output. Hence the measurement resolution of an individual output sample is very coarse. Resolution may be improved however by averaging many such samples. For example 256 samples of 1-bit resolution can average to 1 sample of 8-bit resolution, but this is at the expense of reduced response time. This averaging only operates predictably if the spectral power distribution of the interfering noise is known. If it is not, then noise has to be added by the instrument from its own internal noise source to ensure that it dominates. The addition of this noise, which is only needed in demanding signal recovery situations, tends to lengthen the response time for a given measurement accuracy compared to an analog type of instrument.

4.5.4 Low-pass Filter and Output Amplifier

As mentioned earlier, the purpose of the output filter is to remove the AC components from the desired DC output. Practical instruments employ a wide range of output filter types, implemented either as analog circuits or in digital signal processors. Most usually, however, these are equivalent to one or more stages of simple single-pole “RC” type filters, which exhibit the classic 6 dB/octave roll-off with increasing frequency. There is usually also some form of output amplifier, which may be either a DC-coupled analog circuit or a digital multiplier. The use of this amplifier, in conjunction with the input amplifier, allows the unit to handle a range of signal inputs. When there is little accompanying noise, the input amplifier can be operated at high gain without

overloading the PSD, in which case little, if any, gain is needed at the output. In the case of signals buried in very large noise voltages, the reverse is the case.

4.5.5 Output

The output from a lock-in amplifier was traditionally a DC voltage which was usually displayed on an analog panel meter. Nowadays, especially when the instruments are used under computer control, the output is more commonly a digital number although the analog DC voltage signal is usually provided as well. Units using an analog form of phase-sensitive detector use an ADC to generate their digital output, whereas digital multiplying lock-in amplifiers use a digital to analog converter (DAC) to generate the analog output.

4.5.6 Single Phase and Dual Phase

The discussion above is based around a single-phase instrument. A development of this is the dual-phase lock-in amplifier, which is not, as some people think, a dual channel unit. Rather it incorporates a second phase-sensitive detector, which is fed with the same signal input as the first but which is driven by a reference signal that is phase-shifted by 90 degrees. This second detector is followed by a second output filter and amplifier, and is usually referred to as the "Y" output channel. The original output being referred to as the "X" channel. An advantage of the dual-phase unit is that if the signal channel phase changes (but not its amplitude) then although the output from one detector will decrease, that from the second increases. It can be shown, however, that the vector magnitude, R , remains constant, where: $R = \sqrt{(X^2 + Y^2)}$ Hence if the lock-in amplifier is set to display R , changes in the signal phase will not affect the reading and the instrument does not require the

adjustment of the reference phase-shifter circuit. This capability has led to the dual-phase instrument becoming by far the most common type of unit.

4.5.7 Internal Oscillator

All lock-in amplifiers use some form of oscillator within their reference circuits. Many units however also have a separate internal oscillator which can be used to generate an electrical stimulus for the experiment, usually with user-adjustable frequency and amplitude.

4.6 The PLL

A PLL is a circuit which causes a particular system to track with another one. More precisely, a PLL is a circuit, synchronizing an output signal (generated by oscillator) with a reference or input signal in frequency as well as in phase. In the synchronized – often called ‘locked’- state, the phase error between the oscillator’s output signal and the reference signal is zero or very small.

If a phase error builds up, a control mechanism acts on the oscillator in such a way that the phase error is again reduced to a minimum. In such a control system the phase of the output signal is actually locked to the phase of the reference signal. This is why it is referred to as a Phase- Locked Loop

4.6.1 Operating Principles of the PLL

The operating principle is explained by the example of the linear PLL (LPLL). There exist other types of PLLs e.g., digital PLLs (DPLL), all –digital PLLs (ADPLL) and software PLLs (SPLL). The PLL consists of three basic functional blocks.

1. A voltage-controlled oscillator (VCO)
2. A phase detector (PD)

3. A loop filter (LF).

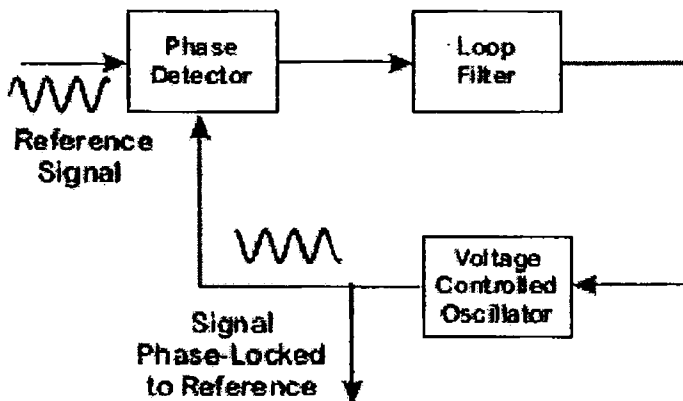


Fig 4.4 Block diagram of PLL

The signals of interest within the PLL circuit are defined as follows :

- The reference (or input) signal $u_1(t)$
- The angular frequency ω_1 of the reference signal
- The output signal $u_2(t)$ of the VCO
- The angular frequency ω_2 of the output signal
- The output signal $u_d(t)$ of the phase detector
- The output signal $u_f(t)$ of the loop filter
- The phase error θ_e , defined as the phase difference between signals $u_1(t)$ and $u_2(t)$

The operation of the three functional blocks is shown in Fig. 4.4. The VCO oscillates at an angular frequency ω_2 , which is determined by the output signal u_f of the loop filter. The angular frequency ω_2 is given by

$$\omega_2(t) = \omega_0 + K_0 u_f(t) \quad 4.5$$

Where ω_0 is the centre (angular) frequency of the VCO and K_0 is the VCO gain in $s^{-1} V^{-1}$.

The Phase Detector (PD) – also referred to as phase comparator- compares the phase of the output signal with the phase of the reference signal and develops an output signal $u_d(t)$ which is approximately proportional to the phase error θ_{er} at least within a limited range of the latter

$$u_d(t) = K_d \theta_e \quad 4.6$$

Here K_d represents the gain of the PD, the physical unit of K_d is volts. The output signal $u_d(t)$ of the PD consists of a dc component and a superimposed ac component. The latter is undesired; hence it is cancelled by the loop filter. In most cases a first-order, low-pass filter is used.

First assume that the angular frequency of the input signal $u_1(t)$ is equal to the centre frequency ω_0 . The VCO then operates at its center frequency ω_0 and the phase error θ_e is zero. If θ_e is zero, the output signal u_d of the PD must also be zero. Consequently the output signal of the loop filter u_f will also be zero. This is the condition that permits the VCO to operate at its center frequency.

If the phase error θ_e were not zero initially, the PD would develop a nonzero output signal u_d . After some delay the loop filter would also produce a finite

signal u_f . This would cause the VCO to change its operating frequency in such a way that the phase error finally vanishes.

Assume now that the frequency of the input signal is changed suddenly at time t_0 by the amount $\Delta\omega$. The phase of the input signal then starts leading the phase of the output signal. A phase error is built up and increases with time. The PD develops a signal $u_d(t)$ which also rises. This causes the VCO to increase its frequency. The phase error becomes smaller now, and after some settling time the VCO will oscillate at a frequency that is exactly the frequency of the input signal. Depending on the type of loop filter used, the final phase error will be reduced to a finite value.

The VCO now operates at a frequency which is greater than the original frequency by an amount $\Delta\omega$. This will force the signal at a final value of $u_f = \Delta\omega/K_0$. If the center frequency of the input signal is frequency modulated by an arbitrary low frequency signal, then the output signal of the loop filter is the demodulated signal. The PLL can consequently be used as an (FM) detector.

One of the most intriguing capabilities of the PLL is its ability to suppress noise superimposed on its input signal. Suppose that the input signal of the PLL is buried in noise. The PD tries to measure the phase error between input and output signals. The noise at the input causes the zero crossings of the input signal $u_1(t)$ to be advanced or delayed in a stochastic manner, this causes the PD output signal $u_d(t)$ to jitter around the average value and the VCO will operate in such a way that the phase of the signal $u_2(t)$ is equal to the average phase of the input $u_1(t)$. Therefore, it can be stated that the PLL is able to detect a signal that is buried in noise.

4.6.2 Classification of PLL types

The very first phase locked loops (PLL) were implemented as early as 1962 by Bell Laboratories [4.1]. The PLL found broader industrial applications only when it became available as an integrated circuit. The first PLL ICs appeared around 1965 and were purely analog devices. An analog multiplier (four-quadrant multiplier) was used as the phase detector, the loop filter was built from a passive or active RC filter, and the well-known voltage-controlled oscillator (VCO) was used to generate the output signal of the PLL. This type of PLL is referred to as the linear PLL (LPLL) today. In the following years the PLL drifted slowly but steadily into digital territory, the very first digital PLL (DPLL) which appeared around 1970 was in effect a hybrid device: only the phase detector was built from a digital circuit, e.g., from an EXOR gate or a JK – flip-flop, but the remaining blocks still are analog. A few years later, the “all –digital” PLL (ADPLL) was invented. The ADPLL is exclusively built from digital function blocks, hence does not contain any passive components like resistors and capacitors. PLLs can also be implemented “by software” In this case, the function of the PLL is no longer performed by a piece of specialized hardware, but rather by a computer program. This is referred to as SPLL.

Because the software PLL is usually implemented by a micro controller, or digital signal processor (DSP) it is generally considered to be an “all-digital” vehicle. The SPLL can be programmed to perform like an LPLL, a DPLL, or an ADPLL, so the SPLL is , the most universal type of PLL. One would

expect that the SPLL has replaced its hardware counterparts in many cases, but this is not the case. The computer algorithm which performs the PLL function must be executed at least once in every period of the input signal of the PLL. This severely limits the range of frequencies which can be covered by the SPLL.

4.6.3 The SPLL

In the age of microcontrollers and digital signal processors (DSP) it is an obvious idea to implement a PLL system by software. When doing so, the functions of the PLL are performed by a computer program.

4.6.3.1 The Hardware-Software Trade-off

The designer realizing software PLL trades electronic components for microseconds of computation time. As the parts count for hardware PLL increases with the level of sophistication, the number of computer instructions rises with the complexity of the required PLL algorithms.

Of course the SPLL can compete with a hardware solution only if the required algorithms are executing fast enough on the hardware platform which is used to run the program. If a given algorithm performs too slowly on a relatively cheap microcontroller the designer is forced to resort to more powerful hardware (e.g., a DSP), the price trade-off also comes into play. The high speed and low cost of available PLL ICs makes it difficult for the SPLL to compete with its hardware counterpart. Nevertheless, SPLLs can offer particular advantages, especially when computing power is already available.

When comparing SPLLS with hardware PLLs, we should recognize first that an LPLL or a DPLL actually is an analog computer which continuously performs some arithmetic operations. When a computer algorithm has to take over that job, it must replace this continuous operation by a discrete-time process. From the previous discussion of hardware PLLs, it is clear that every signal of such a system contains a fundamental frequency, which can be equal to its reference frequency f_1 or twice that value. According to the sampling theorem, the algorithm of the SPLL must be executed two or even four times in each cycle of the reference signal. If the reference frequency is 100 kHz, for example, the algorithm must execute 200,000 times per second in the most favorable case, which leaves not more than 5 μ s for one pass-through.

Today's microcontrollers easily work with clock frequencies of 50 MHz or more, which says that one machine cycle is 20 ns or less. For most microcontrollers, however, one instruction needs more often much more than one machine cycle to execute. There is a risk, therefore, that the microcontrollers on the lower end of the price scale fail to deliver the required computational throughput.

Using DSPs instead brings us a big step forward, because they not only are fast with respect to clock frequency but offer Harvard-Plus and pipeline architecture. Harvard architecture means that the DSP has physically separated data and program memories; hence can fetch instructions and data within the same machine cycle. In even more sophisticated DSPs, the machine can fetch one instruction and several data words at the same time. The term "pipeline" implies that the arithmetic and logic units of the machine are fully

decoupled, so that the DSP chip is able, for example, to perform one instruction fetch, some operand fetches (data fetches), one or more floating-point additions, one or more floating point multiplications, one or more instructions decodings, one or more register-to-register operations, and perhaps even more *in one single machine cycle*. This greatly enhances computational throughput but results in higher cost, of course.

In the next section we discuss the steps required to check the feasibility and economy of an SPLL realization.

4.6.3.1 Feasibility of an SPLL Design

An SPLL design offers the most degrees of freedom available in any one PLL design, because the SPLL can be tailored to perform similar to an LPLL or a DPLL or to execute a function which none of these hardware variants is able to do. To check whether a software implementation can economically be justified, we recommend going through the steps described in the following.

Step 1. Definition of the SPLL algorithm. The SPLL design procedure should start with the formal presentation of the algorithm(s) to be performed by the SPLL. Examples of such algorithms will be given in Sec. 5.3. For the moment it is sufficient to write down these algorithms in symbolic form, i.e., by algebraic and/or logic equations. Structograms are ideally suited to define the sequence of the operations, to describe conditional or unconditional program branchings, to describe loops which are repeatedly run through, and the like. Examples of structograms are also given in next sections

Step 2. Definition of the language. Having defined the algorithms, the language which will be used to encode them should be defined, at least tentatively. The programming effort is minimized when a high-level language such as C, FORTRAN, or PASCAL is used. Other frequently used languages are FORTH, BASIC, PL/M, and ADA. If the program is required to finally run on a microcontroller, a language must be chosen for which a compiler is available. Manufacturers of microcontroller or software houses mostly provide compilers for C and PL/M. When the compiled assembly-language program is available, the time required to execute it can be estimated. It should be noted that different assembler instructions may require different execution times.

Not every compiler is able to generate a time-efficient assembly code. If it is necessary to use a DSP, this point is even more important. When the DSP makes use of pipeline techniques the compiler must generate parallel assembly code, i.e., an assembler program where a number of different instructions are executed in any one instruction. In cases where efficient compiler programs are not available, the software designer could even be forced to write the program immediately in assembly code. With parallel-computing DSPs this is not a simple task, however. Some manufacturers of DSP chips offer signal processing libraries written in assembly code, which can be used to perform most elementary signal-processing tasks, e.g., digital filtering and the like.

Whatever language is used, the assembly code must be available to get an estimate of the approximate execution time of the algorithm(s).

Step 3. Estimation of real-time bandwidth. Having estimated the program execution time, the designer must calculate the real-time bandwidth of the SPLL system. If the execution time of the full SPLL algorithm is 50 μ s, for

example, and two passes are required in one cycle of the reference signal, at least 100 μ s of computation time is needed in one reference period. Probably the microcontroller or whatever hardware is used will need some more time for timekeeping, input/ output operations, and the like; the real-time bandwidth is likely to fall well below 10 kHz in this example.

Step 4. Real-time testing. To check if the system performs as planned, the designer will have to implement a breadboard and test its system in "real time." Only such a test can make sure that the real system is not even slower than the designer imagines.

4.7 SPLL. Examples

Because every known LPLL, DPLL, or ADPLL system can be implemented by software, the number of variants becomes virtually unlimited. We therefore restrict ourselves to a few examples. The required algorithms for the SPLL will be described in great detail, so the reader should be able to adopt the methods to other SPLL realizations. The PLL simulation program delivered with the disk is a good example for SPLLs, because it demonstrates the ability of software to implement a great number of different linear and digital PLL configurations. We should be aware, however, that the simulation program does not represent a real time system, since it does not work with real signals nor does it execute the algorithms in real time. Nevertheless, it uses a great deal of the algorithms described in the following sections

An LPLL like SPLL

An SPLL algorithm which performs similar to a hardware LPLL is described. To derive the required SPLL algorithm, a signal flow diagram which shows the arithmetic operations within the loop is shown (Fig. 5.1). The input signal u_1 is supposed to be an arbitrary analog signal e.g., a sine wave. It is periodically sampled, with the sampling $f_s = 1/T$ by an analog-to-digital converter (ADC), where T is the sampling interval. Thus samples are taken at times $t = 0, T, 2T, \dots, nT$. $u_1(n)$ is the simplified notation for the input signal sampled at time $t = nT$, i.e., $u_1(n) = u_1(nT)$.

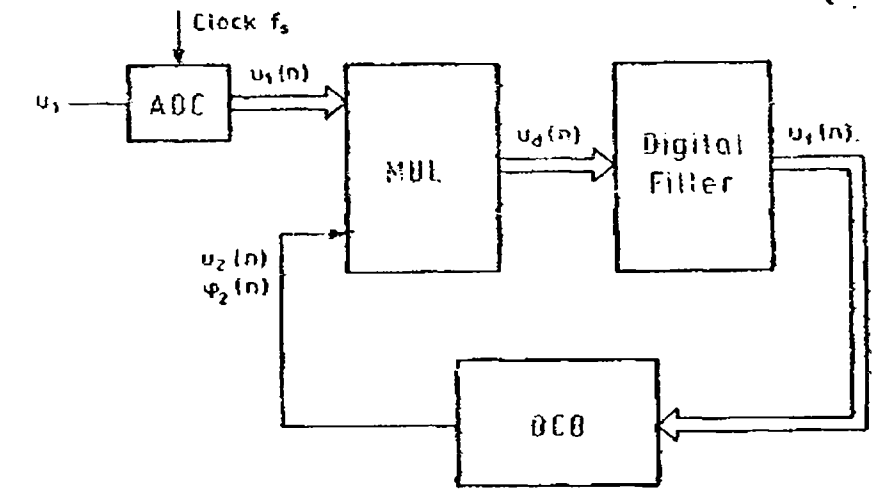


Fig 4.5 Block diagram showing the arithmetic operations to be performed by an SPLL

All other signals of the SPLL are sampled signals, too, and must be calculated at the sampling instants $t = 0, T, 2T, \dots, nT$. Consequently, all functional blocks of the signal flow diagram are working synchronously with the ADC

clock.

In Fig. 4.5 the signals shown by double lines are word signals. The output signal of the DCO however, is a bit signal and is therefore represented by a single line.

There are three functional blocks in the signal flow diagram, a digital multiplier, a digital filter, and a DCO. The multiplier is used as phase detector and corresponds exactly with the already known Nyquist rate PD discussed earlier. Its output signal is denoted $u_d(n)$. The digital filter serves as loop filter, its output signal is $u_f(n)$. Finally, the DCO is supposed to generate a square-wave output signal $u_2(t)$, which is known only at the sampling instants. The sampled, DCO output signal is denoted $u_2(n)$. As seen, the DCO is not able to compute $u_2(t)$ directly; this signal must, rather be calculated indirectly from the phase $\Phi_2(t)$ of the DCO. If a VCO were used instead of the DCO, its instantaneous output angular frequency would be given by

$$\omega_2(t) = \omega_0 + K_0 u_f(t) \quad 4.5$$

And the continuous output $u_2(t)$ is given by

$$u_2(t) = w[\omega_2(t)t] \quad 4.6$$

where w denotes the Walsh function. The total phase $\Phi_2(t)$ of the VCO output signal then would be

$$\phi_2(t) = \int \omega_2(t) dt = \omega_0 t + K_0 \int u_f dt \quad 4.7$$

Here only the differential phase $\theta_2(t)$, which corresponds to the second term only on the right side of Eq. (4.7) is dealt with. The total phase $\Phi_2(t)$ is used to compute the instantaneous value of the DCO output signal $u_2(t)$. If one assigns the values +1 and -1 to the square-wave signal, it follows from the definition of

the Walsh function that $u_2(t)$ is, +1, when the phase $\Phi_2(t)$ is either in the interval $0 \leq \Phi_2 < \pi$ or in the interval $2\pi \leq \Phi_2 < 3\pi$ etc. In all other cases, $u_2 = -1$. This computation scheme is adapted to the time-discrete case we are dealing with. When it is known that the digital filter output signal $u_f(n)$ at sampling instant $t = nT$ and assuming furthermore that it stays constant during the time interval $nT \leq t < (n+1)T$, the total phase of the DCO output signal will change by an amount

$$\Delta\phi_2 = [\omega_0 + K_0 u_f(n)]T \quad 4.8$$

in that interval. If the phase $\Phi_2(n)$ at sampling instant $t = nT$ were known, the total phase $\Phi_2(n+1)$ can be extrapolated at sampling instant $t = (n+1)T$ from

$$\phi_2(n+1) = \phi_2(n) + [\omega_0 + K_0 u_f(n)]T \quad 4.9$$

This computation is possible because the total phase can be initialized with $\Phi_2(0) = 0$ before the SPLL algorithm is started. Hence one can extrapolate $\Phi_2(1)$ at time $t = 0 + T$, $\Phi_2(2)$ at $t = 1 + T$, etc. Given $u_2(n+1)$ we can also extrapolate the value of $u_2(n+1)$ at $t = (n+1)T$,

$$\begin{aligned} u_2(n+1) &= 1 \text{ if } 2k\pi \leq \Phi_2(n+1) < (2k+1)\pi \text{ or} \\ u_2(n+1) &= -1 \text{ if } (2k-1)\pi \leq \Phi_2(n+1) < 2k\pi, \text{ k = integer} \end{aligned} \quad 4.10$$

The signals of the SPLL are depicted in Fig. 4.6. The dashed lines represent continuous signals. The sampled signals are plotted as dots. Only the continuous signal $u_f(t)$ really exists; all others are only fictive. The required algorithm is easily derived from these waveforms. At a given sampling instant $t = nT$, the output signal $u_d(n)$ of the multiplier has to be computed by

$$u_d(n) = K_d u_f(n) u_2(n) \quad 4.11$$

where K_d is the gain of the phase detector. Given $u_d(n)$, a new sample of $u_f(n)$

must be computed; the corresponding filter algorithm will be given below. Given $u_1(n)$, the value of $\Phi_2(n + 1)$ at the next sampling instant is *extrapolated*. This enables us to extrapolate $u_2(n + 1)$ also. This value must be known, because $u_2(n)$ is needed in the following sampling instant to compute the next value of $u_d(n)$.

The SPLL algorithm is now represented symbolically in the structogram of Fig. 4.7. When the algorithm is started, initial values are assigned to all relevant variables. The program enters an endless cycle thereafter; i.e., the algorithm within the box is repeatedly executed, until the system is halted or switched off. It is assumed that the clock signal periodically generates interrupts in the microcontroller or whatever hardware is used. Thus interrupt requests show up at time instants $t = T, 2T, \dots, nT$. As soon as the interrupt is recognized by the hardware, the SPLL algorithm is executed. It starts with the acquisition of a sample of the input signal $u_1(t)$. The next three statements of the structogram correspond with the computation scheme already described. Finally when all the variables of the SPLL have been updated, they must be delayed (or shifted in time). The variable $u_d(n-1)$ is overwritten by the value $u_d(n)$, which means that the "new" value of $u_d(n)$ computed in this cycle will be the "old" value $u_d(n - 1)$ in the next cycle. The same holds true for all other variables.

Knowing what has to be calculated in every step, we can develop the algorithm in mathematical terms. The full procedure is listed in Fig. 4.8. First all relevant variables are initialized with 0. Depending on the particular application, other values can be appropriate. The operation of the multiplier is trivial.

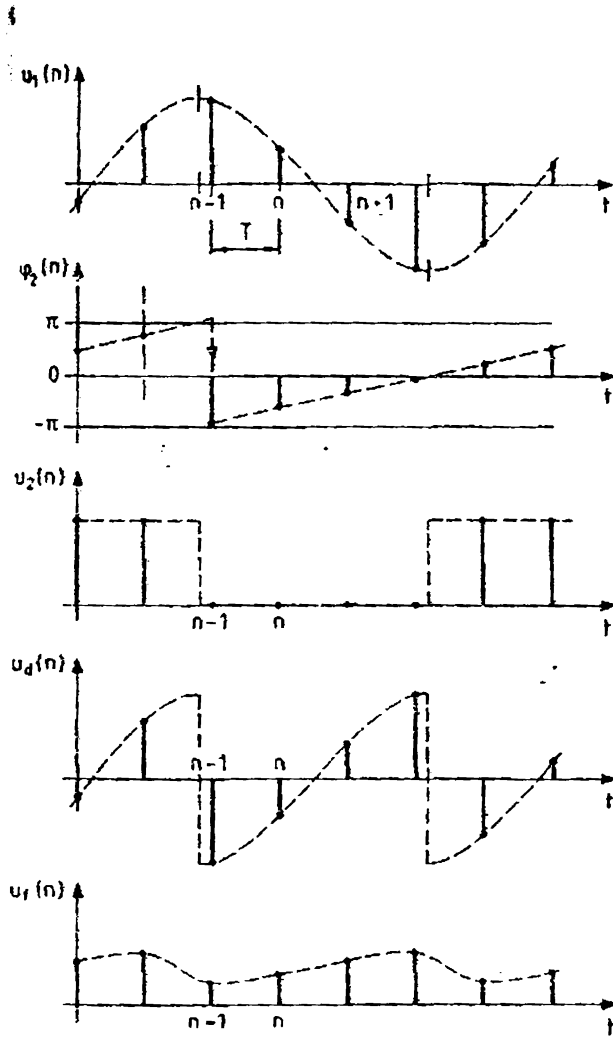


Figure 4.6 Plot of the signals which have to be calculated by the SPLL algorithm.

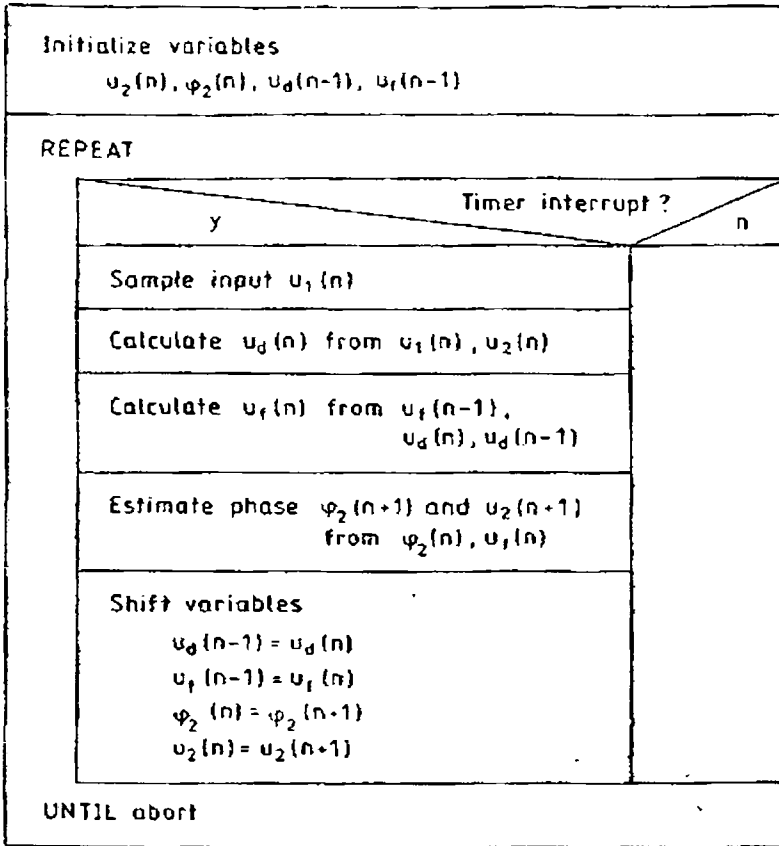


Fig 4.7 Flowchart of SPLL implementation- level 1

The next statement is the digital filter algorithm.

$$u_f(n) = -a_1 u_f(n-1) + b_0 u_d(n) + b_1 u_d(n-1) \tag{4.12}$$

This is the recursion of a first-order digital filter. As pointed out earlier an analog filter is described by its transfer function

$$F(s) = \frac{U_f(s)}{U_d(s)} \tag{4.13}$$

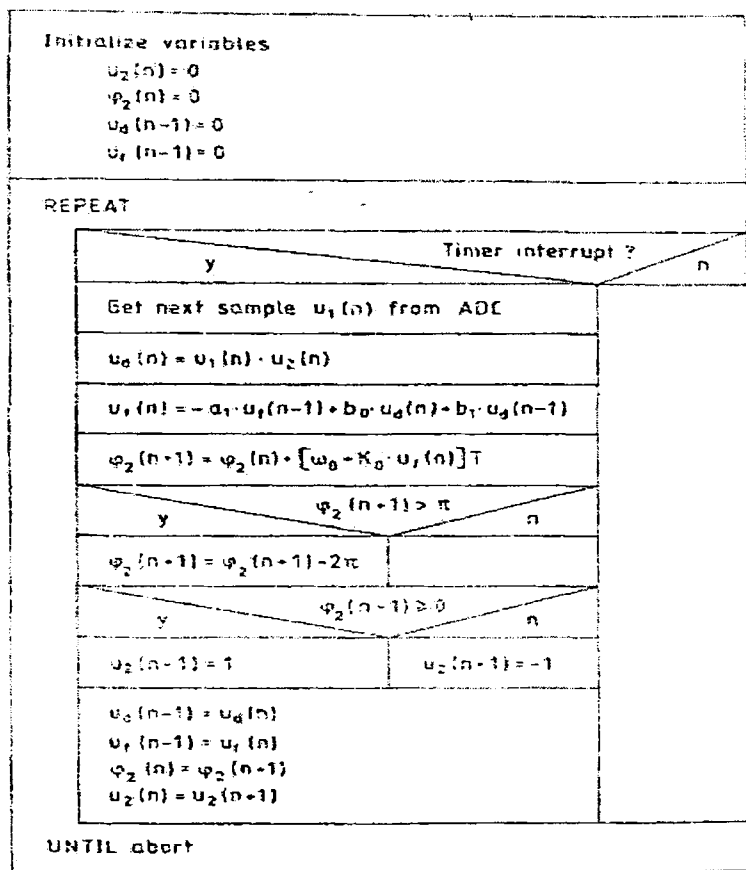


Fig 4.8 Flowchart of SPLL implementation-level 2

where s is the Laplace operator and $U_f(s)$ and $U_d(s)$ are the Laplace transforms of the continuous signals $u_f(t)$ and $u_d(t)$, respectively. To get a digital filter performing nearly the same function $F(s)$ is usually transformed into the z -domain.

$$F(z) = \frac{U_f(z)}{U_d(z)} \tag{4.14}$$

There are a number of transforms which can be used to convert $F(s)$ into $F(z)$.

The most often used is called *bilinear z-transform*. Before the digital filter is designed, the (fictive) analog filter is defined. Because the active PI filter offers best PLL performance, $F(s)$ is assumed to be the transfer function of the active PI filter. Using the bilinear z-transform,

$$F(z) = \frac{b_0 + b_1 z^{-1}}{1 + a_1 z^{-1}} \quad 4.15$$

where the filter coefficients are given by

$$a_1 = -1$$

$$b_0 = \frac{T}{2\tau_1} \left[1 + \frac{1}{\tan(T/2\tau_2)} \right]$$

$$b_1 = \frac{T}{2\tau_1} \left[1 - \frac{1}{\tan(T/2\tau_2)} \right]$$

and T is the sampling interval. Transforming back into time domain, we get the recursion

$$u_f(n) = -a_1 u_f(n) + b_0 u_d(n) + b_1 u_d(n-1) \quad 4.16$$

which is also listed in the structogram of Fig. 4.8. Using Eq. (4.9) the total phase of the DCO output signal at the next sampling instant will be

$$\phi_2(n+1) = \phi_2(n) + [\omega_0 + K_0 u_f(n)]T \quad 4.17$$

When the algorithm is executed over an extended period of time, the values of $\Phi_2(n+1)$ will become very large and could soon exceed the allowable range of a floating number in the processor used. To avoid arithmetic overflow Φ_2 is limited to the range $-\pi \leq \Phi_2 < \pi$. Whenever the computed value of $\Phi_2(n+1)$ exceeds π , 2π is subtracted to confine it to that range. Now the value of

$u_2(n + 1)$ is easily computed by checking the sign of the range-limited total phase. If $\Phi_2(n + 1) \geq 0$, $u_2(n + 1) = 1$; otherwise $u_2(n + 1) = -1$. Finally, the calculated values of $u_d(n)$, etc., are delayed by one sampling interval, i.e. $u_d(n - 1) = u_d(n)$ etc.

When simulating the LPLL on the PC, the sampling rate f_s for this SPLL algorithm must be chosen at least 4 times the reference frequency in order to avoid aliasing of signal spectra.

A DPLL-like SPLL

When the input signal u_1 of a PLL is a binary signal, it is more adequate to implement an SPLL which performs like a DPLL. An algorithm performing like the DPLL using the phase-frequency detector and a passive lag filter is developed. Though the mathematical and logical operations within such a DPLL seem simpler compared with an LPLL, it turns out that the algorithm for the corresponding SPLL becomes much more complicated.

The required functions are represented by a signal flow diagram (Fig. 4.9). It essentially consists of three functional blocks, a *PF*D algorithm, a digital filter, and a DCO. The digital filter is required to operate like the passive lag filter in a DPLL. Before going into details, we consider the signals of this SPLL (Fig. 4.10). The only signal which physically exists—at least at the beginning—is the input signal $u_1(t)$, a square whose frequency can vary within the frequency range of the DCO. The (fictive) output signal $u_2(t)$ of the PLL would be a square wave, too. As we know from Sec. 3.1, the logic state Q of the *PF*D depends on the positive edges of these two signals (or from the negative edges, whatever definition is made). When the PLL has settled to a steady state, the signals $u_1(t)$ and $u_2(t)$ are nearly in phase. The output Q of the *PF*D is then in

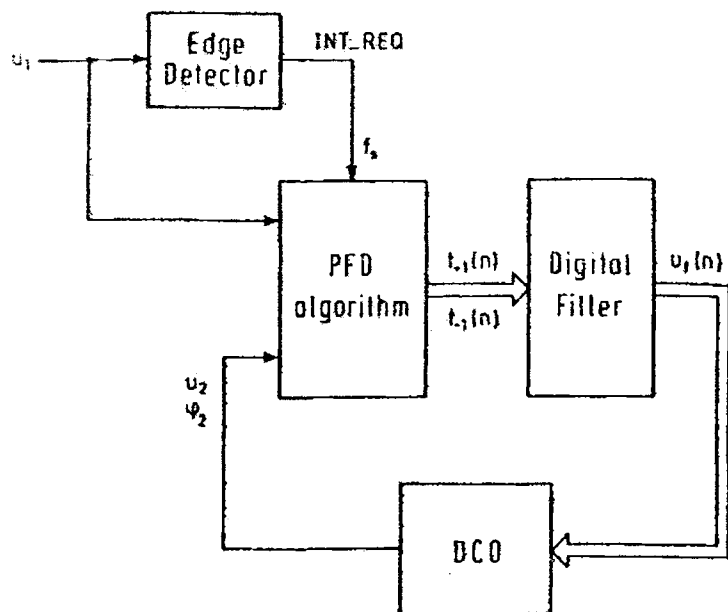


Figure 4.9 Block diagram showing the arithmetic and logic operations to be performed by an SPPLL whose performance is similar to the DPLL.

the 0 state most of the time. Should the output frequency of the DCO drift away, the PFD would generate correction pulses; i.e., Q would become +1 or -1 for a very short time. The width of the correction pulses is mostly less than $1/1000$ of one period of the reference signal. If we tried to detect the edges of $u_1(t)$ and $u_2(t)$ by sampling these signals, the sampling frequency would have to be at least 1000 times the reference frequency, which is highly unrealistic. Another scheme must be used, therefore, to detect the instants where the state of u_1 and u_2 is changing. Because we need to know the times where u_1 and u_2 are switching from low to high, the (positive and negative) edges of $u_1(t)$ are used

to generate interrupt requests to the computer; refer to the signal INT_REQ in Figs. 4.9 and 4.10. The computer is supposed to have a timer/counter chip such as the Intel 8253 or the AMD 9513. As soon as the interrupt is recognized, a "time stamp" is taken; i.e., the time where the interrupt occurred is stored. The instants where interrupts have been detected are called $t(0)$, $t(1)$, . . . , $t(n)$, Three of them are marked on top of Fig. 4.10. Before the SPLL algorithm can be discussed, a number of signals have to be defined: refer to Fig. 4.10. $u_1(n)$ is the sampled version of the continuous reference signal $u_1(t)$ *immediately after occurrence of the interrupt request*. At time $t(n - 1)$, e.g., $u_1(n) = 1$, and at time $t(n)$, $u_1(n) = 0$. $\Phi_2(t)$ is the (fictive) continuous phase of the DCO output signal. $\Phi_2(n)$ is the sampled version of $\Phi_2(t)$. Of course, the samples are also taken at the instants where an interrupt occurred. $u_2(t)$ is the (fictive) continuous output signal of the DCO. It will be calculated from the phase $\Phi_2(t)$. $Q(t)$ is the (fictive) continuous output signal (or state) of the PFD. It can have the values -1, 0, or 1. $Q(n)$ is a sampled version of $Q(t)$ and is defined to be the state of the PFD just *prior to occurrence of the interrupt* at time $t(n)$. For example, $Q(n - 1)$ has the value 0, because $Q(t)$ was in the 0 state before the interrupt at $t = t(n - 1)$ was issued. $T(n)$ is defined to be the time interval between the time of the most recent interrupt $t(n)$ and the time of the preceding interrupt at $t = t(n - 1)$; thus $T(n) = t(n) - t(n - 1)$. When $Q(t)$ is in the +1 state in a fraction of the $T(n)$ interval, the corresponding duration is stored in the variable $t_{+1}(n)$, as shown by the arrow in Fig. 4.10. When $Q(t)$ is in the -1 state in a fraction of the $T(n)$ interval, however, the corresponding duration is stored in the variable $t_{-1}(n)$; this is indicated by another arrow on Fig. 4.10.

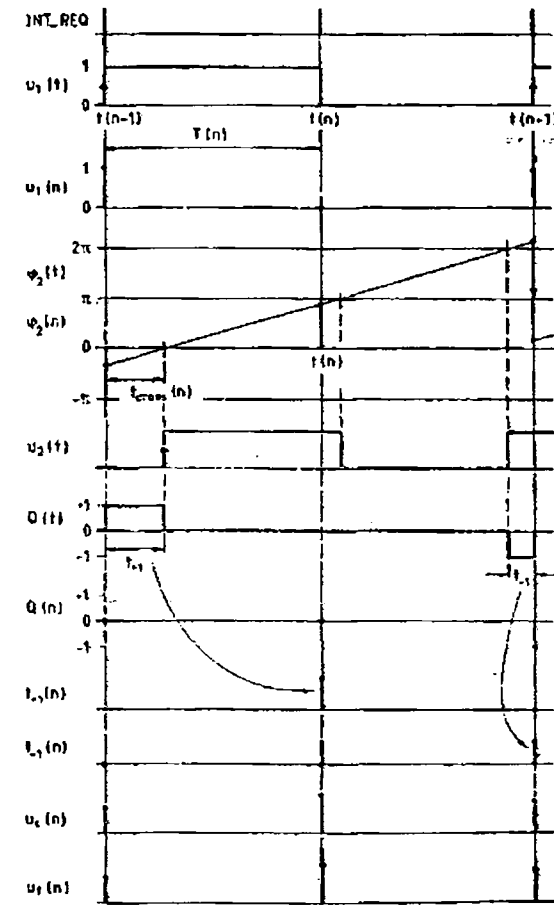


Figure 4.10 Plot of the signals which have to be calculated by the SPLL algorithm

Finally, $u_c(n)$ is used to denote the signal on the (fictive) capacitor C ; $u_f(n)$ is used to denote the sampled output signal of the digital filter in Fig. 5.5. With reference to Fig. 5.6, $u_f(n)$ is nearly identical with $u_c(n)$ but can slightly differ when "current" flows in the (fictive) resistor R_2 .

The enumeration of that large set of variables has been quite cumbersome,

but the elaboration of the algorithms will be even more fatiguing. The structogram of Fig. 4.11 shows what has to be done on every interrupt service.

The signals appearing in the algorithm are shown in Fig. 4.10

The uppermost portion of the SPLL algorithm is trivial and lists the initialization of some variables. As in the previous example, the program then enters an endless loop, where it first waits for the next interrupt. When the interrupt has been detected, the time lapsed since the last interrupt is taken, $T(n) = t(n) - t(n - 1)$. Next, the current value of the reference signal $u_1(t)$ is sampled, $u_1(n) = u_1(t)$. This is necessary because one need to know whether we are in the positive or negative half-cycle of the square wave $u_1(t)$. We assume that the current time t is $t(n)$ right now, which corresponds to the second interrupt request shown in the middle of Fig. 4.9. In contrast to the previous SPLL example, the value of the phase $\Phi_2(t)$ is *not known* at that time. The reason for this is simple: At time $t = t(n - 1)$ the value of the digital filter output signal $u_f(n - 1)$ could be calculated, and consequently we also knew the instantaneous (angular) frequency $\omega_2(n - 1)$ of the DCO. But since one did not yet know at time $t = t(n - 1)$ how long the duration of the following half-cycle of $u_1(t)$ would be, one could not extrapolate $\Phi_2(n)$ but had to postpone that until $t=t(n)$. Only now at $t = t(n)$, $\Phi_2(n)$ can be computed from

$$\phi_2(n) = \phi_2(n-1) + [\omega_0 + K_0 u_f(n-1)]T(n) \quad 4.18$$

Note that the phase $\Phi_2(n-1)$ at time $t = t(n-1)$ was known, because the phase of the signal is computed recursively and was initialized with

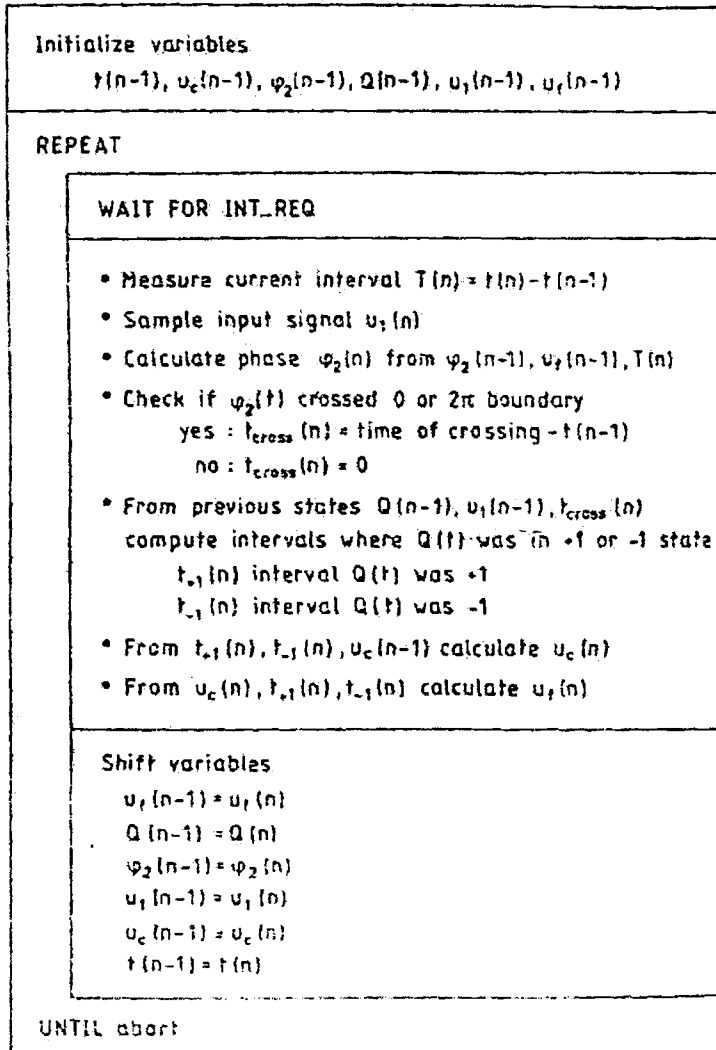


Figure 4.11 Structogram defining the arithmetic and logic operations within the SPLL of Fig 5.5.

$\Phi_2(0) = 0$ at $t = 0$. Next it must be determined whether or not the (fictive) signal $u_2(t)$ showed up a positive edge in the interval $T(n)$. This is the case when the continuous phase signal $\Phi_2(t)$ "crossed" the value 0 or 2π during interval $T(n)$; this is sketched in the waveforms of Fig. 4.10. Positive edges also would occur at phase crossing with $4\pi, 6\pi, \dots$, etc. The total phase is periodically reduced by 2π whenever it becomes larger than 2π . This is necessary to avoid arithmetic overflow in the computer. When the phase crossed such a boundary, the corresponding time [i.e., the time interval from $t(n - 1)$ to the crossing] is stored in the variable $t_{cross}(n)$. When no crossing was detected, $t_{cross}(n)$ is set 0. The algorithm for the computation of $t_{cross}(n)$ is indicated in the structogram of Fig. 4.12. It starts with the "normalization" of the phase signal $\Phi_2(t)$.

The state $Q(t)$ of the PFD can now be computed during the interval $T(n)$. The signal $Q(t)$ depends on a number of other variables. First of all, the state of $Q(n - 1)$ prior to time $t = t(n - 1)$ must be known. If, as sketched in Fig. 5.7, $Q(n - 1)$ was 0 and $u_1(t)$ made a positive transition at $t = t(n - 1)$, $Q(t)$ goes into the + 1 state. When $u_2(t)$ also makes a positive transition thereafter, $Q(t)$ goes back to the 0 state. If $Q(n - 1)$ had already been in the + 1 state at $t = t(n - 1)$, however, it could not have changed its state on the positive edge of $u_1(t)$. The behavior of the PFD is therefore case-sensitive; the algorithm in Fig. 4.13 demonstrates that as many as nine different cases are possible. This algorithm determines the values of $t_{+1}(n)$ and $t_{-1}(n)$ and also computes the state of Q at the end of the $T(n)$ interval.

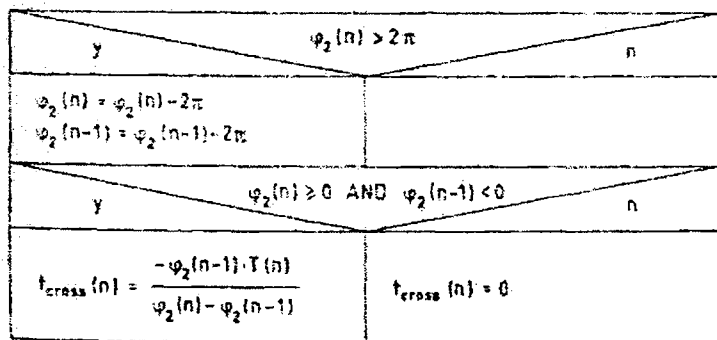


Fig 4.12 Detailed structograms of the algorithms to be performed by the SPLL of Fig. 4.9; Algorithm to determine the variable $t_{\text{cross}}(n)$ (time when output phase $\Phi(t)$ crosses boundary of 0 or 2π)

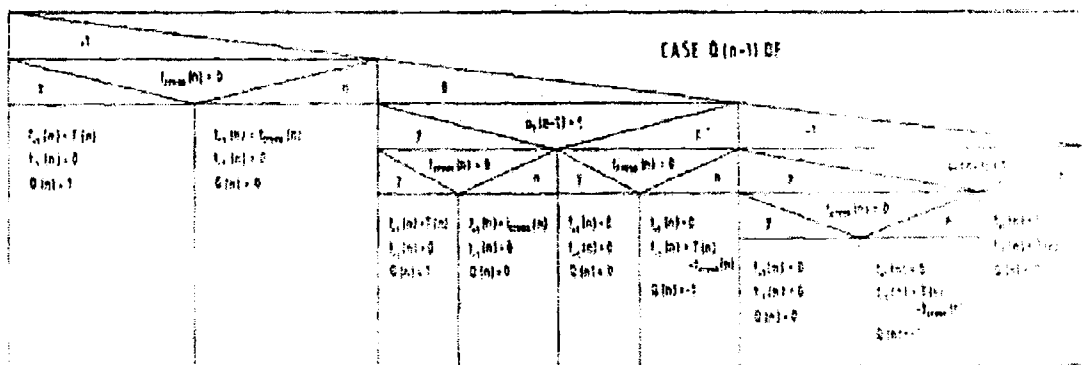


Fig 4.13 Algorithm for the PFD

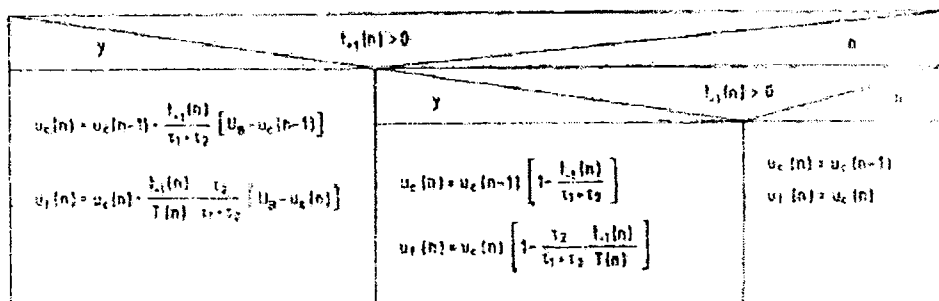


Fig 4.14 Algorithm for the digital filter

This state will be used as initial condition $Q(n - 1)$ in the next interrupt service. When it turns out that $t_{+1}(n)$ is greater than zero, this means that the "supply voltage U_B " must be applied during interval $t_{+1}(n)$ to the RC filter. When $t_{+1}(n)$ is nonzero, however, the "capacitor" C would have to be discharged to ground during the interval $t_{+1}(n)$. The digital filter algorithm in Fig. 4.14 explains how the voltage $u_c(n)$ on capacitor C must be computed from the previous value $u_c(n - 1)$.

If no current flowed into or out of the capacitor C, the output signal $u_f(n)$ would be identical with capacitor voltage $u_c(n)$. In the intervals where current flows, however, $u_f(n)$ can be higher or lower than $u_c(n)$, depending on the polarity of the current. Because $u_f(t)$ is non constant in the interval $t(n - 1) \leq t < t(n)$, we define $u_f(n)$ to be the average of $u_f(t)$ in the interval $t(n - 1) \leq t < t(n)$. This yields the expression listed in Fig. 4.14. When deriving the equations in this algorithm, it was assumed that the duration of a $T(n)$ cycle (half a cycle of the reference signal) is much smaller than the filter time constant τ_1 . Under this

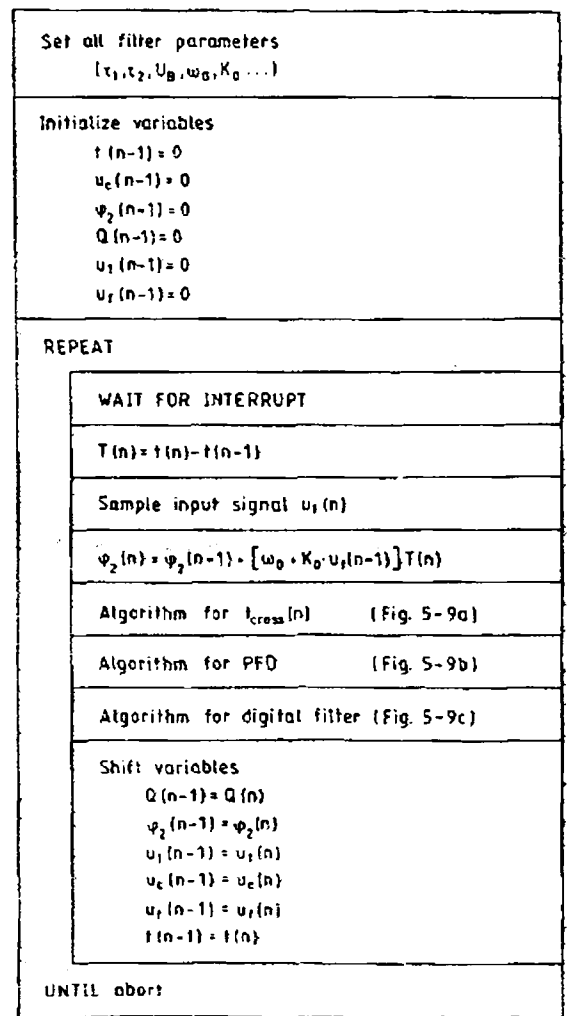


Fig 4.15 Structogram showing the complete algorithm of the SPLL of Fig.4.9

condition, the current flowing into or out from capacitor C remains constant during the charging or discharging intervals. This assumption leads to simpler expressions for $u_c(n)$ and $u_f(n)$.

The algorithm used to compute the filter output $u_f(n)$ differs considerably from

conventional digital filter algorithms. In a classical filter algorithm, the sample $u(n)$ of the output signal is calculated from a number of delayed samples of the output signal and from a number of delayed samples of its input signal. This scheme does not apply, however, to the current example, because the input signal of this circuit is applied only during a *fraction of the sampling interval*. The input is "floating" in the remaining time. Hence the output signal must be calculated like the output of an analog filter, where the input is applied *continuously*.

All computations of one interrupt service are done now. Because most of the computed samples at $t = t(n)$ will be used as starting values in the next interrupt service, they must be shifted in time. This is indicated in the bottom of the structogram of Fig. 4.11. Finally, the structogram of Fig. 4.15 lists the full algorithm in mathematical statements. To avoid overloading the graph, the algorithms for $t_{cross}(n)$ for the PFD and for the digital filter are shown separately (Fig. 4.12-4.14).

4.9 Implementation

We have tried to indigenize the costly imported lock-in-amplifier using a PC and an add-on DSP processor card based on Analog Devices ADSP 2105 with a 12 bit ADC card (M/s Vi Micro Systems, Chennai – VDSP-2105 with VAD - 112 ADC/DAC) and a digital filter design package (Vi-DFDP) which generates the assembly code of ADSP2105. The implementation is described in this section

The generic block of a PC lock-in-amplifier is shown below and the functional blocks are described (Fig 4.16 and Fig 4.17).

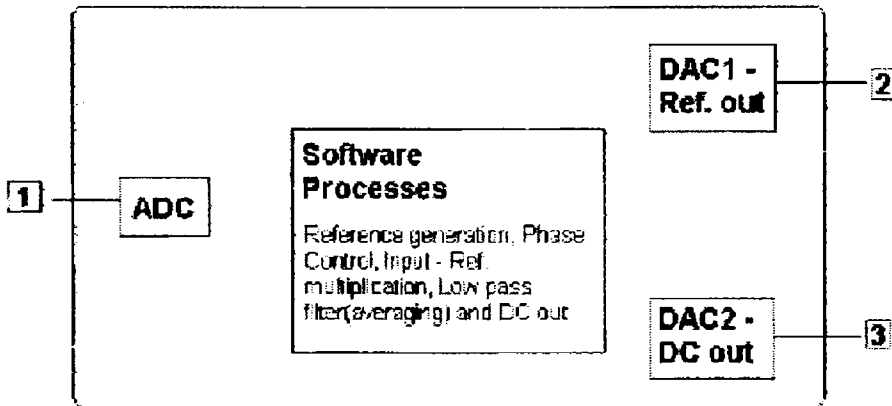


Fig 4.16 Generic PC LIA

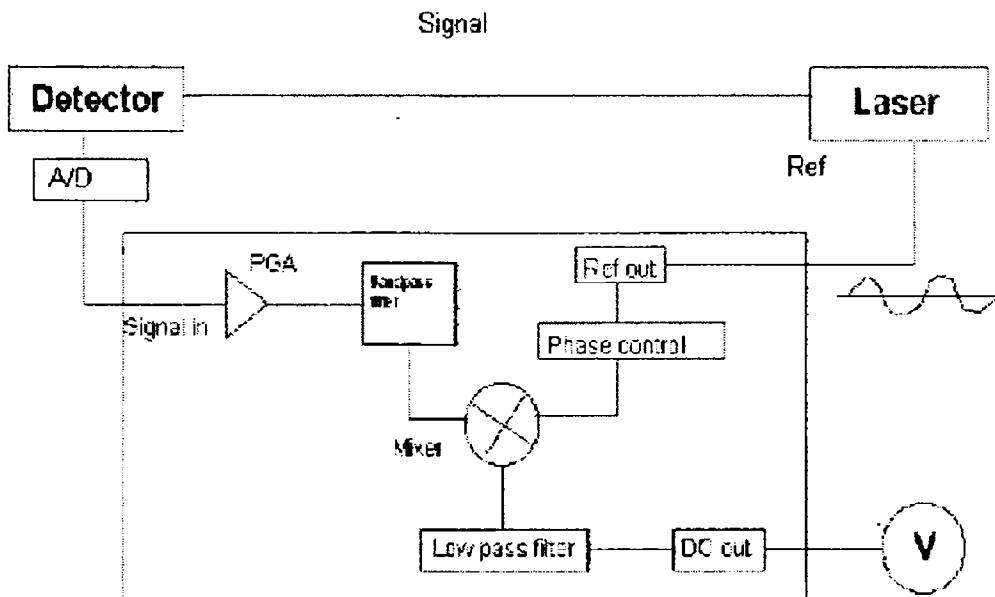


Fig. 4.17 Functional Block diagram

1. PGA – An auto ranging programmable amplifier stage to increase the dynamic range.
2. Bandpass filter – Implemented in software
3. Ref. Out – Reference sine wave output. DAC module

4. Phase Control – To compensate for phase difference between the Reference out and the Signal In. This is implemented in software
5. Mixer - This is implemented in software
6. Low pass filter – This could be implemented in hardware module, but then it requires a high resolution DAC and a filter. It is much simpler to do this using software.
7. DC out – Puts out the DC value proportional to the input signal. This can be implemented using DAC module

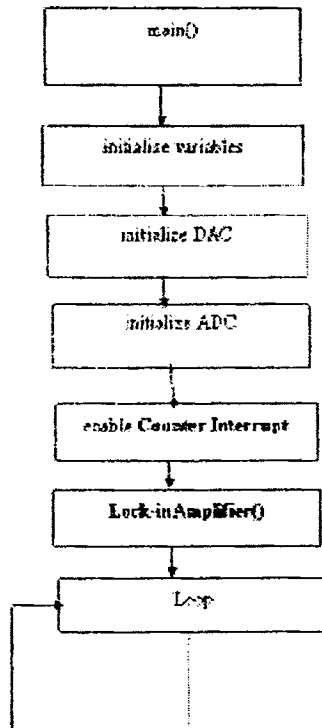


Fig. 4.18 a Main Program Loop

The main program loop takes care of all initializations, enable interrupt and within the interrupt scaling of averager value occurs to fit within the 8-bit DAC2 output to produce the DC output. (Fig. 4.18 a)

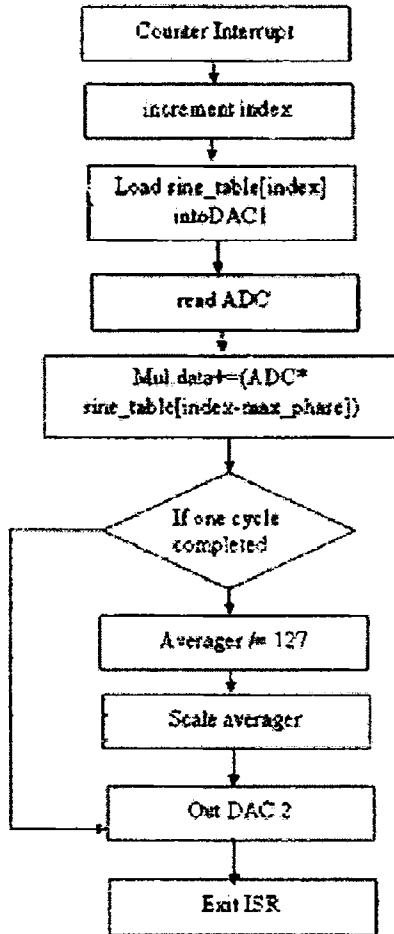
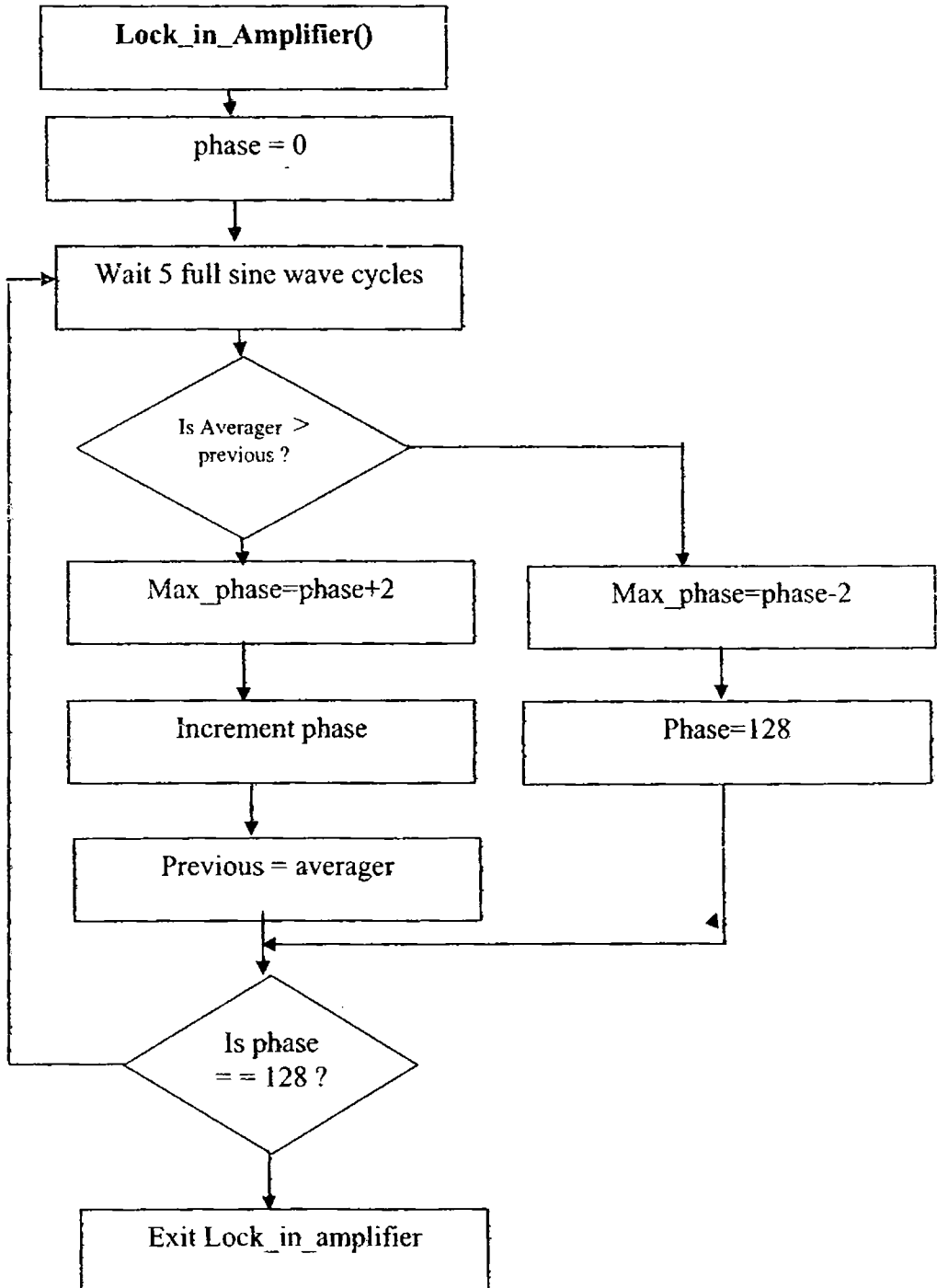


Fig 4.18 b Reference generation

The reference signal is generated using the counter interrupt. The sine wave table value pointed by the 'index' variable is put out of DAC1. The system then reads the ADC, performs the multiplication of the input value and the sine table value pointed by 'index-phase' to correct for delays (Figure 4.18 b)



The 'lock_in_amplifier' routine tries to find the correct phase to lock onto. The interrupt is generating a sine wave and also averaging the input and reference multiplication all the while. The routine scans through the entire sine table array to find the 'index' at which the 'averager' value is at a maximum (Fig 4.18c)

The development of software-driven instrumentation is revolutionizing the extraction of small AC signals that are either partially or completely buried in noise. PC technology improvements continue to push the frontiers of instrumentation. More and more software-based instruments make it easy for engineers and scientists to customize applications to particular needs and leverage new developments from the PC industry. The software implementations of lock-in amplifier described here is a testament of virtual instrumentation that delivers versatile, low-cost digital lock-in amplifiers.

REFERENCES

- 4.1 M. Stachel, "The Lock-in Amplifier: Exploring Noise Reduction and Phase," <http://www.lockin.de/>. An excellent web-based introduction to lock-in detection, complete with Java simulations.
- 4.2 P. Temple, *Am. J. Phys.* **43**(9), 801 (1975).
- 4.3 "About Lock-in Amplifiers" Application Note. Stanford Research Systems, Sunnyvale, CA, 1999. Available at http://www.srsys.com/html/application_notes.html. A functional description of lock-in amplifiers.
- 4.4 *Lock-in Applications Anthology*, ed. Douglas Malchow. EG&G Princeton Applied Research, Princeton, NJ, 1985. A freely available guide to applications of the lock-in analyzer.
- 4.5 D.W. Preston and E.R. Dietz, *The Art of Experimental Physics*. John Wiley & Sons, New York, 1991. Discusses lock-in detection on pp. 367-375.
- 4.6 T H Wilmhurst, *Signal Recovery from noise in electronic instrumentation*, Institute of Physics Publishing, 1990
- 4.7 R E Best, *Phase-Locked Loops-Theory, Design and applications*, McGraw Hill, 1993
- 4.8 M L Meade, *Lock-in Amplifiers: principles and applications*, Peter Peregrinus, UK, 1983

Summary, Conclusion and Scope for future work

A photothermal spectrometer has been set up in the Applied Optics division of Department of Physics, Cochin University of Science and Technology. The salient features of the system include the ability to analyse thin film, powder and polymer samples. The tool has been in use to investigate thermal, optical and transport properties. Binary and ternary semiconducting thin films were analysed for their thermal diffusivities. The system could perform thickness measurements nondestructively. Ion implanted semiconductors are widely studied for the effect of radiation induced defects. We could perform nondestructive imaging of defects using our spectrometer. Dr. M Paulraj, currently a post doctoral scholar at the thin film lab of Dept. of Instrumentation at the Indian Institute of Science, Bangalore was awarded his doctoral degree, (CUSAT, Dept. of Physics, 2005) for his studies on Ar⁺, He⁺ implanted CdS as well as Cu doped CdS. The results reported in his thesis on the above in addition to studies on In₂S₃ and transparent conducting oxide ZnO have been achieved with this spectrometer. Various polymer samples have been easily analysed for their thermal diffusivities. The technique provided ease of analysis not achieved with conventional techniques like TGA and DSC. Industrial application of the tool has also been proved by analyzing defects of welded joints and adhesion of paints. Indigenization of the expensive lock-in-amplifier and automation has been the significant achievement in the course of this dissertation. We are on our way to prove the noise rejection capabilities of our PC LIA.

Summary, Conclusion and Scope for future work

Scope for Future Work

The ability of conventional single-ended photothermal techniques to detect weak inhomogeneities in a given material is mainly limited by two instrumental factors: the signal-to-noise ratio and the amplitude dynamic range. The amplitude level is limited by the output signal baseline, and may be too high to monitor relatively small variations introduced by the presence of weak inhomogeneities. A novel photothermal signal generation methodology, the principle of which can be broadly applied to any technique utilizing a lock-in analyzer demodulation scheme of periodic signal wave forms can be tried out. Unlike the conventional single-ended periodic excitation wave form, which uses a 50% duty-cycle square wave or sinusoidal modulation of the pump laser heating beam, a more complicated periodic modulation wave form can be employed, resulting in the equivalent of differential-signal demodulation. The new wave form takes advantage of the real-time differential action performed by the lock-in amplifier weighing function over the two half periods of the modulated signal. This results in enhanced signal dynamic range due to the efficient suppression of the baseline and a substantial improvement in the SNR. The main features of this technique can be investigated with a theoretical model for an arbitrary repetitive signal wave form and, in particular, for a photothermal signal. The technique known as **lock-in common-mode rejection demodulation signal methodology** can be used as an alternative to the single-ended techniques. This signal generation scheme, when coupled to a photothermal detection system is, in principle, capable of detecting very weak inhomogeneities in materials that are not possible to be detected with conventional techniques.

Summary, Conclusion and Scope for future work

The depth profile of thermally inhomogeneous samples can be estimated from **combined laterally and frequency resolved photothermal measurements**. The mathematical procedure of **data inversion** makes use of the quasianalytical solution of the forward problem. Introducing an appropriately chosen grid of depth coordinates the Hankel transform of the surface temperature can be expressed by a continuous fraction formula. This enables the usage of the effective conjugated gradient technique to retrieve the thermal depth profiles by minimization of the objective function. Making use of the *a priori* information about the inhomogeneous sample we chose an appropriate Tikhonov's stabilizer function and by this way remarkably improved the iteration procedure. The success of this method consists of a drastic reduction in computation time and in a better approximation of the searched profiles.

Or thermal conductivity depth profiles of thermally inhomogeneous materials may be retrieved from the time dependence of the surface temperature after a flash illumination. A **neural network** method, which is trained to recognize the correlation between depth profiles and the surface temperature on the basis of many examples, can be employed.

Inverse problems on different kinds of materials have been identified, classified, and solved. A first classification has been done according to the type of depth profile: the physical quantity to be reconstructed is the optical absorption in the problems of type I, the thermal effusivity for type II, and both of them for type III. Another classification may be done depending on the time scale of the pump beam heating (frequency scan, time scan), or on its geometrical symmetry (one- or three-dimensional). Two different approaches,

Summary, Conclusion and Scope for future work

the **genetic algorithms (GA)** and the **thermal wave backscattering (TWBS)** can be applied to several kinds of photothermal depth profiling problems: The two approaches are based on different mechanisms and exhibit obviously different features. GA may be implemented on the exact heat diffusion equation as follows: one chromosome is associated to each profile. The genetic evolution of the chromosome allows one to find better and better profiles, eventually converging towards the solution of the inverse problem. The main advantage is that GA may be applied to any arbitrary profile, but several disadvantages exist; for example, the complexity of the algorithm, the slow convergence, and consequently the computer time consumed. On the contrary, TWBS uses a simplified theoretical model of heat diffusion in inhomogeneous materials. According to such a model, the photothermal signal depends linearly on the thermal effusivity inhomogeneities, which may be detected because they act as backscattering centers for the heat flux. The physical problem is reduced to the inversion of an algebraic linear system. The advantage is that TWBS allows excellent reconstructions, but only within the limits of validity of the approximate model.

Summary, Conclusion and Scope for future work

REFERENCE

1. M Paulraj, Non destructive evaluation of ion implanted semiconductor thin films using photothermal deflection spectroscopy, Ph.D thesis, Dept. of Physics, CUSAT, Kochi, Kerala, December 2004.
2. Andreas Mandelis,a) Stefano Paoloni,b) and Lena Nicolaidis Review Sc. Instr. 71,(2000)
3. H. G. Walther and V. Aleshin, Jnl. of Appl. Phy.,86 (1999)6512
4. C. Glorieux, R. Li Voti, J. Thoen, M. Bertolotti and C. Sibilia, Jnl. of Appl. Phy. 85 (1999),7059
5. R. Li Voti, C. Sibilia, and M. Bertolotti, Review of Sc. Instr. 74 (2003),372

Appendix A

Temperature Distribution in a photothermal experiment

Consider the geometry shown in Fig. 1. Regions 0 and 2 are optically nonabsorbing media. Region 1 is the absorbing medium and can be either a thin film, gas liquid, or solid. For simplicity, we assume that all three regions extend infinitely in the radial direction. This assumption does not significantly alter the applicability of the treatment, since focused laser beams are typically much smaller than the radial dimension of the sample, and the thermal diffusion length of most samples is less than typical sample dimensions for experimentally useful chopping frequencies.

In the three regions, the temperature rise T satisfies the equations

$$\nabla^2 T_0 - \frac{1}{k_0} \frac{\partial T_0}{\partial t} = 0 \quad \text{region 0,}$$

$$\nabla^2 T_1 - \frac{1}{k_1} \frac{\partial T_1}{\partial t} = \frac{-Q(r,t)}{k_1} \quad \text{region 1,}$$

$$\nabla^2 T_2 - \frac{1}{k_2} \frac{\partial T_2}{\partial t} = 0 \quad \text{region 2,}$$

subject to the following boundary conditions:

$$\begin{aligned} T_0|_{z=0} &= T_1|_{z=0} & T_1|_{z=l} &= T_2|_{z=l} \\ k_0 \frac{\partial T_0}{\partial z}|_{z=0} &= k_1 \frac{\partial T_1}{\partial z}|_{z=0} & k_1 \frac{\partial T_1}{\partial z}|_{z=l} &= k_2 \frac{\partial T_2}{\partial z}|_{z=l} \end{aligned}$$

where k_i is the conductivity, $k_i/(k_i = k_i/\rho_i C_i)$ is the diffusivity, T_i is the temperature rise of the i th medium above the ambient temperature, and l is the thickness of the absorbing medium. $Q(r,t)$ is the heat deposited were unit volume oscillating at the frequency ω in the absorbing medium and is given by

Appendix A

$$Q(r, t) = \frac{1}{2} \frac{4P\alpha}{\pi^2 a^2} \exp(-\alpha z) \exp(-2r^2 a^2) \exp(i\omega t) + c.c$$

for a square wave intensity modulated beam where P is the optically exciting beam (pump beam) power a is the absorption coefficient, and a is the $1/a^2$ radius of the Gaussian beam. We have assumed above that over the interaction region between the pump and probe beams, the probe beam is focused to a smaller spot than that of the pump beam, and that the pump beam waist does not change over the confocal distance of the probe beam.

The diffusion equation is solved by making the following substitutions. For region 0, we have

$$T_0(r, t) = \frac{1}{2} \int_0^\infty \delta d \delta J_0(\delta r) E(\delta) \exp(\beta_0 z) \exp(i\omega t) + c.c.;$$

for region 2, we have

$$T_2(r, t) = \frac{1}{2} \int_0^\infty \delta d \delta J_0(\delta r) D(\delta) \exp(-\beta_2(z-1)) \exp(i\omega t) + c.c.;$$

and for region 1, we have

$$T_1(r, t) = \frac{1}{2} \int_0^\infty \delta d \delta J_0(\delta r) [T(\delta) \exp(-\alpha z) + A(\delta) \exp(-\beta_1 z) + B(\delta) \exp(\beta_1 z)] \exp(i\omega t) + c.c.;$$

where $T_i(r, z)$ is the component of the temperature difference oscillating at frequency ω ,

$$T(\delta) = \frac{P\alpha}{\pi^2 k_1} \frac{\exp[-(\delta a)^2 / 8]}{\beta_1^2 - \alpha^2}$$

$$\beta_1^2 = \delta^2 + i\omega / k_1,$$

substituting into diffusion equation and satisfying the boundary conditions, we find that

Appendix A

$$A(\delta) = -[(1-g)(b-r)\exp(-\alpha l) + (g+r)(1+b) \\ \times \exp(\beta_1 l)]T(\delta) / H(\delta)$$

$$B(\delta) = -[(1+g)(b-r)\exp(-\alpha l) + (g+r)(1-b) \\ \times \exp(-\beta_1 l)]T(\delta) / H(\delta)$$

$$D(\delta) = T(\delta)\exp(-\alpha l) + A(\delta)\exp(-\beta_1 l) + B(\delta)\exp(\beta_1 l)$$

$$E(\delta) = T(\delta) + A(\delta) + B(\delta)$$

$$H(\delta) = -[(1+g)(1+b)\exp(\beta_1 l)] - (1-g)(1-b)\exp(-\beta_1 l)]$$

where

$$g = k_0\beta_0 / k_2\beta_1, \quad b = k_2\beta_2 / k_2\beta_1, \quad r = \alpha l \beta_1$$

The final temperature distribution is obtained by combining the above.

To obtain the 1-D solution, we take $2\pi \int_0^\infty r dr$ of since

$$\int_0^\infty \delta d\delta \int_0^\infty r dr J_0(\delta r) R(\delta) = R(0), \text{ one obtains.}$$

$$\bar{T}_1(z) = 2\pi [T(0)\exp(-\alpha z) + A(0)\exp(-k_1 z) + B(0)\exp(k_1 z)]$$

where

$$k_i^2 = i\omega / k_i \quad \text{and} \quad \bar{T}_1(z) = 2\pi \int_0^\infty r dr T_1(r, z)$$

simplifying this expression, the result is

$$\bar{T}_1(z) = \frac{p\alpha}{H(0)\pi^2 k_1 (k_i^2 = a^2)} \{ (1+g)(1+b)\exp(k_1 l - \alpha z) \\ - (1-g)(1-b)\exp(k_1 l - \alpha z) - (1-g)(b-r) \\ \times \exp(\alpha l - k_1 z) - (g+r)(1+b)\exp[k_1(l-z)] \\ \times (1+g)(b-r)\exp(-\alpha l + k_1 z) - (g+r)(1-b) \\ \times \exp(k_1 l + k_1 z) \}$$

Appendix A

Hence the physical interpretation is that any temperature distribution can be decomposed into distributions of the form $J_0(\delta r) \exp(-\beta_i z)$.

These distributions act independently of each other and have an effective thermal length given by $l_i = 1/\text{Re}(\beta_i) = \{\text{Re}[(k_i^2 + \delta^2)]^{1/2}\}^{-1}$. These case $\delta = 0$ gives a radially uniform temperature distribution, which as expected, is similar to the 1-D case.

For region 1, $A(\delta)$ is the magnitude of the thermal wave diffusing in the positive z direction, $B(\delta)$ is the thermal wave diffusing in the negative z direction, and $T(\delta)$ is the temperature rise due to energy deposited at location (r, z) by the pump beam.

If heat diffusion into the bounding media is neglected and the temperature is integrated along the z direction it reduces to

$$\int_0^l d_z T_1(r, t) = \frac{1}{2} \frac{P[1 - \exp(-\alpha l)]}{\pi^2 k_1} \\ \times \int_0^\infty \frac{\delta J_0(\delta r) \exp[-(\delta a)^2 / 8]}{\delta^2 + K_1^2} d\delta \exp(i\omega t) + c.c.$$

if the thermal length $(\text{Re}K_1)^{-1}$ is much smaller than the beam radius, the denominator becomes K_1^2 , and the integral can be performed. The result is

$$\int_0^l d_z T_1(r, t) \\ = \frac{1}{2} \frac{P[1 - \exp(-\alpha l)] 4}{\delta^2 i\omega(\rho C)_1 a^2} \exp(-2r^2 / a^2) \exp(i\omega t) + c.c.$$

in the above case, the temperature distribution follows the beam profile because there is no diffusion of heat.

Appendix A

If the thermal length is much greater than the beam radius, K_1^2 can be neglected in the denominator. The solution for the temperature gradient reduces to

$$\int_0^t d_z T_1(r, t) = \frac{1}{2} \frac{P[1 - \exp(-at)]}{\pi^2 K_1 r} [1 - \exp(-2r^2/a^2)] \exp(i\omega t) + c.c.$$

This result shows that the temperature distribution extends significantly beyond the beam profile for low chopping frequencies.

B. Optical Beam propagation

The effect of the temperature distribution on the probe beam is now calculated. The index of refraction is, in general, a function of temperature. Hence

$$n(r, t) = n_0 + \Delta n(r, t) = n_0 + \left. \frac{\delta n}{\delta T} \right|_{T_{\text{ambient}}} T(r, t)$$

where $(\delta n / \delta T)$ is typically 10^{-4}C^{-1} for liquids and 10^{-5}C^{-1} solids. The propagation of the Gaussian probe beam through the spatially varying index of refraction is given by

$$\frac{d}{ds} \left(n_0 \frac{dr_0}{ds} \right) = \nabla_{\perp} n(r, t)$$

where r_0 is the perpendicular displacement of the beam from its original direction, n_0 is the uniform index of refraction, and $\nabla_{\perp} n(r, t)$ is the gradient of the index of refraction perpendicular to S (the ray path). The change in the complex beam parameter q is given by

$$\frac{d}{ds} (1/q_{S_{i\perp}}) = - \left(\frac{1}{q_{S_{i\perp}}} \right)^2 - \frac{\delta^2 n}{n_0 \delta S_{i\perp}^2} \quad i = 1, 2$$

Appendix A

where $1/q_{S_{i\perp}} = 1/R_{S_{i\perp}} - i\lambda/(n_0\pi w_0^2)$. $1/R_{S_{i\perp}}$ is the radius of curvature of the phase fronts, w_0 is the $1/e^2$ spot size, and λ is the vacuum wavelength of the probe beam. We also assume that the deflection is small compared with the temperature distribution. Since typical deflections are 10^{-5} rad over 1 cm, the total deviation is $0.1 \mu\text{m}$, which is much smaller than the typical $50\text{-}\mu\text{m}$ spot size of a focused laser. Integrating over the ray path S gives.

$$\frac{dr_0}{ds} = \frac{1}{n_0} \int_{\text{path}} \nabla_{\perp} n(r, t) ds,$$

and

$$\begin{aligned} & \left. 1/q_{S_{i\perp}} \right|_{\text{end of interaction}} - \left. 1/q_{S_{i\perp}} \right|_{\text{beginning of interaction}} \\ &= \int_{\text{path}} ds \left(\frac{-\frac{1}{2} \frac{\delta^2 n}{n_0 \delta S_{i\perp}^2}}{q_{S_{i\perp}}} \right) \quad i = 1, 2 \end{aligned}$$

since the deviation is small

$$\frac{dr_0}{ds} \cong \phi = \frac{1}{n_0} \frac{\delta n}{\delta T} \int_{\text{path}} \nabla_{\perp} T(r, t) ds,$$

where ϕ is the angular deviation from S . This is a 3-D generalization valid for Gaussian beams of the 1-D case. We see that the effect of the curvature of the index of refraction is equivalent to an astigmatic lens of focal length F_i in the S_i direction where F_i is given by

$$\begin{aligned} 1/F_i &= -\frac{1}{n_0} \int_{\text{path}} \frac{\delta^2 n}{n_0 \delta S_{i\perp}^2} ds \\ &= -\frac{1}{n_0} \frac{\delta n}{\delta T} \int_{\text{path}} \frac{\delta^2 T}{\delta S_{i\perp}^2} ds \quad i = 1, 2 \end{aligned}$$

Appendix A

This demonstrates one difference between PDS and TL. PDS probes the gradient of the temperature, while TL probes its curvature.

2. Transverse PDS

For transverse PDS, the probe beam propagates completely within region 0.

The probe beam path is

$$y = y_0 \quad z = (\tan \psi)x + z_0$$

For small $\tan \psi$, $\nabla_{\perp} T = (\delta T)/(\delta z)$

The deflection is given by

$$\phi = \frac{1}{2} \frac{\exp(i\omega t)}{n_0} \frac{\delta n}{\delta T} \int_{-\infty}^{z_0(\tan \psi)} dx$$
$$\times \int_0^{\infty} \delta J_0(\delta \sqrt{y_0^2 + x^2}) \beta_0 E(\delta) \exp\{(\tan \psi)x + z_0\} \beta_0 d\delta + c.c$$

2. Transverse PDS

for the transverse PDS, several parameters were varied

- a. Frequency dependence. It is seen that the signal falls off very rapidly as a function of frequency. Because $T \propto \exp(z_0/l_t)$, the signal falls off exponentially as the frequency increases. The important consequence of the above is that for high modulation frequencies, pulsed work, or solids immersed in liquids, the signal is bigger if the probe beam is carefully aligned close to the sample surface and hence should be focused. This condition shows that the signal is optimized for flat samples with small lateral dimensions.
- b. Signal dependence on pump beam radius a . The signal increases as $1/a^2$ as the pump beam is focused. The temperature rise has an a^2

Appendix A

dependence, while the interaction length goes as $1/a$. when the pump beam radius becomes as small as the lateral thermal length, no further increase in the signal is observed. For z_0 less than the thermal length in air l_a , the lateral thermal length is approximately the thermal length in the glass l_g ; for z_0 greater than l_a , the lateral thermal length is l_a .

- c. Signal dependence on probe and pump beam offset y_0 . By varying the offset y_0 of the beams. The profile of the temperature in region 0 is probed at the position z_0 of the probe beam. The main peak width is determined by the spot size of the pump beam and the sample thermal length. Because l_a is larger than l_g , the heat flows from the air back into the sample for y_0 greater than l_g . This reversed heat flow causes the second, but weaker, maximum with its phase shifted 180° from that of the central peak. For z_0 greater than l_a , the heat flows away from the sample for all y_0 values, and the secondary peak will no longer be observed. Both the 180° phase shift and the disappearance of the secondary peak can be verified experimentally.
- d. Signal dependence on the probe beam tilt angle ψ . For a small pump radius (40 μm), the tilt angle is not important unless the sample actually intercepts the probe beam. In the case of broadband pump beam, the signal is more sensitive to the tilt angle because of the longer path grazing the sample. This often requires a longer focal length lens for the probe beam.
- e. Pump beam offset in the z_0 direction.. In general, the signal increases exponentially as the probe beam approaches the sample. The exponential increase can be used to determine the diffusivity of the

Appendix A

deflecting medium. For the more realistic case of a beam focused on a poor conducting substrate, the results are more complex. For z_0 increasing, the temperature distribution is determined by the thermal properties of the air (or an appropriate fluid) so the beam deflection falls off exponentially as l_a . On the other hand, for z_0 decreasing, the temperature distribution gets smaller and more compressed. Hence the signal rises faster than exponentially.

For cw PDS, the pointing noise of the probe laser predominates. The intensity fluctuations of the probe beam can be discriminated against by adjustment of the probe spot on the detector. Typically, the differential input can reject intensity fluctuations to 1 part in 1000. for a typical laser, the ratio of the intensity noise to the dv level was $5 \times 10^{-6}/\sqrt{\text{Hz}}$, while the observed noise ratio was $6 \times 10^{-7}/\sqrt{\text{Hz}}$. The expected contribution of laser intensity fluctuations in $5 \times 10^{-9}/\sqrt{\text{Hz}}$, which is much less than the observed noise. The noise is due to pointing fluctuations. The electronic noise is easily calculated and seldom limits the sensitivity. The most significant electronic noise term is the shot noise, which sets a detection limit of $3.4 \times 10^{-10} \text{ rad}/\sqrt{\text{Hz}}$ for a 1-m W probe laser.

ADSP-2100 Family DSP Microcomputers

SUMMARY

16-Bit Fixed-Point DSP Microprocessors with On-Chip Memory
Enhanced Harvard Architecture for Three-Bus
Performance: Instruction Bus & Dual Data Buses
Independent Computation Units: ALU, Multiplier/ Accumulator, and Shifter
Single-Cycle Instruction Execution & Multifunction Instructions
On-Chip Program Memory RAM or ROM & Data Memory RAM
Integrated I/O Peripherals: Serial Ports, Timer,

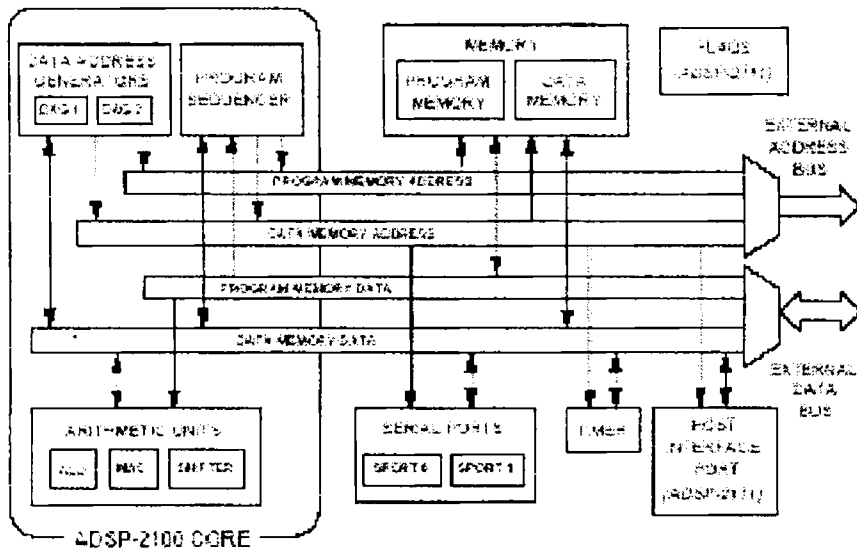
FEATURES

25 MIPS, 40 ns Maximum Instruction Rate
Separate On-Chip Buses for Program and Data Memory
Program Memory Stores Both Instructions and Data
(Three-Bus Performance)
Dual Data Address Generators with Modulo and Bit-Reverse Addressing
Efficient Program Sequencing with Zero-Overhead
Looping: Single-Cycle Loop Setup
Automatic Booting of On-Chip Program Memory from Byte-Wide External
Memory (e.g., EPROM)
Double-Buffered Serial Ports with Companding Hardware, Automatic Data
Buffering, and Multichannel Operation
Three Edge- or Level-Sensitive Interrupts
Low Power IDLE Instruction
PGA, PLCC, PQFP, and TQFP Packages
MIL-STD-883B Versions Available

GENERAL DESCRIPTION

The ADSP-2100 Family processors are single-chip microcomputers optimized for digital signal processing (DSP) and other high speed numeric processing applications. The ADSP-21xx processors are all built upon a common core. Each processor combines the core DSP architecture—computation units, data address generators, and program sequencer—with differentiating features such as on-chip program and data memory RAM, a programmable timer, one or two serial ports,

Appendix-B

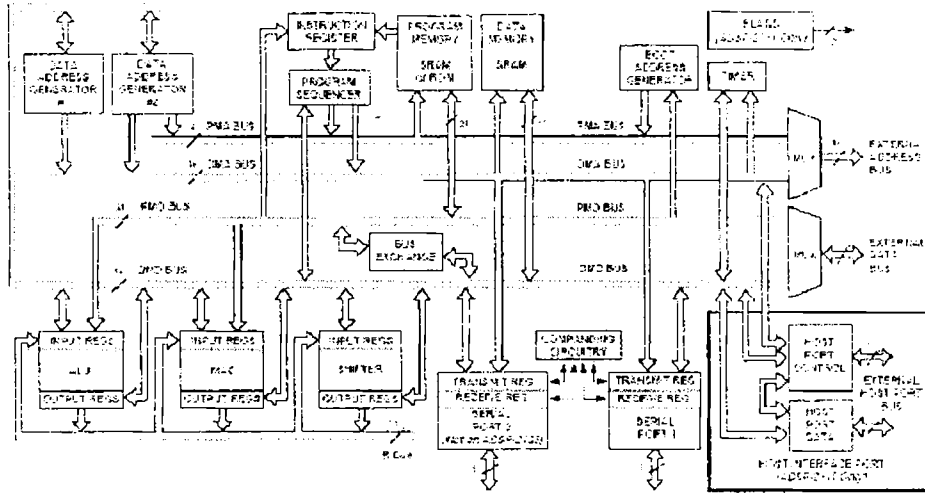


Fabricated in a high speed, submicron, double-layer metal CMOS process, the highest-performance ADSP-21xx processors operate at 25 MHz with a 40 ns instruction cycle time. Every instruction can execute in a single cycle. Fabrication in CMOS results in low power dissipation. The ADSP-2100 Family's flexible architecture and comprehensive instruction set support a high degree of parallelism. In one cycle the ADSP-21xx can perform all of the following operations:

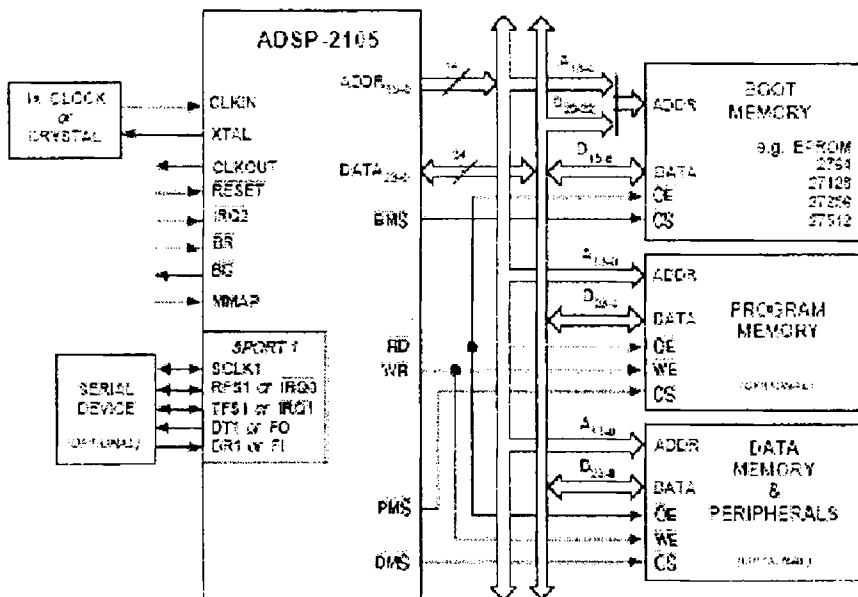
- Generate the next program address
- Fetch the next instruction
- Perform one or two data moves
- Update one or two data address pointers
- Perform a computation
- Receive and transmit data via one or two serial ports

The ADSP-2101, ADSP-2105, and ADSP-2115 comprise the basic set of processors of the family. Each of these three devices contains program and data memory RAM, an interval timer, and one or two serial ports.

Appendix-B



Architecture



Interfacing



Appendix-B

The software PLL

These PLL simulators are based on the methods and 'structograms' presented in Chapter 5 of the text, "Phase-Locked Loops, Theory, Design and Applications", by Roland E. Best, McGraw-Hill, Inc., 1993.

```
#include <float.h>
#include <math.h>
#include <iostream.h>

static float ud[2],uc[2],uf[2],u2[3],phi2[3],Q[2],tm[2],t2[2];
static float a1,b0,b1,w0,K0,Kd,T,phi0,taul,tau2,Ub,u10;

/*
 * This version of a linear PLL simulator operates on signal
 * vectors. Given a signal, 'u1', vector of length, 'len',
 * and appropriate parameter values, it calculates and
 * returns corresponding vectors for the output values of
 * the phase detector 'ud', the filter 'uf', the
 * DCO 'u2' and the phase accumulator 'phi2'.
 */
void lpll(int len,float *u1,float *u2,float *ud,float *uf,
         float *phi2,float a1,float b0,float b1,float T,float w0,
         float K0,float Kd)
{
    int n;

    // Initialize
    ud[0] = 0.0;
    uf[0] = 0.0;
    u2[1] = 0.0;
    phi2[1] = 0.0;
    n = 1;
    // Loop
    while (n < (len-1)) {
        ud[n] = Kd * u1[n] * u2[n];
        uf[n] = -a1*uf[n-1] + b0*ud[n] + b1*ud[n-1];
        phi2[n+1] = phi2[n] + (w0 + K0*uf[n]) * T;

        if (phi2[n+1] > M_PI)
            phi2[n+1] -= 2*M_PI;
        if (phi2[n+1] >= 0.0)
```

Appendix-B

```
        u2[n+1] = 1.0;
    else
        u2[n+1] = -1.0;
// Shift
    n++;
}
}
/*
 * This routine sets up global (static) variables for use
 * by the reentrant version of the linear PLL simulator,
 * 'lpll2'.
 *
 * It can be called at any time to reset the operating
 * conditions of the PLL.
 */
void initlpll2(float detector,float filter,float dco,float
phase,
float alcoeff,float b0coeff,float blcoeff,float omega0,
float gainK0,float gainKd, float sampleT){

    ud[0] = detector;
    uf[0] = filter;
    u2[0] = 0.0;
    u2[1] = dco;
    phi2[0] = 0.0;
    phi2[1] = phase;
    a1 = alcoeff;
    b0 = b0coeff;
    b1 = blcoeff;
    w0 = omega0;
    K0 = gainK0;
    Kd = gainKd;
    T = sampleT;
}

/*
 * This version of the linear PLL simulator processes a single
 * input event. It accepts a value for the signal and returns
 * the updated values for the phase detector, filter, DCO and
 * phase accumulator.
 *
 * The routine is reentrant, as it saves critical values in
 * static variables so they are carried forward from one call
 * to the next.
 */
```

Appendix-B

```
* It is a requirement that the static variables be initialized
* by 'initpll2' prior to the first call to lpll2.
*/
void lpll2(float sig, float *detector, float *filter, float
*dco, float *phase)
{
// Calculate new quantities
    ud[1] = Kd * sig * u2[1];
    uf[1] = -a1*uf[0] + b0*ud[1] + b1*ud[0];
    phi2[2] = phi2[1] + (w0 + K0*uf[1]) * T;

// Collapse phase and determine dco
    if (phi2[2] > M_PI)
        phi2[2] -= 2.0*M_PI;
    if (phi2[2] >= 0.0)
        u2[2] = 1.0;
    else
        u2[2] = -1.0;

// Shift
    ud[0] = ud[1];
    uf[0] = uf[1];
    phi2[1] = phi2[2];
    u2[1] = u2[2];

// Set return values
    *detector = ud[0];
    *filter = uf[0];
    *dco = u2[1];
    *phase = phi2[1];
}
```

DIGITAL PLL

```
/*
* This version of a digital PLL simulator operates on vectors.
The
* primary difference between this PLL and the linear PLL is
* the replacement of a multiplier type phase detector in the
linear
* PLL with a digital phase/frequency detector.
*
* In the linear PLL, the input signal is assumed to be sampled
at
* regular (T) intervals. For the digital PLL, a signal vector,
'ul',
```


Appendix-B

```

    * and a time vector, 't1', must be provided. This simulates
operation
    * in an interrupt driven system where the time vector takes
the
    * place of a 'time stamp' captured at the start of an
interrupt
    * triggered by edges of the input signal.
    *
    */
void dpll(int len,float *u1,float *t1,float *t2,float *Q,float
*uc,
    float *uf,float *phi2,float taul,float tau2,float w0,float
K0,float Ub)
{
    int n,idx;
    float Tn,tcross,tp,tm,oldphi,newphi;
    float tmp1,tmp2;

// Initialize
    uc[0] = 0.0;
    uf[0] = 0.0;
    Q[0] = 0.0;
    phi2[0] = 0.0;
    t2[0] = 0.0;
    oldphi = newphi = 0.0;

    n = 1;
    idx = 1;
    while (n < len) {
        Tn = t1[n] - t1[n-1];

// Calculate and correct phi2
        phi2[n] = phi2[n-1] + (w0 + K0 * uf[n-1]) * Tn;
        if (phi2[n] > 2.0 * M_PI) {
            phi2[n] -= 2.0 * M_PI;
            phi2[n-1] -= 2.0 * M_PI;
        }
// Old code for updating t2...
        newphi = oldphi + (w0 + K0 * uf[n-1]) * Tn;
        if (newphi > M_PI) {
            t2[idx++] = t1[n-1] + (M_PI - oldphi)/(newphi-
oldphi)*Tn;
            newphi -= M_PI;
        }

        oldphi = newphi;
    }
}
```

Appendix-B

```
// Calculate tcross
    if ((phi2[n] >= 0.0) && (phi2[n-1] < 0.0))
        tcross = -phi2[n-1]*Tn/(phi2[n]-phi2[n-1]);
    else
        tcross = 0.0;

// Calculate tp, tm, Q[n]
    if (Q[n-1] == +1.0) {
        if (tcross == 0.0) {
            tp = Tn;
            tm = 0.0;
            Q[n] = 1.0;
        }
        else {
            tp = tcross;
            tm = 0.0;
            Q[n] = 0.0;
        }
    }
    else if (Q[n-1] == 0.0) {
        if (ul[n-1] == 1.0) {
            if (tcross == 0.0) {
                tp = Tn;
                tm = 0.0;
                Q[n] = 1.0;
            }
            else {
                tp = tcross;
                tm = 0.0;
                Q[n] = 0.0;
            }
        }
        else {
            if (tcross == 0.0) {
                tp = 0.0;
                tm = 0.0;
                Q[n] = 0.0;
            }
            else {
                tp = 0.0;
                tm = Tn - tcross;
                Q[n] = -1.0;
            }
        }
    }
}
```

Appendix-B

```
else { // (Q[n-1] == -1)
    if (u1[n-1] == 1.0) {
        if (tcross == 0.0) {
            tp = 0.0;
            tm = 0.0;
            Q[n] = 0.0;
        }
        else {
            tp = 0.0;
            tm = Tn - tcross;
            Q[n] = -1.0;
        }
    }
    else {
        tp = 0.0;
        tm = Tn;
        Q[n] = -1.0;
    }
}
// Update filter
if (tp > 0.0) {
    uc[n] = uc[n-1] + (Ub-uc[n-1])*tp/(taul+tau2);
    uf[n] = uc[n] + (tp/Tn)*(tau2/(taul+tau2))*(Ub-
uc[n]);
}
else {
    if (tm > 0.0) {
        uc[n] = uc[n-1] * (1.0 - tm/(taul+tau2));
        uf[n] = uc[n] * (1.0 -
(tau2/(taul+tau2))*(tm/Tn));
    }
    else {
        uc[n] = uc[n-1];
        uf[n] = uc[n];
    }
}
n++;
}
}
void initdpll2(float cap,float filter,float Qstate,float phase,
float phi,float gainK0,float gainKd,float omega0,float t0,
float sig0,float tK1,float tK2,float Vc)
{
    uc[0] = cap;
    uf[0] = filter;
    Q[0] = Qstate;
```

Appendix-B

```
T = t0;
phi2[0] = phase;
K0 = gainK0;
Kd = gainKd;
w0 = omega0;
phi0 = phi;
u10 = sig0;
taul = tK1;
tau2 = tK2;
Ub = Vc;
}

void dpll2(float sig, float timing, float *t2, float *filter,
          float *phase)
{
    int idx;
    float Tn, tcross, tp, tm, newphi;

    Tn = timing - T;

    // Calculate and correct phi2
    phi2[1] = phi2[0] + (w0 + K0 * uf[0]) * Tn;
    if (phi2[1] > 2.0 * M_PI) {
        phi2[1] -= 2.0 * M_PI;
        phi2[0] -= 2.0 * M_PI;
    }
    newphi = phi0 + (w0 + K0 * uf[0]) * Tn;
    if (newphi > M_PI) {
        *t2 = T + (M_PI - phi0) / (newphi - phi0) * Tn;
        newphi -= M_PI;
        idx++;
    }
    phi0 = newphi;

    // Calculate tcross
    if ((phi2[1] >= 0.0) && (phi2[0] < 0.0))
        tcross = -phi2[0] * Tn / (phi2[1] - phi2[0]);
    else
        tcross = 0.0;

    // Calculate tp, tm, Q[1]
    if (Q[0] == +1.0) {
        if (tcross == 0.0) {
            tp = Tn;
            tm = 0.0;
        }
    }
}
```

Appendix-B

```
        Q[1] = 1.0;
    }
    else {
        tp = tcross;
        tm = 0.0;
        Q[1] = 0.0;
    }
}
else if (Q[0] == 0.0) {
    if (u10 == 1.0) {
        if (tcross == 0.0) {
            tp = Tn;
            tm = 0.0;
            Q[1] = 1.0;
        }
        else {
            tp = tcross;
            tm = 0.0;
            Q[1] = 0.0;
        }
    }
    else {
        if (tcross == 0.0) {
            tp = 0.0;
            tm = 0.0;
            Q[1] = 0.0;
        }
        else {
            tp = 0.0;
            tm = Tn - tcross;
            Q[1] = -1.0;
        }
    }
}
else { // (Q[0] == -1)
    if (u10 == 1.0) {
        if (tcross == 0.0) {
            tp = 0.0;
            tm = 0.0;
            Q[1] = 0.0;
        }
        else {
            tp = 0.0;
            tm = Tn - tcross;
            Q[1] = -1.0;
        }
    }
}
```

Appendix-B

C9076

```
    }
    else {
        tp = 0.0;
        tm = Tn;
        Q[1] = -1.0;
    }
}
// Update filter
if (tp > 0.0) {
    uc[1] = uc[0] + (Ub - uc[0]) * tp / (tau1+tau2);
    uf[1] = uc[1] + (tp/Tn) * (tau2/(tau1+tau2)) * (Ub-
uc[1]);
}
else {
    if (tm > 0.0) {
        uc[1] = uc[0] * (1.0 - tm/(tau1+tau2));
        uf[1] = uc[1] * (1.0 - (tau2/(tau1+tau2))*(tm/Tn));
    }
    else {
        uc[1] = uc[0];
        uf[1] = uc[1];
    }
}
// Shift variables
}
```